

Selective oxidation of methane to hydrocarbon oxygenates using H₂O₂ over Fe-containing MFI zeolites in a micro fixed-bed reactor

Von der Fakultät Energie-, Verfahrens- und
Biotechnik der Universität Stuttgart
zur Erlangung der Würde eines
Doktor-Ingenieurs (Dr.-Ing.)
genehmigte Abhandlung

Vorgelegt von

Hualiang Zuo

aus Hunan, China

Vorsitzender: Prof. Dr. rer. nat. Andreas Friedrich
Hauptberichter: Prof. Dr.-Ing. Elias Klemm
Mitberichter: Prof. Dr.-Ing. Ulrich Nieken

Tag der mündlichen Prüfung: 14.09.2018

Institut für Technische Chemie der Universität Stuttgart

2018

Erklaerung ueber die Eigenstaendigkeit der Dissertation

Ich versichere, dass ich die vorliegende Arbeit mit dem Titel "Selective oxidation of methane to hydrocarbon oxygenates using H₂O₂ over Fe-containing MFI zeolites in a micro fixed-bed reactor" selbstaendig verfasst und keine anderen als die angegebenen Quellen und Hilfsmittel benutzt habe; aus fremden Quellen entnommene Passagen und Gedanken sind als solche kenntlich gemacht. Diese Dissertation wurde zu keiner Zeit in derselben oder substantiell aehnlichen Version bei einem anderen Pruefungsamt eingereicht.

Declaration of Authorship

I hereby certify that the dissertation entitled "Selective oxidation of methane to hydrocarbon oxygenates using H₂O₂ over Fe-containing MFI zeolites in a micro fixed-bed reactor" is entirely my own work except where otherwise indicated. Passages and ideas from other sources have been clearly indicated. This thesis has never been submitted in the same or substantially similar version to any other examination office.

Name/Name: Hualiang Zuo

Unterschrift/Signed:

Datum/Date:

Acknowledgments

Die Zeit vergeht so schnell! Four-years of research journey will soon end. This work cannot be carried out smoothly without many people's help. I would like to thank many of them who contributed to the thesis from different aspects.

First and foremost, I would like to thank Prof. Dr.-Ing. Elias Klemm for providing me with the opportunity for working in ITC. He always supported me to try my ideas and offered valuable suggestions or encouragement when needed. I learned a lot from his high level of specialty and rigorous academic standard. I also want to thank him for the ways of thinking for solving problems I learned from him during our communications, which may be more important than the problem itself! I really appreciate his guidance and support.

I would like to thank Prof. Dr.-Ing. Ulrich Nieken for being the co-referee of my thesis. I really thank his great effort for the proofreading. I also thank Prof. Dr. rer. nat. Andreas Friedrich for being the chairman of my PhD defense.

The financial support from China Scholarship Council (CSC) is highly acknowledged!

Thanks to our collaborators of this work, Prof. Dr. Vera Meynen, Qi Xin and Karen Leysens from the University of Antwerp, Laboratory of Adsorption and Catalysis. They enriched the content and methods of this work a lot.

Thanks to other colleagues in ITC for creating a nice working atmosphere. I acknowledge the support I received from Elisa Favaro (secretary and organization), Ines Lauerwald (technical support), Heike Fingerle (ICP), Barbara Gerling (XRD and TGA), Ingo Nägele (IT), Matthias Scheibe (reagents ordering) and Andreas Stieber (workshop). Special thanks go to Felix Neher and Dr. Philipp Eversfield for the support of my setup at the beginning of my work. Thanks to Swen Lang & Daniel Mack & Moritz Messner (SEM), Fabian Guba & Paul Rößner (TEM), Armin Löwe & Pascal Hermann (PhD meeting organization) and Robin Himmelmann (TPD/TPR technical support). I also thank Dr. Moritz Heuchel, Dorothea Häussermann and Joachim Hildebrand for N₂ sorption measurements for some of my samples. I really appreciate the fruitful discussion with Thomas Lange and Dennis Kopljar and also the help from Thomas Lange for the preparation of “Zusammenfassung”. In particular, I would like to thank the football group in ITC and Benjamin

Wriedt & Fabian Guba for organizing football games. I really enjoy the games we played together and cherish the friendship with you guys!

Thanks also go to other people who I did not mention but contributed to the thesis.

Finally yet importantly, I want to thank my family. I thank my parents for their everlasting selfless love and support to me! I also thank my elder brother and sister-in-law for taking care of our parents when I am far away from them. The most special thanks go to my beloved wife, Li Zuo. It is not easy to live and integrate into a different culture far away from home. We made it happen and got a so lovely child. I want to tell her: I sincerely appreciate your trust, understanding and encouragement to me and the selfless devotion to our family. Let us enjoy together the coming exciting adventures in the rest of our life.

Contents

Acknowledgments	I
Contents	III
Nomenclature	VII
Abstract	XI
Zusammenfassung	XV
1 Introduction	1
1.1 Background and motivations.....	1
1.2 Selective oxidation of methane using different oxidant.....	4
1.2.1 Selective oxidation of methane with SO ₃	4
1.2.2 Selective oxidation of methane with N ₂ O	7
1.2.3 Selective oxidation of methane with O ₂	8
1.2.4 Selective oxidation of methane with H ₂ O ₂	11
1.3 Selective oxidation of methane over Cu- and Fe-containing zeolites.....	14
1.3.1 Inspiration from methanotrophic bacteria	15
1.3.2 Selective oxidation of methane over Cu-containing zeolites	18
1.3.3 Selective oxidation of methane over Fe-containing zeolites	23
1.4 Preparation of Fe-containing MFI zeolites.....	28
1.4.1 Direct hydrothermal synthesis	29
1.4.2 Post-synthetic methods	31
1.5 Aim of this work	33
2 Experimental methods	35
2.1 Experimental setup.....	36
2.2 Preparation of the catalysts	37
2.2.1 Silicalite-1, Fe-silicalite-1 and Cu-silicalite-1/Fe-silicalite-1	37
2.2.2 Fe-silicalite-1 with large crystals.....	39
2.2.3 Fe-silicalite-1 with small crystals.....	39
2.2.4 H-ZSM-5	39
2.2.5 Solid State Ion Exchange.....	40
2.2.6 Liquid Ion Exchange	40
2.2.7 Molecular Designed Dispersion method	40
2.2.8 Wetness Impregnation	41

2.2.9 Na-form of Fe-silicalite-1 <i>via</i> hydrothermal synthesis.....	41
2.2.10 Overview of the prepared samples	41
2.3 Characterization of the catalysts	43
2.3.1 Powder X-Ray Diffraction.....	43
2.3.2 Chemical Analysis	43
2.3.3 Scanning Electron Microscopy.....	43
2.3.4 Transmission Electron Microscopy	43
2.3.5 FT-Infrared Spectroscopy.....	44
2.3.6 Low Temperature Nitrogen Physisorption	44
2.3.7 H ₂ -Temperature Programmed Reduction	44
2.3.8 NH ₃ -Temperature Programmed Desorption	44
2.3.9 Diffuse reflectance Ultraviolet-Visible spectroscopy.....	44
2.3.10 Thermogravimetric analysis	45
2.4 Procedure of the catalytic experiments	45
2.5 Analysis of products.....	46
3 Optimizing catalyst performance.....	49
3.1 Introduction	49
3.2 Catalysts and characterization.....	49
3.3 Adjusting appropriate reaction conditions	51
3.3.1 Variation of the reaction temperature.....	52
3.3.2 Decreasing the over-oxidation level	54
3.3.3 Comparison with the state-of-the-art.....	56
3.3.4 Reaction scheme	58
3.4 Summary	60
4 Selective oxidation of methane over Fe-silicalite-1 catalysts	61
4.1 The influence of different calcination temperatures	61
4.1.1 Introduction	61
4.1.2 Catalysts.....	62
4.1.3 Characterization results	63
4.1.4 Catalytic results and discussion.....	71
4.1.5 Summary.....	73
4.2 The influence of different Fe contents	74
4.2.1 Introduction	74
4.2.2 Catalysts.....	74

4.2.3	Characterization results	75
4.2.4	Catalytic results and discussion.....	84
4.2.5	Summary.....	86
4.3	The influence of different crystal sizes	86
4.3.1	Introduction	86
4.3.2	Catalysts.....	88
4.3.3	Characterization results	88
4.3.4	Catalytic results and discussion.....	92
4.3.5	Summary.....	94
4.4	The influence of different acidities	95
4.4.1	Introduction	95
4.4.2	Catalysts.....	95
4.4.3	Characterization results	96
4.4.4	Catalytic results and discussion.....	99
4.4.5	Summary.....	102
5	Selective oxidation of methane over post-synthetically Fe-loaded MFI zeolites.....	103
5.1	Introduction	103
5.2	Catalysts and characterization results	103
5.2.1	Catalysts.....	103
5.2.2	Characterization results	104
5.3	Catalytic results and discussion	113
5.4	Summary	117
6	Conclusion	119
7	References.....	121
	List of figures.....	129
	List of tables.....	133

Nomenclature

Symbols

Symbols	Unit	Designation
a_i	-	carbon atom number of product i
c_{o,H_2O_2}	mol/L	initial molar concentration of H_2O_2 in the liquid flow at the inlet of reactor
$c_{H_2O_2}$	mol/L	concentration of H_2O_2 in the liquid flow behind the reactor
ΔH_{298K}^0	kJ mol ⁻¹	standard enthalpy of formation at the temperature of 298 K
n_i	mol	molar amount of product i in the sample volume behind the reactor
n_{o,CH_4}	mol	molar amount of methane in the sample volume at the inlet of reactor
n_{CH_4}	mol	molar amount methane in the sample volume behind the reactor
S_{BET}	m ² g ⁻¹	specific surface area
S_{ex}	m ² g ⁻¹	external surface area
S_i	mol %	selectivity of product i
μ_i	-	stoichiometric coefficient of product i in corresponding reaction equations
ν_{CH_4}	-	stoichiometric coefficient of methane in corresponding reaction equations
$\nu_{H_2O_2}$	-	stoichiometric coefficient of product H_2O_2 in corresponding reaction equations
V_p	cm ³ g ⁻¹	micropore volume
X	%	conversion

Indices

bpym	bipyrimidine
U.S.	United States

Abbreviations

a.u.	arbitrary units
AIP	aluminum isopropoxide
BET	Brunauer-Emmett-Teller
CTF	covalent triazine-based framework
DFT	density functional theory
DME	dimethyl ether
EPR	electron paramagnetic resonance
EXAFS	Extended X-Ray absorption fine structure
FA	formic acid
FD	formaldehyde
FT-IR	Fourier transform infrared spectroscopy
HPLC	high-performance liquid chromatography
ICP-OES	inductively coupled plasma optical emission spectrometry
IR	infrared spectroscopy
LIE	liquid ion exchanged
MDD	molecular designed dispersion
MFC	mass flow controller
MHP	methyl hydroperoxide
MMO	methane monooxygenase
MMOH	methane monooxygenase hydroxylase
MMOs	methane monooxygenase enzymes
pMMO	particulate methane monooxygenase
pmoB	particulate methane monooxygenase alpha (pmoB) subunit
PXRD	Powder X-ray diffraction
Ref.	reference
SEM	scanning electron microscopy
sMMO	soluble methane monooxygenase
SSIE	solid state ion exchange
TCD	thermal conductivity detector
Tcf	trillion cubic feet

TEM	transmission electron microscopy
TEOS	tetraethyl orthosilicate
TGA	Thermogravimetric analysis
TOF	turnover frequency
TONs	turnover numbers
TPAOH	tetrapropylammonium hydroxide
TPD	temperature programmed desorption
TPR	temperature programmed reduction
UV-Vis-DR	diffuse reflectance ultraviolet-visible spectroscopy
XANES	X-ray absorption near edge structure

Abstract

The selective oxidation of methane to value-added hydrocarbon oxygenates has profound meaning not only for chemical industry but also for academic research. However, it is a key challenge in catalysis as methane is a highly symmetric molecule that does not possess any dipolar moment or functionality that would allow for directing chemical reactions. The presented work studied the selective oxidation of methane to hydrocarbon oxygenates using aqueous H_2O_2 as an oxidant over Fe-containing MFI zeolites. The aim of this work is to improve the catalytic performance by intensifying the mass transport, adapting reaction conditions and optimizing the preparation of Fe-containing MFI zeolites.

Sub-micrometer sized Cu-silicalite-1/Fe-silicalite-1 was prepared and a micro fixed-bed reactor was used to intensify internal and external mass transport of the overall reaction. The reaction conditions were adapted by varying the reaction temperature and the concentration and the flow rate of aqueous H_2O_2 solution. Formic acid was found to be the main hydrocarbon oxygenates product and the positive role of Cu species for obtaining methanol was not observed under given conditions. The TOFs of the reaction could be promoted nearly three orders of magnitude compared to referenced work in a fixed-bed reactor. The adapted reaction temperature was $100\text{ }^\circ\text{C}$. A relative low concentration of H_2O_2 in the aqueous solution (0.12 M) and a relative high liquid flow rate of 1.5 ml/min was preferable for the selective oxidation of methane as it decreases the over-oxidation of methane under given conditions. With such adapted reaction conditions, a selectivity to formic acid of 96.7 % at a methane conversion of 10.3 % could be obtained. The investigation of the reaction scheme revealed that the selective oxidation of methane comprises consecutive oxidation reaction steps over the catalyst and the decomposition of formic acid does not take place

Based on the obtained conclusion of the first part of this work, the preparation of Fe-containing MFI zeolites was optimized in the second part of this work. The influence of different preparation conditions of Fe-silicalite-1 and different post-synthetic methods for Fe loading based on MFI zeolites were investigated.

A series of sub-micrometer and micrometer sized crystals of Fe-silicalite-1 with typical MFI structure were successfully synthesized. The influence of different calcination temperatures, different Fe contents, different crystal sizes and different acidities of Fe-silicalite-1 to the selective

oxidation of methane were studied. After calcination, migration of Fe species from framework to extra-framework positions was observed. Increasing calcination temperatures lead to an increasing fraction of extra-framework iron species with an increasing variety of types and structures. Catalysts calcined at lower temperatures lead to higher levels of selectivity to hydrocarbon oxygenates with lower level of over-oxidation, but relative low values of the TOF and volumetric productivity were obtained. On the other hand, higher calcination temperature lead to higher levels of TOFs and volumetric productivities but a much lower level for the utilization of H₂O₂ and a higher degree of over-oxidation were observed. The catalyst calcined at 550 °C showed the best catalytic performance under given conditions. With increasing Fe contents, the crystal sizes decreased and the morphology of the crystals also changed, indicating that Fe plays an important role as nucleus of crystal growth in the synthesis step. With increasing Fe contents, the amount of both framework and extra-framework iron species and the acidity also increased. Higher Fe contents lead to larger extra-framework iron aggregates, which may be inactive for the selective oxidation of methane but active for H₂O₂ decomposition and over-oxidation to CO₂. A relative low Fe content (e.g., around 0.5 wt. %) is preferable for the catalytic reaction under given conditions. Three kinds of Fe-silicalite-1 catalysts with similar Fe contents and textural properties but different crystal sizes around 140 nm, 400 nm and 5.5 μm were successfully synthesized. Too large or too small crystal sizes of Fe-silicalite-1 lead to lower conversions, TOFs and volumetric productivities. A crystal size of about 400 nm seems to be preferable for the reaction. Four Fe-silicalite-1 catalysts with very different acidities were successfully synthesized. The positively charged iron species play an important role for the selective oxidation of methane. Brønsted acid sites do not play a role as a critical promoter for the activation of methane, but seems to enhance the decomposition of H₂O₂ and over-oxidation reactions.

Sub-micrometer sized crystals of H-ZSM-5 and silicalite-1 with Fe impurities below 10 ppm were successfully synthesized. Different post-synthetic methods and different Fe precursors were used for obtaining Fe loading of MFI zeolites of 0.40 wt. %. Commercial H-ZSM-5, with trace amounts of Fe impurities of 175 ppm, already showed significant methane activation activity while on self-synthesized H-ZSM-5 not any activity was observed, indicating that Brønsted acid sites alone can't activate methane under given conditions. Thus, it is important to have Fe-free H-ZSM-5 samples as the basis for the investigation of methane oxidation with iron-loaded H-ZSM-5 catalysts. Fe loaded on silicalite-1 having the same MFI structure as H-ZSM-5 exhibited no activity in methane

conversion, even bearing the same Fe content, indicating Brønsted acid sites play an important role in obtaining active Fe species when using post-synthetic methods of loading Fe. Different H/Fe-ZSM-5 catalysts based on different post-synthetic methods showed similar methane activation activities and catalysts based on Fe(II) as the precursor for loading Fe showed a better performance with regard to retarding the level of over-oxidation.

Zusammenfassung

Die Selektivoxidation von Methan zu wertvollen, sauerstoffhaltigen Kohlenwasserstoffverbindungen ist nicht nur für die chemische Industrie von tiefgreifender Bedeutung, sondern auch für die akademische Forschung. Dies ist allerdings eine der großen Herausforderungen der Katalyse, da Methan ein hochsymmetrisches Molekül darstellt und über kein Dipolmoment oder funktionelle Gruppen verfügt, die eine Aktivierung und Steuerung chemischer Reaktionen erlauben. Die vorliegende Arbeit ist eine experimentelle Studie zur Selektivoxidation von Methan zu sauerstoffhaltigen Kohlenwasserstoffverbindungen unter Verwendung wässriger H_2O_2 -Lösungen an Fe-haltigen MFI Zeolithen. Ziel dieser Arbeit ist es, durch Intensivierung des Stofftransports, Optimierung der Reaktionsbedingungen und Optimierung der Präparationsmethoden für Fe-haltige MFI Zeolithe, das katalytische Verhalten zu verbessern.

Dazu wurde zuerst ein Cu-Silikalit-1/Fe-Silikalit-1, mit Partikelgrößen im Sub-mikrometer-Bereich, hergestellt und in einem Mikrofestbett verwendet, um den internen und externen Stofftransport für die Gesamtreaktion zu intensivieren. Durch Variationen der Reaktionstemperatur, der Konzentrationen und der Flussraten der wässrigen H_2O_2 -Lösung, wurden die Reaktionsbedingungen optimiert. Dabei konnte Ameisensäure als Hauptprodukt der sauerstoffhaltigen Kohlenwasserstoffe identifiziert werden, wobei der positive Einfluss von Cu auf die Bildung von Methanol bei den verwendeten Versuchsbedingungen nicht beobachtet werden konnte. Allerdings konnten im Vergleich zur Referenzarbeit an einem Festbett die TOFs der Reaktion um nahezu drei Größenordnungen angehoben werden. Es konnte festgestellt werden, dass das Optimum der Reaktortemperatur bei 100°C lag und relativ niedrige Konzentrationen wässriger H_2O_2 -Lösung (0,12 M) bei hohen Flussraten (1,5 ml/min) für die Selektivoxidation von Methan günstig sind, da dies unter den verwendeten Versuchsbedingungen die Überoxidation von Methan unterdrückt. Mittels dieser optimierten Reaktionsbedingungen konnte eine Selektivität zu Ameisensäure von 96,7% bei einem Umsatz von 10,3% erreicht werden. Die so optimierten Versuchsbedingungen wurden im Rahmen dieser Arbeit für die weiteren Untersuchungen im Mikrofestbettreaktor verwendet.

Des Weiteren wurden im Rahmen dieser Arbeit die Präparationsmethoden der Fe-haltigen MFI Zeolithe optimiert. Dazu wurde der Einfluss verschiedener Präparationsbedingungen von Fe-

Silikalit-1 und verschiedene post-synthetische Methoden zur Beladung mit Fe basierend auf MFI-Zeolithen untersucht.

Im Rahmen dieser Arbeit konnte eine Reihe von Mikrometer und sub-Mikrometer großen Kristalliten von Fe-Silikalit-1 mit typischer MFI-Struktur erfolgreich synthetisiert werden. Des Weiteren wurde der Einfluss der Kalzinierungstemperatur, des Eisengehalts, der Kristallgröße und der Azidität von Fe-Silikalit-1 auf die Selektivoxidation von Methan untersucht. Dabei konnte festgestellt werden, dass Fe-Spezies durch die Kalzinierung aus dem Gerüst des Zeolithen auf Extra-Gitterplätze wandern und diese Extra-Gerüst-Fe-Spezies eine heterogene Verteilung aufwiesen. Katalysatoren, die bei relativ niedrigen Temperaturen kalziniert wurden, zeigten dabei niedrige Werte für die TOFs und niedrige volumenbezogene Produktivitäten, während höhere Kalzinierungstemperaturen zu Katalysatoren führten, die eine deutlich niedrigere selektive Nutzung von H_2O_2 aufwiesen und stärker zur Überoxidation von Methan neigten. Der Katalysator, der bei 550°C kalziniert wurde, zeigte dabei die beste katalytische Leistung.

Des Weiteren konnte festgestellt werden, dass mit steigendem Fe-Gehalt die Kristallgröße abnimmt und sich die Morphologie der Kristalle ändert, wodurch nahe liegt, dass Fe eine bedeutende Rolle als Kristallisation beim Kristallwachstum zukommt. Mit steigendem Fe-Gehalt stieg sowohl der Anteil von Gerüst- und Extra-Gerüst-Fe-Spezies als auch die Azidität. Ein hoher Fe-Gehalt führte zu großen Extra-Gerüst-Eisenoxid-Agglomeraten, welche nicht in der Methan-Oxidation aktiv waren, sondern nur in der Zersetzung von H_2O_2 . Unter den gegebenen Reaktionsbedingungen hat sich ein niedriger Fe-Gehalt (z.B. rund 0,5 Ma%) als besonders vorteilhaft für die katalytische Reaktion erwiesen. Für die Aktivierung von Methan ist dabei eine spezielle Struktur der Fe-Spezies als aktives Zentrum nötig, wobei diese nicht einfach durch Erhöhung des Fe-Gehalts erhalten werden können.

Im Rahmen der Arbeit konnten drei verschiedene Fe-Silikalit-1-Zeolithe mit unterschiedlichen Kristallgrößen von ca. 140 nm, 400 nm und $5,5\ \mu\text{m}$ erfolgreich synthetisiert werden. Diese Katalysatoren wiesen ähnliche Fe-Gehalte und strukturelle Eigenschaften auf. Es konnte festgestellt werden, dass zu große oder zu kleine Kristallgrößen von Fe-Silikalit-1 zu niedriger katalytischer Leistung führen, wohingegen sich ein passender Bereich an sub-Mikrometer großen Kristallen als vorteilhaft erwiesen hat. Des Weiteren konnten vier verschiedene Fe-Silikalit-1 Katalysatoren erfolgreich synthetisiert werden, die sich zwar in der Azidität unterschieden, aber

sehr ähnliche Fe-Gehalt, strukturelle Eigenschaften und Partikelgrößen aufwiesen. Die Ergebnisse der Katalyse zeigten, dass der Brønsted-Azidität keine bedeutende Rolle für die Aktivierung von Methan unter den verwendeten Bedingungen zukommt.

Im Rahmen der Arbeit konnten sub-mikrometer große Kristalle von H-ZSM-5 und Silikalit-1 mit Fe-Verunreinigungen von weniger als 10 ppm erfolgreich synthetisiert werden. Für die Beladung der MFI Zeolithe mit 0,4 Ma% Fe wurden verschiedene post-synthetische Methoden und Fe-Vorläufer verwendet, um Fe-MFI zu erhalten. Kommerziell erhältlicher H-ZSM-5 mit Spurenanteilen von Fe (ca. 175 ppm) zeigte bereits eine katalytische Aktivität bei der Methan-Aktivierung, was die Verwendung von Fe freien H-ZSM-5 Proben als Basis für die Untersuchung deutlich macht. Bei dem selbst hergestellten Fe-freien H-ZSM-5 konnte keine Aktivität festgestellt werden, was vermuten lässt, dass Brønsted-Säure-Zentren allein, unter den verwendeten Bedingungen Methan nicht aktivieren können. Daher war es auch wichtig Fe-freie H-ZSM-5 Proben als Basis für die Untersuchung der Methan-Oxidation mit Fe-beladenen H-ZSM-5 zu verwenden. Mit Fe beladener nicht-saurer Silikalit-1 mit ähnlichem Fe-Gehalt war in keinem Fall ein aktiver Katalysator, was verdeutlicht, dass Brønsted-Säure-Zentren eine bedeutende Rolle zukommt, um durch post-synthetische Beladung mit Fe aktive Fe-Zentren zu erhalten. Durch verschiedene post-synthetische Methoden hergestellte H/Fe-ZSM-5-Katalysatoren zeigten ein ähnliches Verhalten in der Methan-Aktivierung, wobei ein auf einem Fe(II)-Vorläufer basierender Katalysator eine bessere Leistung durch Hemmung der Überoxidation aufweist.

1 Introduction

1.1 Background and motivations

The demand for resources and energy is rapidly increasing along with the fast development of economy and the growth of world's population. As well-known fossil resources, such as conventional petroleum, coal and gas are subject to irreversible depletion. However, natural gas is attracting more and more attention as an important resource of clean fossil energy and as a feedstock for chemicals [1]. Especially, relative large unconventional reserves of shale gas, coalbed methane and methane hydrate have been recently discovered [1, 2]. It is worth mentioning that, with the progress of drilling technology and the improvement of mining technology, the global shale gas production capacity has seen explosive growth in the past decade. The U.S. Energy Information Administration projects that the annual natural gas production from shale gas and tight oil would increase from 13.6 trillion cubic feet (Tcf) in 2015 to 29.0 Tcf in 2040 [3] (schematically show in Figure 1.1), which is described as “shale gas revolution” and will inevitably change the energy landscape.

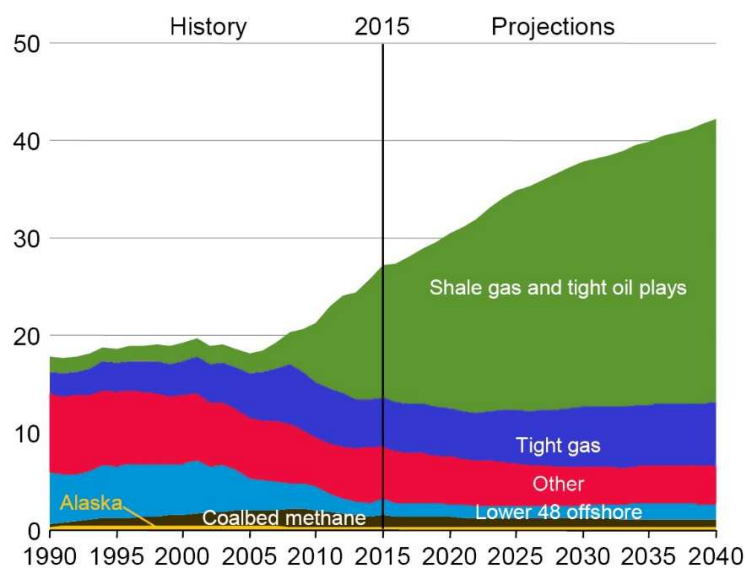


Figure 1.1. U.S. dry natural gas production by source for 1990-2040 (trillion cubic feet) [3].

In a transitional period until renewable sources can play a dominating role, the efficient utilization of substantial natural gas is considered by many experts to be an effective way to compensate for lack of resources and ease the energy crisis for the 21st century [4]. The consumption of natural gas has risen significantly in the recent past [5]. According to the *International Energy Outlook*

2016, the consumption of natural gas worldwide was projected to increase from 120 Tcf in 2012 to 203 Tcf in 2040 (illustrate in Figure 1.2), which accounts for the largest increase in world primary energy consumption among all energy sources [6].

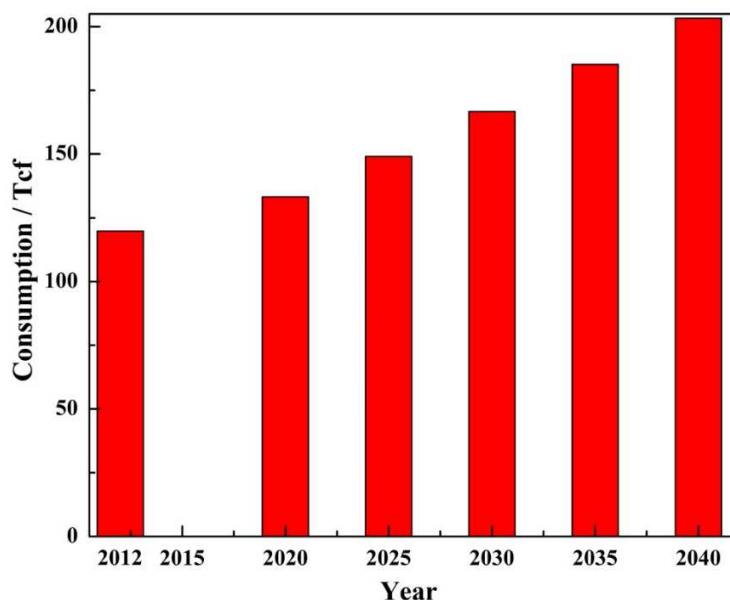


Figure 1.2. World natural gas consumption for 2012-2040. Data from Ref. [6].

Most of the natural gas reserves are located in remote areas, which are usually very far away from the areas of consumption. Transportation of methane through pipelines or via liquefaction over a long distance is not economically viable [1]. Flaring is widely used to dispose of natural gas produced at oil and gas facilities that lack sufficient infrastructure to capture all of the gas that is produced [7]. The volume of total flared gas was estimated to be 5.1 Tcf in 2012 [7] and the total value is equivalent to a market value of approximately 20 billion dollars [5]. As we know, methane is the main component of natural gas. Consequently, over many decades, there is an urge to convert methane on-site and on a large scale to transportable high-density energy sources or high value-added chemicals such as methanol, olefins and aromatics [1]. Figure 1.3 shows an overview of the different routes for the valorization of methane. The on-site conversion of methane is quite difficult, mainly due to the fact that methane is a very stable and symmetric molecule which does not possess any dipolar moment or functionality that would allow for directing chemical reactions [8].

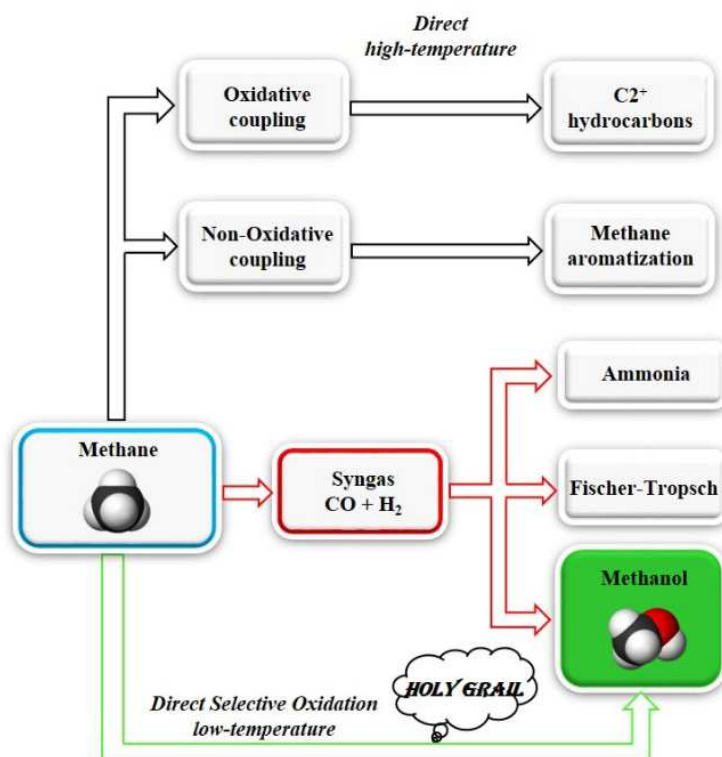
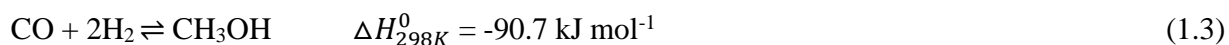
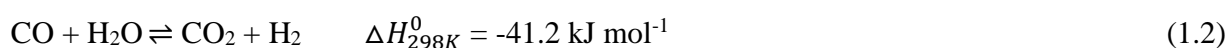
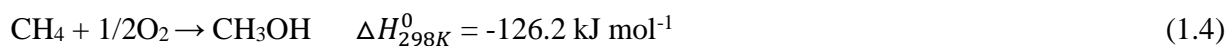


Figure 1.3. Overview of the different routes for the valorization of methane [8].

The carbon-hydrogen bond in methane possesses a very high bond energy ($104 \text{ kcal mol}^{-1}$ C-H bond), which usually requires high temperature in gas phase or other harsh conditions for activation and leads mostly to radical reactions with inherent low selectivities [9, 10]. Because of these reasons, nowadays an established route for methane utilization into useful chemicals and liquid fuels is only feasible via the endothermic steam reforming process (Equations 1.1 and 1.2) to produce syngas ($\text{H}_2 + \text{CO}$) followed by a Fischer-Tropsch or methanol synthesis (Equation 1.3) step to obtain hydrocarbon oxygenates [5]. However, these are energy-intensive and cost-intensive processes, which become profitable only at very large scales [11, 12]. Thus, alternative routes such as the one-step selective oxidation of methane to chemicals (Equation 1.4 shows as an example formation of methanol) and fuels are of considerable interest especially for decentralized smaller plants and received intensive investigations.





The selective oxidation of methane to value-added hydrocarbon oxygenates has profound meaning not only for chemical industry but also for academic research. Unfortunately, the products of selective oxidation of methane such as methanol, formaldehyde (FD) and formic acid (FA) are more easily oxidized to CO and/or CO₂ compared to methane. This makes the selective oxidation of methane to hydrocarbon oxygenates an extremely challenging task in catalysis.

1.2 Selective oxidation of methane using different oxidant

1.2.1 Selective oxidation of methane with SO₃

Due to the highly stable structure of methane and a very high bond energy (104 kcal mol⁻¹ C-H bond), higher temperatures are often required in gas-solid heterogeneous catalytic oxidation systems for methane activation. However, in liquid phase of homogeneous catalytic systems, as the molecular catalysts provides highly dispersed active sites as well as low resistance for heat and mass transport, the activation of C-H bond can be achieved even at low temperatures.

In 1969, Shilov and co-workers firstly reported the use of soluble molecular catalysts in acetic acid solution for the activation of methane [13]. After that, they continued their investigation of the activation of alkanes in solution using metal complexes as catalysts [14, 15]. Their work laid the foundation for the selective oxidation of methane in liquid phase by metal complexes. A remarkable review focused on the activation of C-H bonds by metal complexes was contributed by Shilov and Shul'Pin [16]. Inspired by this initial progress in molecular catalysis, Periana et al. investigated the oxidation of methane to methanol derivatives under concentrated sulfuric acid conditions providing SO₃ as oxidant and reported their results in two milestone publications [17, 18]. In an autoclave reactor, mercuric bisulfate was firstly used as catalysts and methane was oxidized to methanol via methyl bisulfate in the presence of concentrated sulfuric acid [17]. The reaction was conducted at 34.5 bar and 180 °C for 3 hours. A remarkable selectivity for methyl bisulfate of 85 % at a high methane conversion of 50 % was achieved. The yield of methyl bisulfate was around 43 % and the major side product was carbon dioxide. Methanol was obtained by hydrolysis of the methyl bisulfate. A possible catalytic cycle was proposed and shown in [Figure 1.4](#).

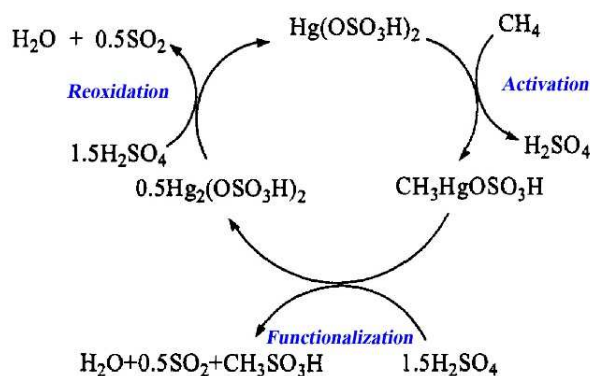


Figure 1.4. Proposed catalytic cycle for the Hg (II) catalyzed methane oxidation reaction [17].

If noble metal ions are used as catalysts they tend to be irreversibly reduced to elementary noble metal (causing the loss of the effective component of the catalyst) which leads to undesired complete combustion of the partially oxidized products [18]. Subsequently, in order to obtain a more stable catalyst, platinum bipyrimidine complexes were developed as catalysts by Periana et al. and showed to be more stable and efficient catalysts for the same reaction [18]. A very high methane conversion of 90 % with an 81 % selectivity for methyl bisulfate was obtained, thus led to the one-pass yield of methyl bisulfate being around 72 %, making it by far the highest one-pass yield for the selective oxidation of methane. A possible reaction mechanism for the oxidation of methane by [(2, 2'-bipyrimidine)PtCl₂] was proposed and shown in Figure 1.5. The process is supposed to proceed via electrophilic C-H activation by the coordinatively unsaturated (cus) Pt complex followed by the oxidation and functionalization steps [19]. A more recent study suggests that the success of “Periana” catalyst is because the methanol is protected as methyl bisulfate, which is substantially less reactive than methanol toward the catalyst. The bisulfate group protects the C-H bond in the product by making them less nucleophilic, thereby reducing the interaction with the electrophilic Pt complexes [20].

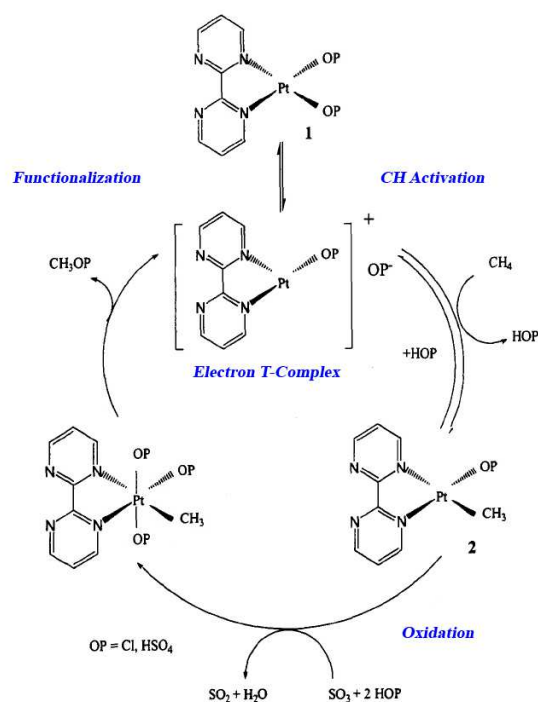


Figure 1.5. Proposed reaction mechanism for the oxidation of methane by $(bpy)PtCl_2$ [18].

Inspired by the success of the “Periana catalyst” and to overcome the separation and recycling problem of the molecular catalyst, Palkovits and co-workers recently prepared electrophilic Pt centers attached to a polymer, which was a covalent triazine-based framework (CTF), as solid catalyst for the oxidation of CH_4 in oleum (H_2SO_4 -30 % SO_3) [21, 22]. Two different routes were chosen, either an in situ pathway by simply combining CTF and the platinum precursor in the reaction mixture for the methane oxidation reaction ($K_2[PtCl_4]$ -CTF), or by pre-coordination of platinum (Pt-CTF) in a separate step [21]. Both of these two catalysts exhibited high activity for selective methane oxidation at 215 °C under 40 bar of CH_4 after 2.5 h of reaction. The turnover numbers (TONs) for $K_2[PtCl_4]$ -CTF and Pt-CTF catalysts reached 201 and 246, respectively. A catalyst performance comparable to that of the homogeneous catalyst systems of Periana et al. was obtained and these heterogeneous systems were stable over at least five recycling steps [21].

It is also noteworthy that iodine and iodine-containing compounds show considerable catalytic activity with concentrated H_2SO_4 in selective oxidation of methane and thus received intensive investigations recently [23-25]. Elemental iodine was dissolved in weak oleum and catalyzed the oxidation of methane to methyl bisulfate with a selectivity higher than 90 % and a yield of 45 %. I_2^+ is assumed to be the probable reactive species and the reaction mechanism was quite similar to

that of Hg^{2+} catalyst [23]. However, Davico believes that it is I^+ playing a vital role in the activation for C-H bond of methane instead of I_2^+ [24].

Although impressive catalytic results (such as high level of methane conversion and product yield) were obtained in the catalytic process based on concentrated H_2SO_4 , the disadvantages of it are also obvious. The corrosiveness of sulfuric acid, difficulties in the recycling of the catalyst, inevitable hydrolysis of methyl bisulfate, and the accumulation and re-oxidation of SO_2 [5, 26], thus hindered the commercialization of this process.

1.2.2 Selective oxidation of methane with N_2O

N_2O provides distinguished prospects in catalytic and non-catalytic oxidation chemistry due to its unique oxidative properties and it has received a considerable attention of researchers involved in searching for new approaches in selective transformation of methane in the late 1970s to early 1980s [27]. During this early period, representative work came from the research groups of Lunsford [28] and Somorjai [29]. Lunsford and co-workers used molybdenum supported on silica as the catalyst for the selective oxidation of methane with N_2O as the oxidant. A methane conversion of 3 % along with a combined selectivity to CH_3OH and HCHO of 78 % was achieved [28]. Silica-supported vanadium pentoxide was used as catalyst by Somorjai and co-workers. With a reactant mixture of CH_4 , N_2O , and H_2O , a total selectivity to CH_3OH and HCHO of 100 % at low methane conversions (around 0.2 %) and contact time (1.2 s) was reached at 460 °C [29]. The specificity of N_2O as a selective oxidant is one of the most interesting questions arising from the research of benzene oxidation to phenol over Fe-containing catalysts, in particular Fe-ZSM-5 zeolites [30]. Panov and co-workers believe that a unique active oxygen species, designated as α -oxygen (O_α), can be formed on Fe-ZSM-5, and this O_α species exhibit impressive selective oxidation ability for benzene to phenol [30-32] and methane to methanol [33, 34]. However, an extraction process using an appropriate solvent such as water or an acetonitrile aqueous solution is needed to obtain the CH_3OH generated on the surface of catalysts, revealing that this reaction system is not a catalytic cycle but a stoichiometric reaction between CH_4 and the α -oxygen.

Furthermore, Panov and co-workers proposed a potential mechanism of the α -sites' formation (shown in Figure 1.6) [35]. A reduced complex (II) could be formed from complex (I) upon oxygen desorption at elevated temperatures. The initial binuclear iron complex (I) may form via either a framework or extra-framework Fe species. Then it is assumed that complex (II) could transform

to stabilized complex (III), in which Fe_2^{2+} entities are strongly incorporated into a silicate fragment of the zeolite framework and have more distant positions. Complex (III) appears to be inert against dioxygen. However, complex (III) can be readily oxidized by N_2O into complex (IV) to give adsorbed O_α species [27, 35].

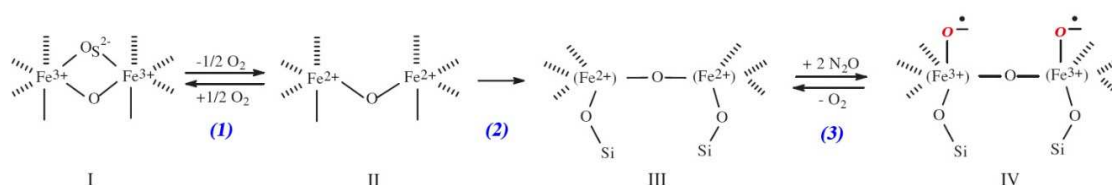


Figure 1.6. Mechanism of the α -sites' formation [35].

Wang and co-workers found that FePO_4 or supported FePO_4 showed excellent catalytic performances for the oxidation of methane by N_2O or O_2 to oxygenates and the reaction proved to be a true catalytic oxidation reaction [36, 37]. Over a 40 wt. % FePO_4 -MCM-41 catalyst, when O_2 was used as the oxidant at 500°C , a formaldehyde selectivity of 79.3 % with a methane conversion of 0.40 % was obtained. When switching the oxidant to N_2O and decreasing the temperature to 400°C , a total selectivity for methanol, formaldehyde and dimethyl ether (DME) of 96.6 % with a methane conversion of 0.98 % was achieved [37]. When the reaction temperature increased from 400°C to 450°C , the conversion of methane increased from 0.98 % to 3.0 %, however, the oxygenate selectivity dropped from 96.6 % to 82.1 % [37]. Kinetic studies indicated that the activation of oxygen occurs rapidly, while the activation of nitrous oxide proceeds at a comparable rate with the conversion of methane by the active oxygen species over both the supported and the unsupported catalysts [37]. A subsequent study confirmed that the presence of phosphorus is crucial for getting a high hydrocarbon oxygenates selectivity since the FeO_x -SBA-15 exhibited a very low oxygenate selectivity of 32.0 % and no methanol could be detected [38]. Thus, the phosphate groups surrounding the Fe sites played an important role for generating methanol as the primary partial oxidation product.

1.2.3 Selective oxidation of methane with O_2

Due to its easy availability and relative low cost, molecular oxygen or air have received much attention as oxidants in the study of the selective oxidation of methane. Since copper and iron have been found to be active sites in methanotrophic bacteria, in recent decades there have been intensive studies on Cu- or Fe-containing zeolites to develop bionic catalysts and using O_2 or air

as oxidant. These studies will be reviewed in sections 1.3.2 and 1.3.3. In the present section, publications reporting on Mo, V, and Co as heterogeneous catalysts using O₂ as oxidant to generate hydrocarbon oxygenates as products will be roughly reviewed.

In 1988, Spencer reported the partial oxidation of methane to formaldehyde by molecular oxygen over MoO₃-SiO₂ catalysts [39]. On Na-free MoO₃-SiO₂ catalysts, HCHO and CO₂ were generated in parallel via a common activation step and CO was produced via HCHO, and became the dominant oxidation product at high conversions [39]. Relative high selectivities (around 80 %) of HCHO were observed at very low CH₄ conversions (below 1 %) and the selectivity of HCHO decreased monotonically with increasing methane conversion. Trace quantities of methanol were detected and assumed to be an intermediate in formaldehyde formation [39]. Later on, the same group switched their focus to vanadium (V) and V₂O₅-SiO₂ catalysts for the study of the partial oxidation of CH₄ using molecular oxygen, and it was found that V₂O₅-SiO₂ catalysts to be more efficient when compared to MoO₃-SiO₂ catalysts [40]. Similarly to the observation obtained on MoO₃-SiO₂ catalysts, the selectivity of HCHO was found to decrease rapidly as the extent of reaction was increased and at the highest conversions (6.4 %), carbon monoxide was the main product [40]. It is interesting that a different reaction mechanism was found compared to the MoO₃-SiO₂ catalysts. Methane oxidation was found to follow a sequential reaction pathway, in which formaldehyde is directly formed from methane, carbon monoxide from formaldehyde, and carbon dioxide from carbon monoxide [40]. Based on the sequential mechanism and experimentally derived kinetic parameters, a reaction model was established.

In recent years, MoO₃-SiO₂ and V₂O₅-SiO₂ as conventional catalysts were extensively studied for the selective oxidation of methane using O₂ as oxidant and in most cases single-pass yields of HCHO were below 5 % [26, 41-43]. In terms of the reaction mechanism, the lattice oxygen species, particularly the terminal oxygen species (i.e. Mo=O and V=O), were assumed to be responsible for the oxidation of methane to HCHO [39, 40, 44, 45]. Such a mechanism is depicted in Equation 1.5 (methane is activated by the terminal oxygen species) and Equation 1.6 (the reduced sites are recovered by O₂) [41]:



This type of redox reaction mechanism is also known as the Mars-van Krevelen mechanism, which has been proposed for the selective oxidation of olefins to oxygenates [46-48]. However, based on isolated MoO_x species dispersed on SiO_2 (with a Mo loading of 0.44 Mo/nm^2), Bell and co-workers investigated the reaction mechanism for the selective oxidation of methane to HCHO using O_2 and a mechanism different from the Mars-van Krevelen mechanism was proposed [49, 50]. The Mo atoms in this catalyst were present as isolated, pentacoordinated molybdate species containing a single $\text{Mo}=\text{O}$ bond and it is proposed that the active oxygen species for CH_4 activation was not the lattice oxygen but might be a peroxide species generated by the activation of O_2 on the small concentration of isolated reduced molybdate species (Mo(IV)) thus leading to the formation of formaldehyde (Figure 1.7) [49]. This mechanism may also be applied to the supported VO_x catalysts, as isolated VO_x species are also needed for these catalysts for the selective oxidation of CH_4 to HCHO [26].

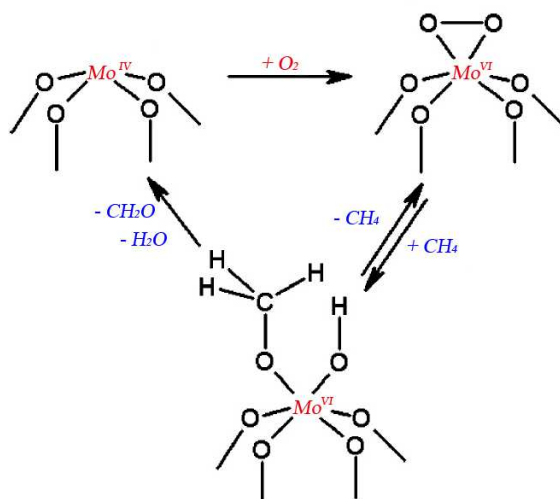


Figure 1.7. Proposed mechanism the selective oxidation of CH_4 at isolated, SiO_2 -supported MoO_x sites [49].

Cobalt as the active site of catalysts for methane oxidation also received intensive studies recently [51, 52]. Bitter and co-workers initially reported the selective oxidation of methane to methanol and formaldehyde at a low temperature over Co-ZSM-5 using air and the influence of the preparation method on the nature of the cobalt species was investigated [51]. On Co-ZSM-5 ($\text{Si/Al} = 17.5$) prepared by liquid ion-exchange at room temperature with a low Co content (0.9 wt. %), 80 % of Co species was proved to be isolated Co^{2+} and after the reaction (150 °C for 25 min in CH_4 and He flow), selectivities of 25 % and 75 % to CH_3OH and HCHO were obtained

respectively [51]. It was found that samples prepared by liquid ion-exchange at room temperature, leading to more isolated Co species, were most selective towards formaldehyde and the impregnated samples, containing mainly oxidic cobalt species (CoO and Co₃O₄), were more selective towards methanol [51]. Subsequently, the same group investigated the influence of alkaline and acid treatments of the zeolite Co-ZSM-5 agglomerates on the reactivity and selectivity of methane oxidation and confirmed that the higher fraction of isolated Co²⁺ species in the Co-ZSM-5 resulted in higher selectivity to HCHO [52]. However, the products had to be extracted from the surfaces of the catalysts using ethanol. Thus, the reaction is not a catalytic but stoichiometric reaction.

1.2.4 Selective oxidation of methane with H₂O₂

Hydrogen peroxide is widely used in chemical industry especially as an oxidant in oxidation processes, mainly due to its advantages of being environmentally friendly, having a high efficiency per weight of oxidant and being a liquid which is miscible with water and is relatively easy to handle [53]. The earliest related literature using H₂O₂ as oxidant for the oxidation of methane can be traced back to 1905 being the priority date of a patent by Lance and Elworthy, in which ferrous sulfate was used as catalyst and mixtures of methanol, formaldehyde and formic acid were obtained as the products [54]. Although from the economical point of view, H₂O₂ is usually more expensive than the C₁ oxygenates derived from methane (e.g., CH₃OH), the selective oxidation of methane by H₂O₂ is of fundamental significance [26] and received much attention recently.

Among the reactions between organic reactants and H₂O₂ with ferrous ion as a catalyst, there is a well-known reaction called Fenton's reaction, which was proposed by Fenton in 1894 that iron has a special oxygen transfer property, which could obviously improve the use of hydrogen peroxide as oxidant [55]. Nowadays, the Fenton's reaction is widely used to oxidize organic compounds and contaminants, e.g. for treatment of wastewaters. A typical Fenton's process consists in the reaction of Fe²⁺ species with H₂O₂ under strong acid conditions to generate highly reactive hydroxyl radicals (HO•) [56, 57]. Fe²⁺ is oxidized by hydrogen peroxide to Fe³⁺, forming a hydroxyl radical and a hydroxide ion. The stoichiometry of the reaction and the products formed are shown in Equation (1.7) [57]. As can be seen, Fenton's reaction consists basically in the oxidation of Fe²⁺ to Fe³⁺ by H₂O₂ as oxidizer. The important feature of the mechanism of the Fenton's reaction is the outer-sphere single electron transfer from Fe²⁺ to H₂O₂ generating hydroxyl radicals and

hydroxide anions [56, 57]. Accompanied with the true Fenton's reaction, other reactions (illustrated in Equations (1.8) - (1.13)) can also occur simultaneously and these parallel reactions are typically undesirable as they represent a loss of H₂O₂ without the generation of hydroxyl radicals [57].



In addition to iron salts, other transition metals that exhibit at least two oxidation states such as Pd, V, Cu, Co, Os, and Au can also promote the production of hydroxyl radicals from H₂O₂ [58-61]. The extremely powerful hydroxyl radical species can abstract one electron from an electron rich organic substrate or any other species present in the medium to form hydroxide anion [57] and thus leading to the corresponding oxidized products.

Sen and co-workers reported the oxidation of methane in the organic solvent of trifluoroacetic anhydride by using H₂O₂ as oxidant and Pd(II) ion as catalyst with a methanol derivative (methyl trifluoroacetate) as the product at a low temperature of 90 °C [58]. They assumed that the reaction follows an electrophilic pathway under mild conditions rather than a methyl radical pathway. Unfortunately, no detailed evidence was provided. Organic solvents such as acetonitrile were also used by Shul'pin and co-workers for the oxidation of CH₄ with H₂O₂ catalyzed by vanadium or iron complexes [59, 62]. In an autoclave reactor charged with a mixture of air and methane, by using [NBu₄]VO₃-pyrazine-2-carboxylic acid as the catalyst and in a acetonitrile solution mixed with aqueous H₂O₂, methane was oxidized to give methyl hydroperoxide (which can be easily reduced to methanol), formaldehyde and formic acid [59]. The catalytic oxidation of methane requires the presence of air and hydrogen peroxide and by using ¹⁸O₂ for isotope labeling, they

concluded that hydrogen peroxide only acts as a promoter while molecular oxygen is the true oxidant. They proposed that in the presence of the catalyst, hydrogen peroxide is an efficient source of hydroxyl radicals which can attack the alkane molecule (RH) abstracting a hydrogen atom to produce alkyl radicals (R•) which rapidly react with molecules of oxygen to yield peroxy radicals (ROO•) which then are transformed into ROOH [59]. Later on, the same group shifted their focus to Fe complexes. Iron(III) perchlorate, iron(III) chloride, iron(III) acetate and a binuclear iron(III) complex with 1,4,7-triazacyclononane were used as catalysts for alkane oxidation with hydrogen peroxide in acetonitrile and it was found that the ligand environment of iron ions plays a pivotal role [62]. The addition of chloride anions to the “naked” iron(III) cation switches the reaction mechanism from that proceeding through hydroxyl radicals to another mechanism which proceeds predominantly with participation of ferryl species [62]. Wang and co-workers investigated the selective oxidation of methane and ethane with H₂O₂ in aqueous medium by using various transition metal chlorides including FeCl₃, CoCl₂, RuCl₃, RhCl₃, PdCl₂, OsCl₃, IrCl₃, H₂PtCl₆, CuCl₂ and HAuCl₄ as catalysts [60]. Among the metal chlorides investigated, OsCl₃ exhibited the highest turnover frequency (TOF) for the formation of hydrocarbon oxygenates (mainly alcohols and aldehydes). With OsCl₃ as the catalyst, methyl hydroperoxide was also formed together with methanol and formaldehyde. At 90 °C, a TOF of 12h⁻¹ for the formed C₁ oxygenates (CH₃OH, HCHO and CH₃OOH) along with a selectivity of 61 % was obtained and CO₂ was found to be the main by-product [60]. UV-Vis spectroscopic measurements suggested that Os(III) was probably oxidized into an Os(IV) species by H₂O₂ in aqueous medium, forming HO• radicals, and the Os(IV) species might be involved in the oxygenation of methane. Hydroquinone was added as a radical scavenger and the reaction was quenched, indicating the oxidation of methane with H₂O₂ catalyzed by OsCl₃ proceeded *via* a radical pathway [60].

Inspired by the results achieved in the homogeneous systems, Hutchings and co-workers intensively investigated the selective oxidation of CH₄ by H₂O₂ in aqueous solution recently by using solid catalysts [61, 63-65]. Based on their former work of using copper-promoted Fe-silicalite-1 (denoted as Cu-silicalite-1/Fe-silicalite-1) as catalyst [63] (this work is described in detail in section 1.3.3), they developed TiO₂ supported Au-Pd alloy nanoparticles as catalysts for the selective oxidation of CH₄ by H₂O₂ in aqueous solution with CH₃OH and CH₃OOH as the main products [61]. In an autoclave reactor operated at a methane pressure of 30.5 bar, using a catalyst of 1 wt. % Au-Pd-TiO₂ (prepared by incipient wetness), the TOF of all the generated products was

6.85 h⁻¹ and the selectivities to C₁ oxygenates and CH₃OH were 85.4 % and 12.1 %, respectively. When increasing the reaction temperature from 30 °C to 90 °C, as expected, enhancements of TOFs could be observed, with a maximum TOF (25.7 h⁻¹) at 90 °C. Concomitantly the highest methanol selectivity (19 %) and a selectivity of C₁ oxygenates of 88.4 % were measured at 90 °C. An increase of the metal loading from 1 wt. % to 5 wt. % of Au-Pd-TiO₂ let the selectivity of CH₃OH increase to 49.3 % at a similar selectivity to total C₁ oxygenates of 90.3 %. However, the overall catalyst productivity was lower for the 5 wt. % metal-loaded catalyst which is due to the high H₂O₂ decomposition rate. Hence, a quite low reaction temperature of 2 °C was chosen and an oxygenate selectivity of 93.4 % (45.2 % to CH₃OH), a low H₂O₂ conversion (about 90 % left after reaction) and a high productivity were observed. Methyl hydroperoxide was found to be the primary reaction product being subsequently transformed to methanol and CO₂ in the presence of the catalyst, but no HCOOH could be found in the products for all the reaction conditions, which is different from the results based on Cu-silicalite-1/Fe-silicalite-1 catalysts [63]. Another difference to the Cu-silicalite-1/Fe-silicalite-1 catalysts is that CH₃• radicals have been detected by EPR under reaction conditions while this kind of radicals could not be observed over the Cu-silicalite-1/Fe-silicalite-1 catalysts. HO• radicals were also detected by EPR, thus, the reaction is proposed to proceed *via* a radical mechanism under the given conditions. In subsequent experiments they considered the occurrence of a hydroperoxy species generated in situ from molecular oxygen. As the 5 wt. % Au-Pd-TiO₂ catalyst is very efficient for the synthesis of H₂O₂ from H₂ and O₂ [66], experiments were performed using CH₄, H₂, and O₂ diluted with N₂ for the concurrent synthesis of hydrogen peroxide and eventual formation of methanol at 50 °C [61]. A similar productivity, but much higher CH₃OH selectivity (68.2 %) was obtained when using the in situ generated H₂O₂ as compared to the experiments performed with H₂O₂ at 50 °C over the 5 wt. % Au-Pd-TiO₂ catalyst. The in situ generation of H₂O₂ lead to a three-fold increase in reactivity as compared to the reaction performed using low amounts of H₂O₂, indicating that the use of oxygen is improved by adopting an in situ capture approach [61].

1.3 Selective oxidation of methane over Cu- and Fe-containing zeolites

In nature, methanotrophic bacteria are able to convert methane to methanol using methane monooxygenase enzymes (MMOs) [67, 68]. Di-iron sites in the soluble MMO and di-copper sites in the particulate MMO are attributed to be the active species [69]. These binuclear centers create bridged oxygen species sufficiently strong to attack the C-H bond of methane. Towards the

beginning of the 21st century, the research focus shifted from vanadium and molybdenum oxide catalysts to Fe- and Cu-containing zeolites [5]. Inspiration may come from the fact that di-iron sites and di-copper sites are active for methane oxidation and based on the findings that microporous zeolites, such as ZSM-5, mordenite, and SSZ-13 can stabilize binuclear centers similar to those present in MMOs.

1.3.1 Inspiration from methanotrophic bacteria

The members of a class of bacteria known as methanotrophs can convert CH_4 highly selective to CH_3OH via a mild and controlled oxidation process under atmospheric conditions using O_2 [67]. Generally, there are two types of MMO employed by the methanotrophs. One is a Fe-containing soluble methane monooxygenase (sMMO) and the other is a Cu-containing particulate methane monooxygenase (pMMO) which is membrane-bound [70]. These two enzymes show significant ability to generate CH_3OH by using O_2 for the oxidation of CH_4 . In particular, pMMO is found to be the most efficient CH_4 oxidizer so far and it is capable of catalytic oxidation of CH_4 at a TOF of approximately one CH_4 molecule per second per enzyme [71]. Obviously, understanding the structures and mechanisms behind these enzymes may clarify how to design efficient and powerful catalysts, which may eventually be applied in industrial-scale selective oxidation of CH_4 to CH_3OH and other hydrocarbon oxygenates.

sMMO is a multi-component enzyme that is composed of a hydroxylase for substrate oxidation, a reductase that delivers electrons to the active site, and a regulatory protein [72]. sMMO is the most well-characterized member of the bacterial multicomponent monooxygenase family and is the only member that can hydroxylate CH_4 [70]. Transient kinetic studies of sMMO revealed eight reaction cycle intermediates, providing the most comprehensive description of enzymatic O_2 activation and C-H bond oxidation currently available for any of the di-iron oxygenases [73] (Figure 1.8). In the reaction cycle of methane oxidation with O_2 conducted by sMMO, termed compound Q (Q) is thought to be the key intermediate of the sMMO.

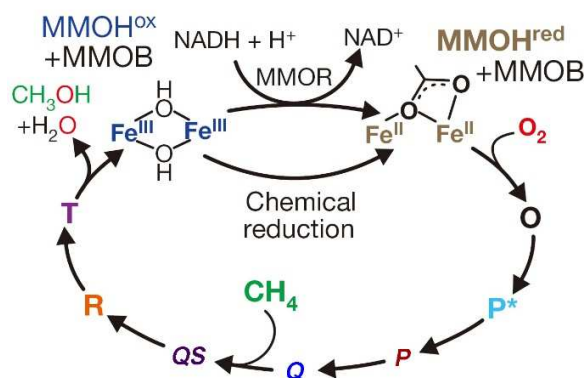


Figure 1.8. The catalytic cycle includes stable MMOH^{ox} and MMOH^{red} (diferrous sMMO hydroxylase) and detectable transient species O, P*, P, Q and T; transient states QS and R were predicted from kinetic, spectroscopic, and chemical studies [73].

By using time-resolved resonance Raman spectroscopy, Lipscomb and co-workers reported the core structures of Q and the following product complex, compound T. They proposed that Q possesses a bis- μ -oxo diamond core structure (Figure 1.9) and showed that both bridging oxygens originate from O_2 [73]. This observation strongly supports a homolytic mechanism for O-O bond cleavage.

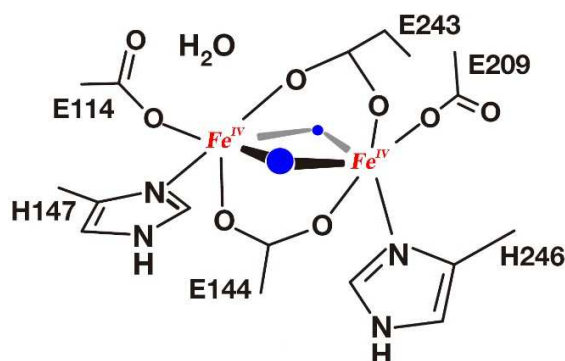


Figure 1.9. Proposed diamond-core structure of compound Q proposed in sMMO, having two irons (Fe^{IV}) bridged by oxygen atoms. The numbered groups in black surrounding the diamond core are the side chains of amino-acid residues. H, histidine residues; E, glutamate residues [73].

Unlike the case of sMMO, for which the information of the structure and mechanism is quite clear, such information of pMMO is still unclear and remains somewhat controversial. Compared to sMMO, pMMO is a membrane-bound protein that is extremely difficult to separate and purify from the plasma membrane for biochemical and biophysical research [70]. pMMO is an integral membrane metallo-enzyme which is composed of three subunits, pmoA, pmoB and pmoC, arranged in a trimeric $\alpha_3\beta_3\gamma_3$ polypeptide complex [74]. Recently, representative work in

determining the detailed structure and mechanism of pMMO comes from the research group of Rosenzweig and co-workers [69, 74, 75] and the research group of Chan and co-workers [70, 76, 77]. In 2004, Chan and co-workers investigated a purified pMMO-detergent complex and characterized the enzyme in pMMO-enriched membranes [76]. On the basis of the hyperfine splitting pattern of an electron paramagnetic resonance (EPR), it was proposed the purified pMMO is a multi-copper protein, with ca. 15 copper ions sequestered into five trinuclear copper clusters: two for dioxygen chemistry and alkane hydroxylation (catalytic or C-clusters) and three to provide a buffer of reducing equivalents to re-reduce the C-clusters for the following turnover (electron transfer or E-clusters) [76]. Later on, based on additional support by redox potentiometry and EPR spectroscopy, they confirmed their hypothesis of a ferromagnetically coupled tricopper cluster as the active hydroxylation site of pMMO [77]. In addition, the same group synthesized model tricopper clusters to provide further chemical evidence that a tricopper cluster mediates the enzyme's oxo-transfer chemistry [78]. These biomimetic models exhibit similar spectral properties and chemical reactivity to the putative tricopper clusters in pMMO and based on the DFT results, triangular tricopper clusters can utilize "single-state oxene" after activation by oxygen [78]. The turnover frequency and kinetic isotope effect predicted by DFT agreed very well with experimental data. However, Rosenzweig and co-workers hold a different opinion regarding to the structure of the active site. In 2005, based on the investigation of methanotroph *Methylococcus Capsulatus* (Bath), they determined the structure of pMMO [75]. The enzyme was proposed to be a trimer with a $\alpha_3\beta_3\gamma_3$ polypeptide arrangement. Figure 1.10 shows the proposed structure of pMMO. Two metal centers (modeled as mononuclear copper and binuclear copper) are located in the soluble region of each particulate methane monooxygenase alpha (pmoB) subunit and a third metal center occupied by zinc in the crystal is located within the membrane [75]. In 2010, Rosenzweig and co-workers continued their research on pMMO. They found that recombinant soluble pmoB fragments bound copper showed oxidation activity for propylene and methane. Destruction of each copper center in soluble pmoB indicates that the active site is a dicopper center [69]. The proposed structure of this dicopper center is shown in Figure 1.11.

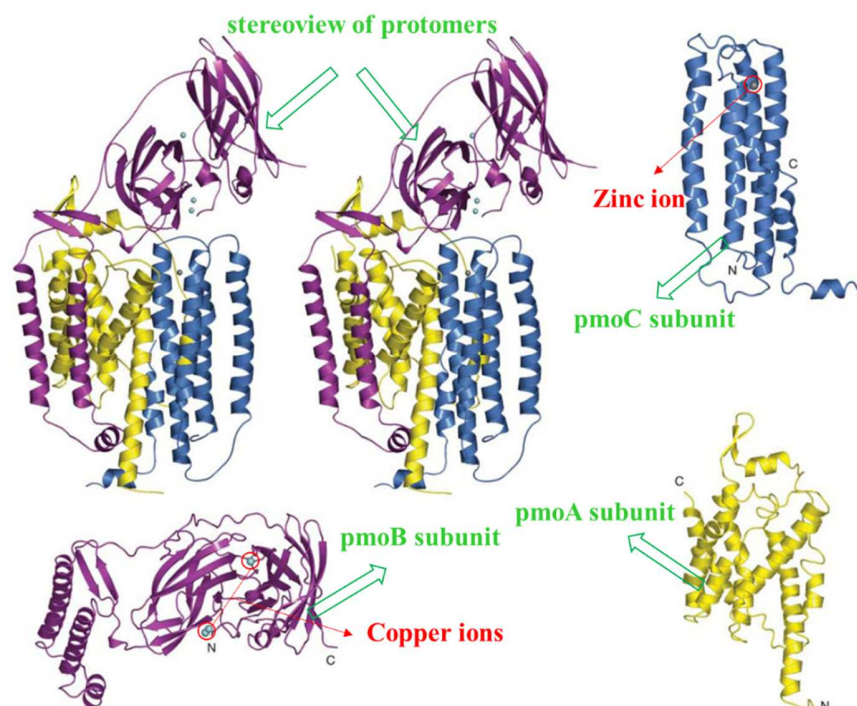


Figure 1.10. Proposed structure of pMMO subunits [75].

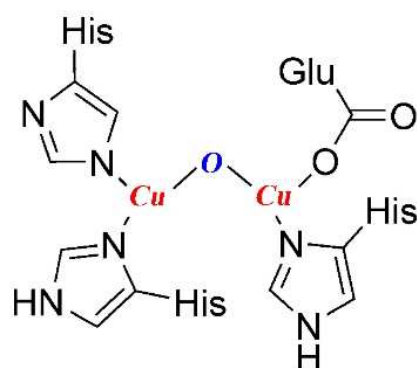


Figure 1.11. Proposed structure of the dicopper center as active sites in pMMO. From Ref. [5].

1.3.2 Selective oxidation of methane over Cu-containing zeolites

Inspired by the fact that there may exist Cu co-factors in MMOs, catalysts based on Cu zeolites proved to be active for the oxidation of methane and received intensive study over recent twenty years. However, the identification of the active site in these copper zeolites is still controversial. According to literature, they are roughly classified into three types: mononuclear Cu active sites, binuclear Cu active sites, and tri-nuclear Cu active sites [79].

Based on the detailed information obtained from pMMO and DFT calculation, bare mononuclear $[\text{CuO}]^+$ was predicted to be active in the activation of methane to methanol using O_2 [80, 81]. However, this prediction is very difficult to be experimentally proven, mainly due to the difficulties in obtaining sufficient amounts of $[\text{CuO}]^+$ to probe its reactivity [82]. Recently, Schwarz and co-workers successfully generated the bare $[\text{CuO}]^+$ cation in the gas phase and observed the efficient activation of methane at room temperature [83]. It was found that $[\text{CuO}]^+$ is able to efficiently activate methane at room temperature both by hydrogen abstraction (generated a product cation $[\text{CuOH}]^{*+}$) and by oxygen-atom transfer (generated methanol) [83]. Furthermore, the generated cation $[\text{CuOH}]^{*+}$ itself also homolytically cleaves the C-H bond of a second methane molecule, thus giving rise to the formation of a water complex ($[\text{Cu}(\text{OH}_2)]^+$) [83].

Compared to mononuclear Cu oxide species, binuclear Cu oxide species are much more widely investigated and acknowledged to be active sites for the activation of methane. A variety of synthetic ligands have been reported to assemble the binuclear Cu oxide active species and reactions of 2:1 mixtures of Cu(I) complexes with O_2 generally lead to the constitution of the corresponding dicopper peroxy or dicopper oxo complexes, as shown in Figure 1.12 [70].

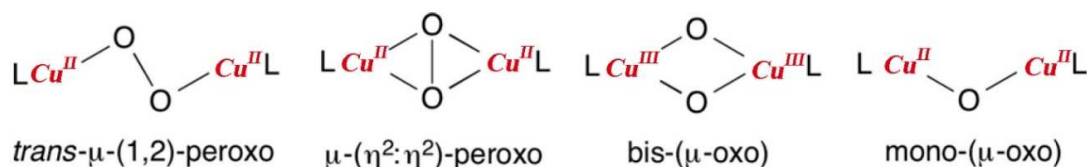


Figure 1.12. Activation of dioxygen by two Cu(I) centers [70].

In 2005, Groothaert et al. reported on the capability of the O_2 -activated Cu-ZSM-5 and Cu-MOR zeolites for selective conversion of methane to methanol and a bis(μ -oxo)dicopper core was proposed to be the active site, which was characterized by an intense UV-Vis band at 22700 cm^{-1} [84]. However, the determination of the active sites in Cu based zeolites is still not fully clear and in 2009, the same research group excluded their originally proposed bis(μ -oxo)dicopper site and instead proposed the active sites to be bent mono-(μ -oxo)dicupric species [85]. In their opinion, the absorption feature at 22700 cm^{-1} of UV-Vis spectroscopy is not sufficient to unambiguously define the nature of the active site and resonance enhanced Raman spectroscopy was used to obtain more clear information [85]. The oxygen activated Cu core is uniquely defined as a bent mono-(μ -oxo)dicupric site (Figure 1.13), according to the combination with density functional theory (DFT)

and normal coordinate analysis calculations [85]. Soon after, the same group reported the formation of an O₂-precursor of this reactive site and defined the precursor to be a μ-(η²:η²) peroxo dicopper(II) species, [Cu₂(O₂)]²⁺ [86]. The combination of resonance Raman experiments and UV-Vis absorption data illustrated that this [Cu₂(O₂)]²⁺ species transforms directly into the [Cu₂O]²⁺ reactive site and spectator Cu⁺ sites in the zeolite ion-exchange sites provide the two electrons required for the cleavage of the peroxo bond in the precursor [86]. Figure 1.14 shows a summary of this reaction pathway.

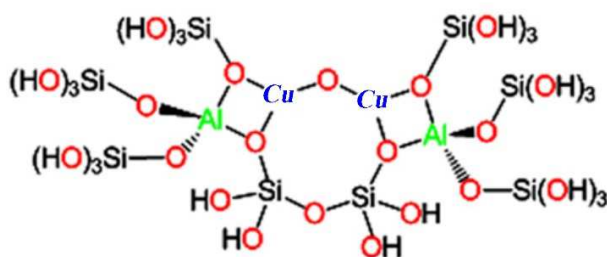


Figure 1.13. Structural models of ZSM-5 and the Cu₂O intermediate used for DFT calculations: Large model constructed from part of a 10-membered ring [85].

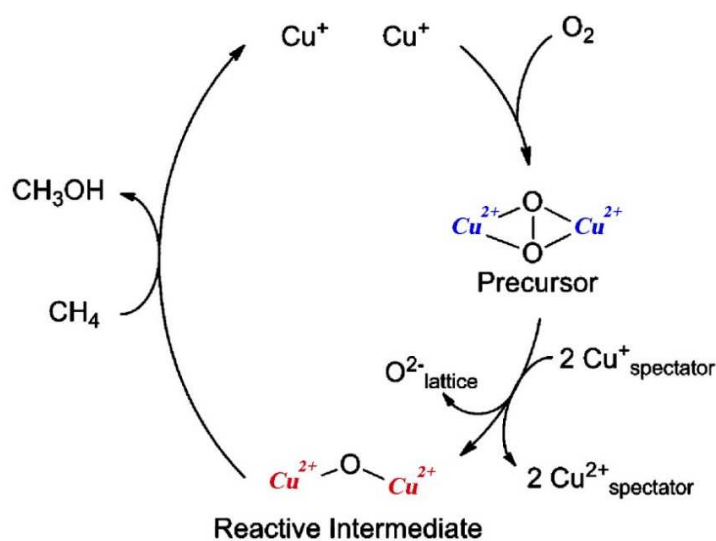


Figure 1.14. Proposed reaction pathway for Cu species [86].

Based on their former investigation of the structure of active sites in pMMO (tricopper clusters are proposed to be the active sites of this enzyme) [76, 77], Chan and co-workers successfully synthesized catalysts to mimic the structure of tricopper clusters and engaged the catalysts for the selective oxidation of methane [87, 88]. A tricopper complex of [Cu^ICu^ICu^I(7-N-Etppz)]¹⁺ (7-N-

Etpz corresponds to the ligand 3,3'-(1,4-diazepane-1,4-diyl)bis[1-(4-ethylpiperazine-1-yl)propan-2-ol]] was synthesized and the oxidation of CH₄ to methanol was mediated in acetonitrile [87]. The catalyst is activated by O₂ as in the single-turnover experiment and the spent catalyst is regenerated by two electron reduction by a molecule of H₂O₂ (Figure 1.15 A) [87]. It has also been found that when the steady state concentration of H₂O₂ exceeds about 10 equivalents, the abortive cycling starts (Figure 1.15 B) [87]. This homogenous catalyst was proved to be very efficient one, and later on, this research group successfully immobilized this molecular catalyst into mesoporous silica nanoparticles [88]. The mechanism of the immobilized catalyst is found to be similar with the homogenous one and it is interesting that the immobilized catalyst exhibits significantly higher productivities and TONs, corresponding to increased chemical yields [88]. The heterogeneous catalyst system is also robust and showed good reusability.

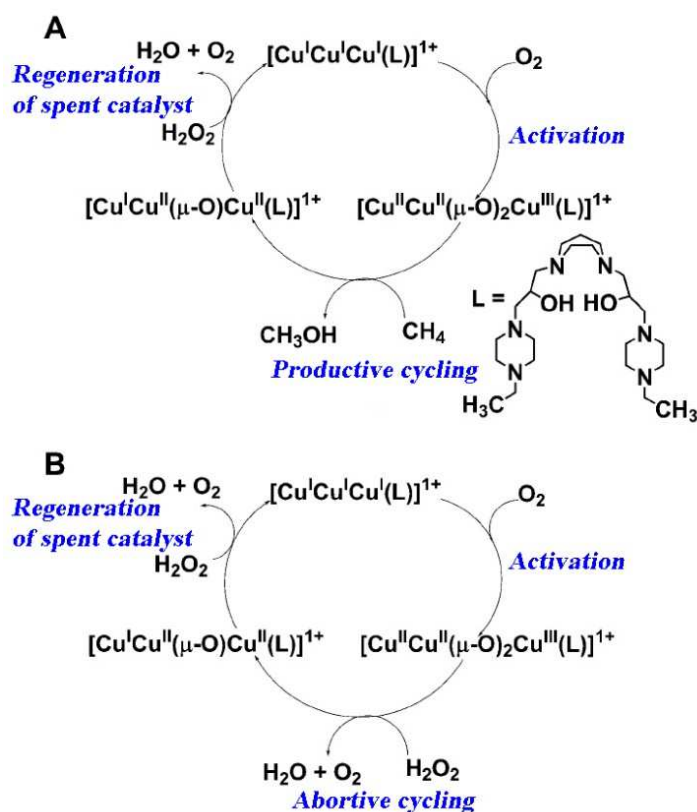


Figure 1.15. A) Productive cycling and B) abortive cycling in the oxidation of methane by O₂, mediated by the [Cu^ICu^ICu^I(7-N-Etpz)]¹⁺ complex in the presence of H₂O₂ as the sacrificial reductant [87].

Recently, it is reported that the mordenite micropores can provide a perfect confined environment for the highly selective stabilization of trinuclear copper-oxo clusters (shows in Figure 1.16) that

exhibit a high reactivity towards activation of C-H bonds in CH₄ and its subsequent transformation to methanol [89]. It is supposed that the 8-member ring side pockets in mordenite enhance the activity of the clusters by providing steric constraints similar to that in the subunits of pMMO [89].

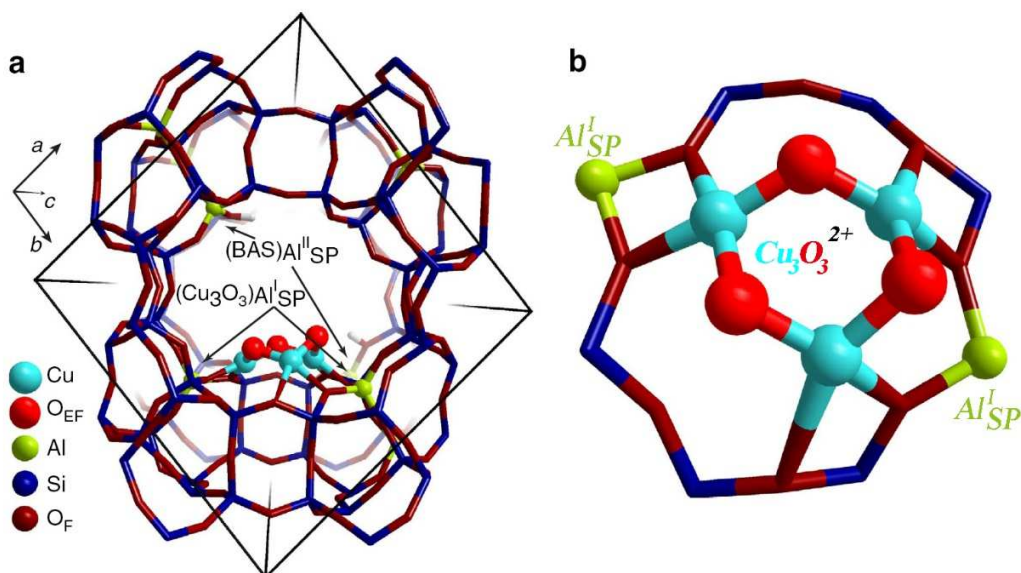


Figure 1.16. Structure and location of $[\text{Cu}_3(\mu\text{-O})_3]^{2+}$ cluster in mordenite predicted by DFT [89]. a), the main channel of MOR; b), the MOR side pocket

Regarding the Cu based on zeolites catalysts for the selective oxidation of methane, despite the uncertainty of the structure for active-sites, a significant disadvantage is that most reactions require several consecutive steps and the products has to be extracted from the catalysts by a solvent since they did not desorb themselves [89, 90]. In such a typical system, the process circulates between two very different temperatures: high temperature activation in oxygen to form active sites, and low temperature methane reaction and products extraction to prevent the over-oxidation of methane. Therefore, these processes are not catalytic but a typical chemical looping system with a loop composed of activation of the material, methane reaction, and products extraction steps [5]. Thus, some investigations are carried out to overcome this drawback or to obtain a closed catalytic cycle.

To overcome the drawback of tedious heating and cooling procedure performed throughout cycles, van Bokhoven and co-workers developed an isothermal methane-to-methanol process carried out at 200 °C [91]. In a typical cyclic process, online extraction with H₂O was performed after the activation of the catalyst and subsequent reaction with methane. All the steps were performed at

the same temperature. The characterization of the activated catalyst revealed that the active sites are small clusters of copper, and they are not necessarily di- or tricopper sites [91]. Narsimhan et al. reported the first demonstration of direct, catalytic oxidation of methane into methanol with molecular oxygen over Cu-exchanged zeolites at relative low reaction temperatures (210-225 °C) [92]. Unlike previous reported studies in which H₂O or other solvents were used for solid-liquid-extraction, they hydrolyzed surface-bound methoxy species by feeding a gas mixture of water vapor, molecular O₂ and CH₄. A variety of commercially available zeolites with different topologies were screened and it was found that the catalytic rates and apparent activation energies are affected by the zeolite topology, with cage-type zeolites (e.g., Cu-SSZ-13) showing the highest rates [92]. Based on their results, they argued that a closed catalytic cycle was obtained over H₂O-tolerant copper sites. Although very high selectivity to methanol was reported, however, this process still suffers from very poor productivity with an extremely low methane conversion.

1.3.3 Selective oxidation of methane over Fe-containing zeolites

Fe-containing zeolites show good performance in selective oxidation reactions not only for methane, but also for other alkanes [5, 26, 70]. Among these Fe-containing zeolites for the selective oxidation of methane, Fe-MFI zeolites were intensively studied, mainly due to their notable activity and high selectivity to the desired products [33-35, 63, 64, 93, 94].

On Fe-ZSM-5, a distinct form of surface oxygen, designated as α -oxygen, can be generated upon the activation of N₂O [30]. Panov and co-workers proposed that this particular oxygen species is responsible for the removal of hydrogen from methane, forming hydroxyl and methoxy groups at the α -sites [94]. However, the nature of the reactive intermediate α -oxygen is still not clear. In 2016, Snyder et al. defined the α -oxygen to be a mononuclear, high spin (S=2) Fe^{IV}=O species (Figure 1.17), based on the combined information from spectroscopic and computational studies of N₂O-activated Fe-zeolites [95].

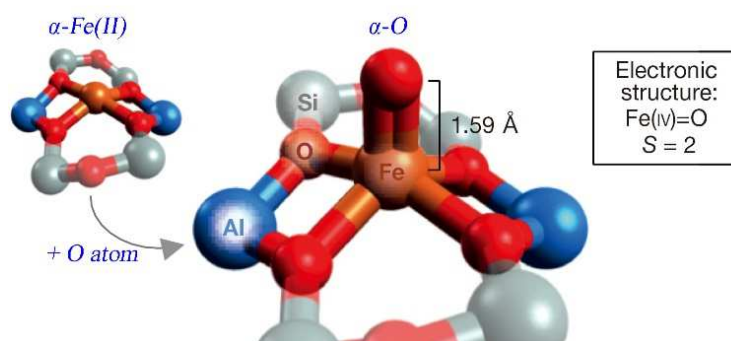


Figure 1.17. DFT-predicted structure of $\alpha\text{-O}$ in Fe-BEA [95].

The structure of the active sites for Fe-containing zeolites was proposed to be different under different conditions. Mainly, the active sites are attributed to be mononuclear Fe species or binuclear Fe species from literatures. An oxygen bridged binuclear Fe complex (iron-oxygen-iron bridge) was first proposed by Boudart and co-workers in 1970, based on a Mössbauer spectroscopic study of the reversible oxidation of ferrous ions in Y zeolite [96]. Later on, other research groups also demonstrated that Fe may exist as binuclear oxo cations and as very small particles of Fe oxide [97-99]. Chen and Sachtler initially developed a method for preparing Fe-ZSM-5 catalyst by sublimation of FeCl_3 into the cavities of H-ZSM-5 with a Fe loading corresponding to Fe/Al ratios of up to 1 [99]. This method is also called chemical vapor deposition (CVD) in literature. It was found that Fe is located at the exchange sites of the zeolite and this catalyst was very active and selective in the catalytic reduction of NO_x with *iso*-butane [99]. An oxygen bridged binuclear Fe complex of the type $[(\text{HO})\text{Fe}-\text{O}-\text{Fe}(\text{OH})]^{2+}$ was assumed to be the active Fe species [99]. However, no detailed characterization by spectroscopy was supplied and thus making their assumption doubtful. After the publication of this work, intensive research emerged for the investigation of Fe-ZSM-5 catalysts prepared by CVD using FeCl_3 as the Fe precursor and more detailed information was obtained to unravel the structure of the active Fe species [100, 101]. Marturano et al. investigated the state of Fe in Fe-ZSM-5 samples prepared by CVD using FeCl_3 as the Fe precursor by extended X-Ray absorption fine structure (EXAFS), infrared spectroscopy (IR) and nitrogen adsorption measurements [97]. EXAFS revealed the presence of diferric (hydr)oxo-bridged binuclear clusters (Figure 1.18) with a structure different to the one proposed by Sachtler and co-workers [99] and being quite similar to that of the methane monooxygenase hydroxylase (MMOH) [97]. IR indicates that binuclear iron complexes are located at the ion-exchange sites of the zeolite, compensating for one or two lattice charges and

the remaining charge-compensating sites are the Brønsted hydroxyls group [97]. This is the first time that direct experimental evidences clearly demonstrated the presence of binuclear Fe clusters in Fe-ZSM-5 catalysts. Almost at the same time, Koningsberger and co-workers by using EXAFS and X-ray absorption near edge structure (XANES), also confirmed the stable binuclear iron oxo/hydroxo-complexes in Fe-ZSM-5 prepared through the CVD technique [102].

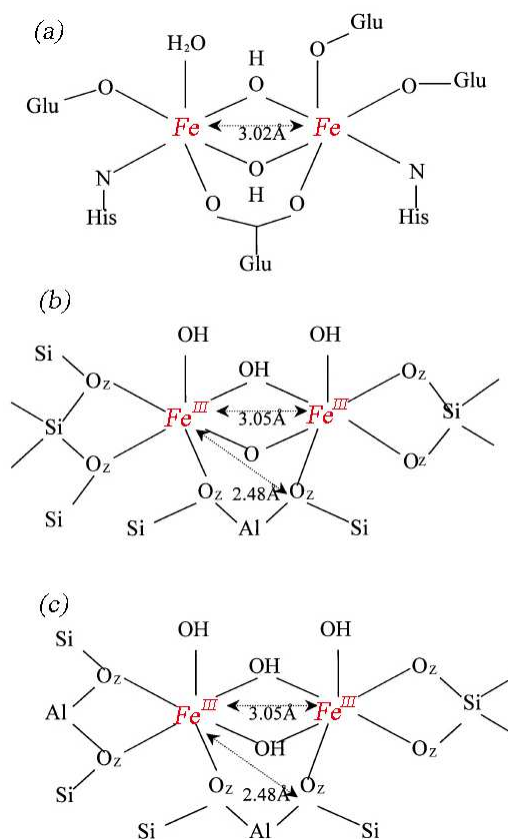


Figure 1.18. (a) Structure of active center in MMOH as reported in [103] and proposed Fe_2O_2 -type clusters in Fe-ZSM-5 compensating (b) one or (c) two lattice charges [97].

Analogous to the attribution of the active sites in Fe-ZSM-5 zeolites being binuclear Fe species, mononuclear Fe species are also thought to be the active sites in Fe-ZSM-5 zeolites for the selective oxidation of methane, hydroxylation of benzene to phenol and the decomposition of N_2O . Representative work come from the research group of Bell and co-workers [93, 104, 105]. Based on DFT calculations and experimental evidence, cations such as $[\text{Fe}(\text{OH})_2]^+$ or $[\text{FeO}]^+$ which are proposed to be the mononuclear Fe oxide species, can be accommodated to the isolated charge-exchange sites without any constraints by the Fe/Al ratio of the zeolite [104, 105]. While for the

binuclear cations such as $[M-O-M]^{2+}$, obvious constraints emerge when the Fe/Al ratio is larger than 24, as the distance between two Al atoms in next nearest neighbors T sites is too large to compensate these binuclear cations [105]. Thus, they argue that a significant fraction of the Fe^{3+} cations exchanged into ZSM-5 ($Si/Al \geq 25$) is present as isolated cations associated with a single charge-exchange site [104]. They also experimentally proved that mononuclear Fe species in SBA-15 are very active for oxidations of alkanes, alkenes, and arenes using hydrogen peroxide as the oxidant [106]. Furthermore, the formation of methanol on Fe/Al-MFI *via* the oxidation of methane by nitrous oxide was investigated and mononuclear Fe migrated from the lattice after calcination and stabilized at cation-exchange sites associated with framework Al atoms was assumed to be the active site [93]. A proposed reaction sequence for the formation of methoxy species is shown in Figure 1.19 [93].

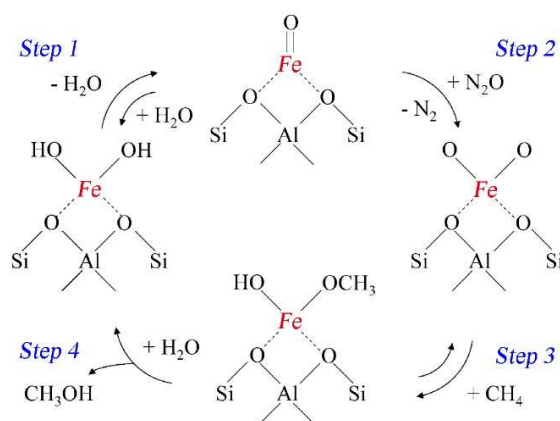


Figure 1.19. Proposed reaction sequence for the formation of methoxy species on Fe and Si sites [93].

Recently, Hutchings and co-workers used Cu-promoted Fe-containing MFI zeolites as catalysts for the selective oxidation of CH_4 to CH_3OH with H_2O_2 as oxidant in aqueous medium [63, 64, 107, 108]. With a physical mixture of Fe-silicalite-1 and Cu-silicalite-1 as the catalyst (denoted as Cu-silicalite-1/Fe-silicalite-1) and under optimal reaction conditions in an autoclave reactor, a methane conversion of 10.1 % with a CH_3OH selectivity of 93.0 %, together with a high TOF related to Fe of $70 h^{-1}$ and volumetric productivity of $4.7 \times 10^{-9} mol \cdot ml^{-1} s^{-1}$ were obtained [63]. Main oxygenate products were CH_3OOH , CH_3OH , $HCOOH$ and CO_2 . After 5 cycles of repeated use, the catalyst still showed a good catalytic performance without significant deactivation and no leaching of iron species was detected during the repeated cycles [63, 108].

Fe was proved to be the active site while Cu did not show a direct methane activation ability and even a trace amount of Fe (Fe content, 0.014 wt. %) in the commercial ZSM-5 already showed efficient activity for the selective oxidation of CH₄ by H₂O₂ [63]. The Fe in the framework of hydrothermally synthesized Fe-silicalite-1 was found migrated to extra-framework positions after the template removal and calcination and these extra-framework Fe oxide species were proved to be the active sites [63]. The specific geometrical environment of the extra-framework Fe species was investigated by EXAFS and combined with the results of periodic DFT calculations, binuclear iron complexes of [Fe₂(μ₂-OH)₂(OH)₂(H₂O)₂]²⁺ were attributed to be the active sites and a catalytic cycle for the oxidation of methane was also proposed (Figure 1.20) [63, 108]. Based on DFT calculations, a high-valent iron-oxo species of Fe⁴⁺=O was assumed to be responsible for the activation of CH₄, leading to the formation of an adsorbed CH₃OOH as the product with the help of the adjacent Fe-OOH site (Figure 1.20) [63].

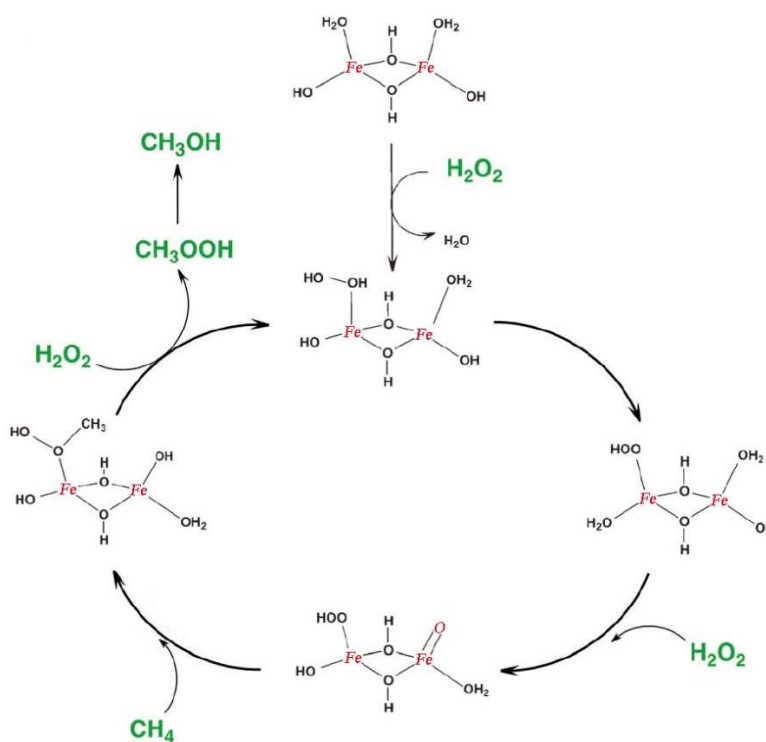


Figure 1.20. Proposed reaction mechanism for selective oxidation of CH₄ over Fe-ZSM-5 or Fe-silicalite-1 using H₂O₂ [63].

Radical scavengers were added into the reaction system and the absence of methyl radical signals in the EPR spectra was in agreement with the reaction mechanism they proposed [63]. The absence

of methyl radicals also suggested that the methane activation mechanism is different from that of α -O or Fenton's reagent [63]. The kinetic studies further confirmed that methyl hydroperoxide (CH_3OOH , MHP) was the primary reaction product followed by the consequent conversion to CH_3OH and HCOOH . Over Fe-silicalite-1 or Fe-ZSM-5 without presence of Cu, HCOOH was the main product, which was supposed to be the over-oxidation of formed CH_3OH due to the presence of OH radicals [63]. After the addition of Cu species either as Cu^{2+} in the reaction solution or as copper oxide in the catalyst in Fe-containing silicalite-1 or ZSM-5, the selectivity of CH_3OH increased a lot while almost maintaining the same level of CH_4 conversion [63, 107]. Combined with the results of adding Na_2SO_3 into the system as the scavenger of OH radicals, the authors proposed that the role of the Cu-containing component is for decreasing the concentration of the OH radicals thus retarding the over-oxidation of CH_3OH . The mechanism is illustrated in Figure 1.21.

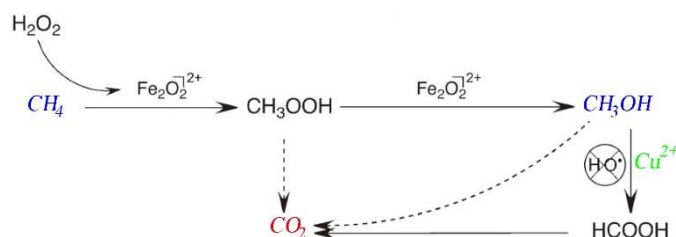


Figure 1.21. A proposed reaction scheme for the oxidation of methane and the function of Cu component [63].

Based on the success for the selective oxidation of methane to methanol in the autoclave reactor, later on, Hutchings and co-workers transferred the reaction into a fixed-bed reactor [64]. However, it was found that with the same catalyst, the TOFs dropped by nearly two orders of magnitude compared to the batch reactor and a low methane conversion of 0.5 % even at optimized condition was obtained [64]. This significant decline of the reaction performance observed in the fixed-bed reactor let the authors assume that severe mass transport limitations occur during the reaction [64].

1.4 Preparation of Fe-containing MFI zeolites

Fe-containing MFI zeolites were intensively investigated by many researchers due to their good performance not only in the selective oxidation of methane, but also in the hydroxylation of benzene to phenol [30, 31, 109-111], the selective catalytic reduction of NO_x [99, 112-114], and the decomposition of N_2O [115-117]. Although these reactions are different from the selective

oxidation of methane, similar state-of-the-art for the catalysts of Fe-MFI zeolites could be shared and thus can also shine light for the investigation of this work.

Generally, there are two main preparation routes to disperse Fe species inside the zeolite channels to get Fe-containing MFI zeolites [118]. One route comprises first the direct hydrothermal synthesis to obtain MFI zeolites containing isomorphously substituted Fe^{3+} and second the controlled migration of iron to extra-framework positions. The other route involves post-synthetic methods for loading Fe to the MFI zeolite after synthesis by liquid or solid state ion exchange, by impregnation, and by chemical vapor deposition (CVD). In this section, these two different routes and the corresponding state-of-the-art are described.

1.4.1 Direct hydrothermal synthesis

Fe-containing MFI zeolites prepared by the direct hydrothermal synthesis method have been proven to possess sufficient stability and selectivity to be promising catalysts in selective oxidation reactions of industrial interest [118]. Isomorphous substitution of a certain fraction of Si^{4+} with Fe^{3+} in the framework of silicalite-1 leads to the structure of Fe-silicalite-1. The framework of silicalite-1 is electrically neutral and after the introduction of Fe^{3+} species into the zeolite framework, an extra negative charge appears in the framework which has to be compensated by cations, e.g. by protons in the form of bridged hydroxyls (Fe-OH-Si) possessing an acid strength very close to that of H-ZSM-5 [119]. It is reported that the framework stability of Fe-silicalite-1 is lower compared to that of ZSM-5, in which Si^{4+} is isomorphously substituted with Al^{3+} . During the calcination for the removal of the organic template, partial cleavage of bonds connecting iron and oxygen atoms in the zeolite lattice is observed, leading to a migration of iron species to extra-framework positions [118-122]. These extra-framework iron species show very special catalytic activities in selective oxidation, xylene isomerization and ethylbenzene dehydrogenation reactions [63, 64, 122, 123].

Bordiga and co-workers investigated the structure and reactivity of framework and extra-framework Fe species in Fe-silicalite-1 by using IR, Raman, UV-Vis, EPR, XANES, EXAFS, and TPR techniques to determine the local environment of Fe species after thermal treatments and interaction with adsorbents [119]. It was found that for the prepared Fe-silicalite-1 containing organic template, isolated Fe^{3+} species locate in the framework in substitution positions and these Fe^{3+} species are in tetrahedral symmetry. However, the calcination procedure for the removal of

template causes the partial cleavage of bonds connecting iron with the oxygen of the framework, leading to the formation of extra-framework Fe oxide aggregates (possibly clustered $(\text{Fe}_2\text{O}_3)_n$ species) and the collapse of the tetrahedral structure, especially at a higher calcination temperature [119]. Later on, the same research group further investigated the structure, oxidation state and mutual interaction of the Fe species dislodged from the tetrahedral framework positions by a systematic spectroscopic study of Fe-silicalite-1 samples characterized by different iron content, activation temperature and redox treatments [118]. Based on the obtained results, they proposed that during the calcination procedure, the total migration of Fe into extra-framework position produces nascent FeOOH and FeO species and partially hydroxylated nests or nano-cavities. A $\text{Fe}^{3+} \rightarrow \text{Fe}^{2+}$ reduction of migrated Fe is accompanied. These nascent extra-framework species can travel along the channels and react with SiOH or strained SiOSi groups, and residual Brønsted Si(OH)Fe sites, leading to the formation of isolated or binuclear grafted Fe species [118]. Figure 1.22 briefly illustrates such potential reactions. Those extra-framework FeOOH and FeO species which have not reacted with the host matrix, can lead to $(\text{Fe}_2\text{O}_3)_n$, $(\text{Fe}_3\text{O}_4)_n$ or $(\text{FeO})_n$ larger Fe-oxide aggregates which do not adsorb CO, N_2O or NO and they are assumed to be inactive Fe species [118]. Thus, a very complex family of extra-framework Fe species is formed after the calcination procedure.

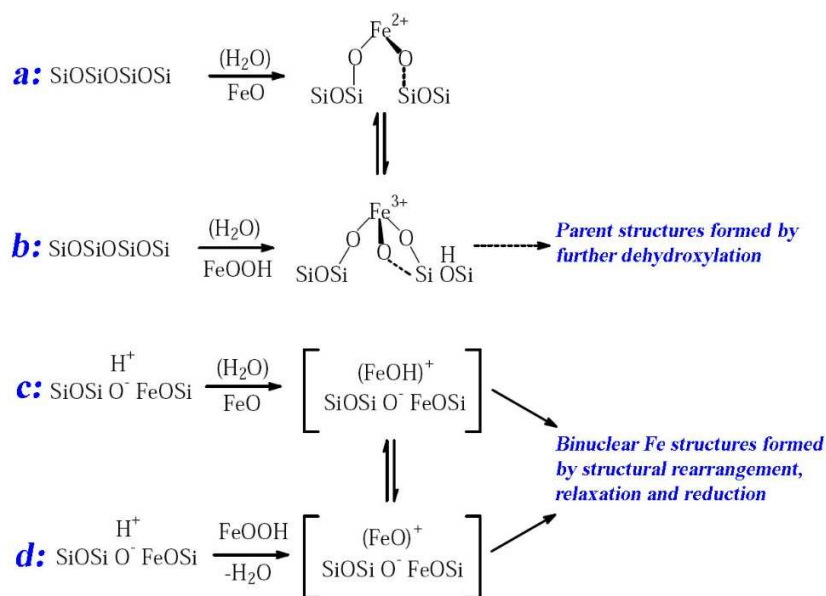


Figure 1.22. Proposed potential reactions of extra-framework Fe species with the host matrix (residual Brønsted sites and/or zeolite walls) [118].

1.4.2 Post-synthetic methods

Another important approach for dispersing Fe species inside the zeolite channels to obtain Fe-containing MFI catalysts are post-synthetic methods for loading Fe on ZSM-5. Various post-synthetic methods such as impregnation, liquid ion exchange (LIE), solid state ion exchange (SSIE), and chemical vapor deposition (CVD) are widely used in literature to obtain Fe-containing MFI catalysts [99, 112-114, 116].

Liquid ion exchange is commonly used for preparing metal-exchanged zeolites. In this approach [113], the zeolite is added to the corresponding metal salt solution (aqueous and/or organic) under continuous stirring. After a certain period of time, the mixture is filtered followed by the washing of the precipitate. These steps are usually repeated several times to obtain a desired content of the metal. Shishkin et al. [113] have prepared Fe-ZSM-5 catalysts by different post-synthetic methods: wetness impregnation using $\text{Fe}(\text{NO}_3)_3$ as Fe precursor and either methanol or 50 wt. % methanol in water as solvent, and liquid ion exchange using FeCl_2 (aqueous solution) as Fe precursor. Based on their obtained results, it was concluded that the post-synthetic method for the preparation of Fe-ZSM-5 catalyst is of significant importance for the activity and selectivity for selective catalytic reduction of NO_x and the most active catalyst is prepared by using liquid ion exchange with FeCl_2 as the Fe precursor [113].

For the solid state ion exchange method for the preparation of transition metal exchanged zeolites, a metal salt (usually chloride) is firstly fully mixed with the H- or NH_4 -form of the zeolite powder followed by heating in air, inert atmosphere or vacuum. During the thermal treatment, the solid-state interaction occurs which is accompanied by evolution of HCl or NH_4Cl gases, respectively [124]. Compared to LIE, SSIE showed several advantages. It allows the exchange of multivalent cations into the zeolite pore system, which is usually very difficult because of the formed large size of the hydrated metal complex in aqueous phase [125]. In addition, it may create some active sites that are different from those obtained by aqueous exchange [125]. Furthermore, it allows the control of the metal loading and it is more reproducible compared to LIE [124]. Grünert and co-workers investigated the role of NO_2 in the selective catalytic reduction of NO_x over Fe-ZSM-5 catalysts [112]. The catalysts were prepared by different post-synthetic methods such as improved liquid ion exchange, chemical vapor deposition and solid state ion exchange. It was found that the potential of preparation procedures to improve the activity by increasing the Fe content was very

different and the best performance was achieved over the catalysts prepared by solid state ion exchange with FeCl_3 as the Fe precursor [112]. Hellgardt and co-workers [126] investigated the selective oxidation of methane to methanol over Cu and/or Fe exchanged zeolites prepared by solid state ion exchange and wetness impregnation, at similar reaction conditions to Hutchings's work [63]. They found that, by decreasing the Si/Al ratio of Fe-ZSM-5 catalysts and thus increasing the number of acid sites, a significant enhancement of catalytic activity was observed. They proposed that Brønsted acid sites play an important role for the formation of a special structure of active extra-framework Fe species by providing appropriate positions for them.

To overcome the difficulty for obtaining a Fe loading corresponding to a Fe/Al ratio of 1 by ion exchange methods for the preparation of Fe-ZSM-5 catalysts, Chen and Sachtler initially prepared Fe-ZSM-5 catalysts by sublimation of FeCl_3 into the cavities of H-ZSM-5 with a Fe loading corresponding to Fe/Al ratios of up to 1 [99]. This method is the so-called chemical vapor deposition (CVD). An oxygen bridged binuclear Fe complex of the type $[(\text{HO})\text{Fe}-\text{O}-\text{Fe}(\text{OH})]^{2+}$ was assumed to be the active Fe species for the selective catalytic reduction of NO_x with *iso*-butane [99]. Intensive research emerged for the investigation of Fe-ZSM-5 catalysts prepared by the CVD method after their work. As described in the section 1.3.3, representative work comes from Marturano et al. [97] and Koningsberger and co-workers [102], in which direct experimental evidences clearly demonstrated the presence of binuclear Fe clusters in Fe-ZSM-5 catalysts.

For the post-synthetic method of preparation of metal oxide dispersed on porous materials, the molecular designed dispersion method (MDD) was developed to deposit highly dispersed layers of metal oxides without the formation of crystals [127-129]. The MDD method is based on the reaction of an acetylacetonate metal complex with the surface hydroxyls of the support materials. The acetylacetonate metal complex can react with the supports by a hydrogen bonding mechanism between an acetylacetonate ligand and surface OH groups on the pore walls, or by a ligand-exchange mechanism resulting in a covalent metal-oxygen bond. Figure 1.23 illustrates the potential mechanism of the MDD method. The large acetylacetonate ligands reduce the probability of metal clustering, and by that allowing a good dispersion of the metals [129]. In order to obtain highly dispersed Fe species in the supports of H-ZSM-5 and silicalite-1, the post-synthetic method of MDD was also adopted by using $\text{Fe}(\text{acac})_3$ or $\text{Fe}(\text{acac})_2$ as the precursor of Fe in this work.

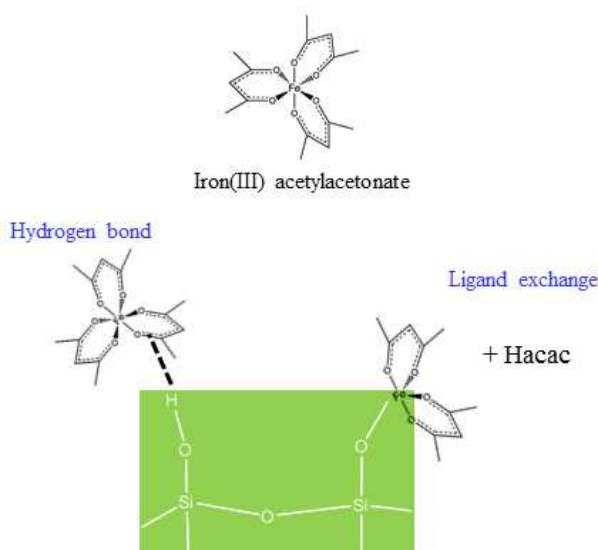


Figure 1.23. The potential mechanism of the MDD method by using $\text{Fe}(\text{acac})_3$ as the precursor of Fe.

1.5 Aim of this work

Although the selective oxidation of methane to value-added hydrocarbon oxygenates has been widely investigated in literature, until now there is still no efficient and economical route available for the large-scale industrial application of this chemical reaction. The work recently carried out by the group of Hutchings by using non-noble metal catalysts (Cu-promoted Fe-containing MFI zeolites) for the selective oxidation of methane to CH_3OH with H_2O_2 as oxidant in aqueous medium showed high application potential [63, 107, 108]. In an autoclave reactor, a high CH_3OH selectivity of 93.0 % with a relative high methane conversion of 10.1 %, together with high values of TOF (70 h^{-1}) and volumetric productivity ($4.7 \times 10^{-9} \text{ mol} \cdot \text{ml}^{-1} \cdot \text{s}^{-1}$) were obtained [63]. However, when the reaction was transferred to a continuous fixed-bed reactor, the catalytic performance dropped by three orders of magnitude due to severe mass transport limitations occurring during the reaction [64]. Becoming aware of the severe mass transport limitations, the starting point of this thesis was triggered.

The work presented in this thesis deals with the selective oxidation of methane to hydrocarbon oxygenates using aqueous H_2O_2 as an oxidant over Fe-containing MFI zeolites. The aim of this work is to improve the catalytic performance by intensifying the mass transport, adapting reaction conditions and optimizing the preparation of Fe-containing MFI zeolites. The chosen approach can be briefly summarized as follows:

1. Sub-micrometer sized Cu-silicalite-1/Fe-silicalite-1 was prepared and a micro fixed-bed reactor was used to intensify internal and external mass transport of the overall reaction. The reaction conditions were adapted, these adapted reaction conditions and the micro fixed-bed reactor were used in the following investigations.
2. A series of sub-micrometer and micrometer sized crystals of Fe-silicalite-1 were synthesized and the influence of different calcination temperatures, different Fe contents, different crystal sizes and different acidities of Fe-silicalite-1 to the selective oxidation of methane was studied.
3. Sub-micrometer sized crystals of H-ZSM-5 and silicalite-1 were synthesized. Different post-synthetic methods and different Fe precursors were used for Fe loading based on self-synthesized MFI zeolites. Their catalytic performance was carried out and compared.

The experimental setup and all applied methods are described in detail in chapter 2. In chapter 3 the optimization of catalyst performance in a micro fixed-bed reactor is reported. The experimental results on the selective oxidation of methane over different Fe-silicalite-1 catalysts can be found in chapter 4. In the subsequent chapter 5 the preparation and performance of different post-synthesized Fe-containing MFI zeolites in the selective oxidation of methane is described. At the end, the conclusions are summarized in chapter 6 and suggestions for future investigations are presented.

2 Experimental methods

All the chemicals that were used in this work are listed in Table 2.1. All the chemicals were used as received without further purification.

Table 2.1. Chemicals used in this work

Chemical	Producer, Purity/Composition
Aerosil 130	Evonik Degussa GmbH, silica, ≥ 99 %
Aluminum isopropoxide	Sigma-Aldrich, trace metals basis
Ammonia 3.8	Westfalen AG, 99.98 vol. %
Ammonium fluoride	Fluka, ≥ 98 %
Ammonium nitrate	Merck, ≥ 95 %
Cerium(IV) sulfate	Fluka, 0.1M (0.1N)
Chloroform solution	Sigma Aldrich, anhydrous, ≥ 99 %
Copper(II) acetate monohydrate	Fluka, ≥ 99 %
Copper(II) acetylacetonate	Sigma-Aldrich, trace metals basis
Ferric citrate	Sigma-Aldrich, ≥ 98 %
Ferroun indicator solution	Merck, 0.025M
Formaldehyde solution	Sigma Aldrich, 37 wt. % in water
Formic acid solution	Sigma Aldrich, 1.0 M in water, HPLC grade
Helium 4.6	Westfalen AG, 99.996 vol. %
Hydrogen 5.0	Westfalen AG, 99.999 vol. %
Hydrogen peroxide solution	Sigma-Aldrich, ≥ 30 %, for trace analysis
Iron (II) acetylacetonate	Chemos, 99 % / Fe(acac) ₂
Iron (III) acetylacetonate	Acros, 99 % / Fe(acac) ₃
Iron(II) chloride	Sigma-Aldrich, anhydrous, trace metals basis
Iron(III) chloride	Sigma-Aldrich, anhydrous, trace metals basis
Iron(III) nitrate nonahydrate	Fluka, ≥ 99 %
Methane 4.5	Westfalen AG, 99.995 vol. %
Methanol	Sigma Aldrich, anhydrous, 99.8 %
Nitrogen 5.0	Westfalen AG, 99.999 vol. %
Potassium bromide	Fluka, ≥ 99 %
Silver nitrate	Merck, ≥ 99.8 %
Sodium hydroxide	Merck, ≥ 99 %
Sodium nitrate	Merck, ≥ 99 %
Sulfuric acid	unknown, 96 %
Sulfuric acid for HPLC	Merck, ≥ 98 %, HPLC grade
Tetraethyl orthosilicate	Sigma-Aldrich, ≥ 98 %
Tetraethyl orthosilicate	Sigma-Aldrich, trace metals basis
Tetrapropylammonium bromide	Fluka, ≥ 98 %
Tetrapropylammonium hydroxide aqueous	Sigma-Aldrich, 1.0 mol/L
Tetrapropylammonium hydroxide aqueous	Alfa Aesar, 40 wt. %
Water for HPLC	Roth, HPLC gradient grade
Zeolite ZSM-5	Zeolyst, Si/Al=17, lot No: CBV 2314

2.1 Experimental setup

The selective oxidation of methane was carried out in a micro fixed-bed reactor. A flow sheet of the experimental setup is shown in [Figure 2.1](#). Two MFCs (Bronkhorst) were used to control the flow of N₂ and CH₄, respectively. Aqueous hydrogen peroxide solution was pumped into the reaction system by using a high-performance liquid chromatography pump (Knauer) and mixed with the gas phase consisting of methane and nitrogen in a T-junction type mixer with the liquid in straight line and the gas at a 90 ° angle. A transparent pipe was installed in front of the reactor to visually observe the flow regime and ensure the desired slug-flow regime. The temperature of the reaction was controlled by an oil bath and after the reactor a double casing cooler was used to cool the reaction mixture to ambient temperature. The pressure of the system was controlled by a digital pressure controller (Bronkhorst) after the double casing cooler. The gas phase and the liquid phase were separated by a separator behind the digital pressure controller where the pressure was decreased to nearly atmospheric pressure. The liquid phase was collected and sampled directly from the separator, while the gas phase was passed through a cooler to remove the potential moisture. A MilliGascounter (MGC-1 V3.4 PMMA, Ritter) was used to measure the flow rate of the gas phase after the second cooler. The gas phase could also be switched to the gas analyzers for online gas analysis. Passivated tubes (100 mm by length, 2.16mm ID x 3.18mm OD) made of seamless 316L grade stainless steel from Restek® are used as the reactor. Two standard 90° pipe bends (1/8") from Swagelok® are used for connection and a certain amount of glass wool is put into the two 90° pipe bends to hold the catalyst bed [130]. [Figure 2.2](#) and [Figure 2.3](#) show the micro reactor and the slug flow observed from the transparent tube in front of the reactor.

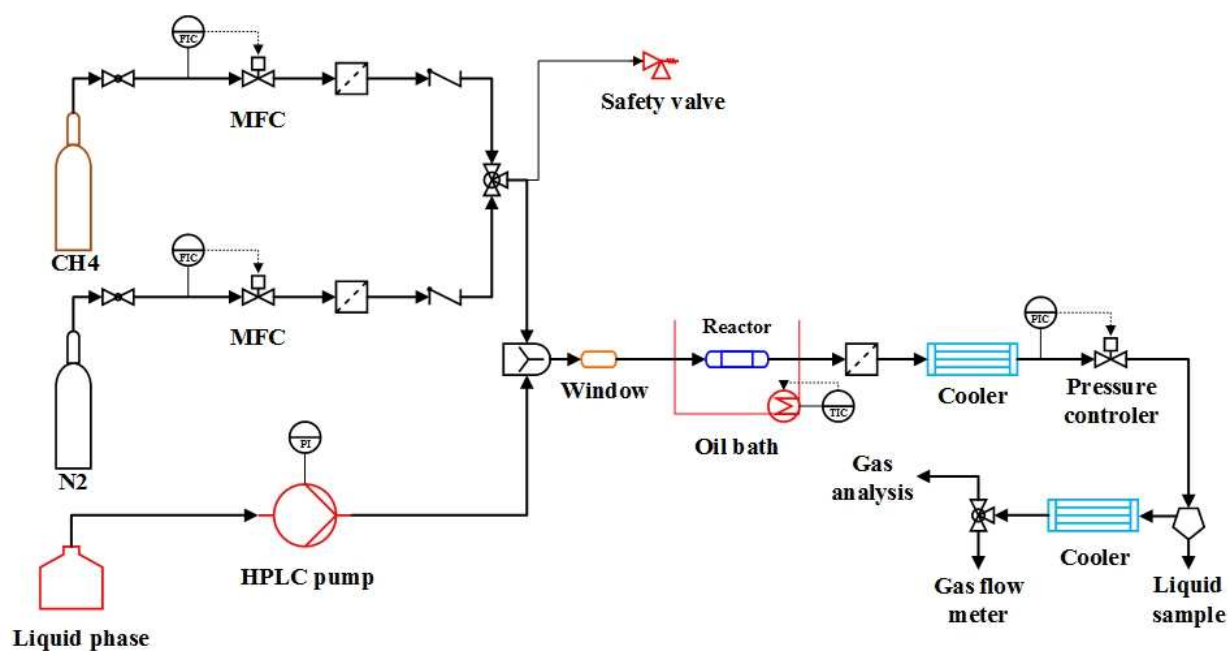


Figure 2.1. Flow sheet of the experimental setup in this work.



Figure 2.2. The micro reactor used in this work.

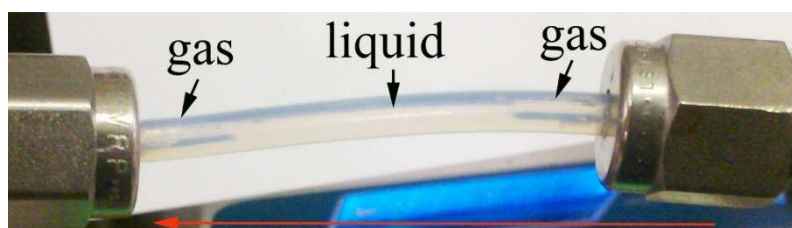


Figure 2.3. The slug flow observed from the transparent tube in front of the reactor.

2.2 Preparation of the catalysts

2.2.1 Silicalite-1, Fe-silicalite-1 and Cu-silicalite-1/Fe-silicalite-1

Silicalite-1 was synthesized according to Persson et al. [131] with modifications. This recipe was chosen because crystals of TPA-silicalite-1 with sub-micrometer size or even nano-size with a narrow size distribution could be obtained. Typically, 23.57 mL of tetraethyl orthosilicate (TEOS)

was mixed with 28.22 mL of tetrapropylammonium hydroxide (TPAOH) aqueous solution (1.0 mol/L). The molar composition of the synthesis mixture is $25\text{SiO}_2:6.82\text{TPAOH}:950\text{H}_2\text{O}$. After being stirred for 5 hours, the homogenized gel was transferred into a Teflon-lined stainless steel autoclave and crystallized at 170 °C for 3 days. The as-synthesized materials were later recovered by centrifugal separation, washed with deionized water and dried at 100 °C overnight. The dried sample was ground in a pestle and mortar to powders and calcined (8 h, 550 °C (1 °C min⁻¹)) in flowing nitrogen (5 h) and air (3 h) to obtain template free silicalite-1. Calcination was done in a shallow crucible in a muffle oven and gives at the end around 6.0 g of catalyst. The obtained sample is denoted as Si-1.

For the synthesis of Fe-silicalite-1, the same procedure was used while only before the homogenization step a certain amount of ferric citrate solution (this example shows an aimed Fe content of 0.5 wt. % in the calcined sample) was added as the precursor of Fe to form a molar composition of the synthesis mixture of $25\text{SiO}_2:6.73 \times 10^{-2}\text{Fe}_2\text{O}_3:6.82\text{TPAOH}:950\text{H}_2\text{O}$. After the same crystallization, washing, drying and grinding procedures mentioned for silicalite-1, the obtained sample is denoted as 0.5Fe-Si-1-syn. Then, 0.5Fe-Si-1-syn was calcined at 550 °C by a heating rate of 1 °C min⁻¹ and hold 5 h in flowing nitrogen and 3 h in air in a shallow crucible in a muffle oven (calcination was done in the same way described for silicalite-1) to obtain template free Fe-silicalite-1. The obtained sample is denoted as 0.5Fe-Si-1-550. The template free sample was subsequently ion-exchanged with a 1.0 M solution of $\text{NH}_4(\text{NO}_3)_3$ twice (85 °C, 24 h) and dried at 100 °C overnight. The dried sample is denoted as $\text{NH}_4\text{-}0.5\text{Fe-Si-1}$. To get H-form, $\text{NH}_4\text{-}0.5\text{Fe-Si-1}$ was calcined at 550 °C (1 °C min⁻¹) for 3 h in static air in a closed muffle oven. The finally obtained sample is denoted as H-0.5Fe-Si-1.

Sublimation was applied to get Cu-silicalite-1. The protocol for the preparation of a Cu content of 0.5 wt. % of Cu/silicalite-1 was as follows: 0.0316 g of $\text{Cu}(\text{CH}_3\text{COO})_2\text{H}_2\text{O}$ was added to 2.0 g of silicalite-1 and ground in a pestle and mortar for 30 minutes. Subsequently, the ground powder was calcined at 550 °C (1 °C min⁻¹) for 3 h in static air in a closed muffle oven.

To obtain Cu-silicalite-1/Fe-silicalite-1, the same amount of Cu-silicalite-1 and $\text{NH}_4\text{-}0.5\text{Fe-Si-1}$ was mixed, ground in a pestle and mortar for 30 minutes and calcined (550 °C, 1 °C min⁻¹) for 3 h in static air.

2.2.2 Fe-silicalite-1 with large crystals

For the synthesis of Fe-silicalite-1 with large crystals, similar recipe was used as described previously in 2.2.1, just with a diluted gel (much more water and less template were used) with a molar composition of the mixture of $25\text{SiO}_2:6.73 \times 10^{-2}\text{Fe}_2\text{O}_3:3\text{TPAOH}:1500\text{H}_2\text{O}$. The crystallization time was extended to 5 days ($170\text{ }^\circ\text{C}$). The final obtained material is denoted as H-0.5Fe-Si-1-LC.

2.2.3 Fe-silicalite-1 with small crystals

In order to obtain smaller crystal size than the materials described in 2.2.1, based on the method described in 2.2.1, a concentrated mixture (much less water and more template of TPAOH were used) with a molar composition of $25\text{SiO}_2:6.73 \times 10^{-2}\text{Fe}_2\text{O}_3:10\text{TPAOH}:100\text{H}_2\text{O}$ was used. The following procedure is the same as described in 2.2.1 and the final obtained sample is denoted as H-0.5Fe-Si-1-SC.

2.2.4 H-ZSM-5

ZSM-5 (Si/Al=29) was synthesized according to Van Grieken et al. [132]. Aluminum isopropoxide (AIP, trace metals basis, Sigma-Aldrich) and TEOS (trace metals basis, Sigma-Aldrich) were used as the aluminum and silicon source. TPAOH aqueous solution (40 wt. %, Alfa Aesar) with traces of Na was used as the template. Typically, 0.17 g of AIP was added to 4.87 g of 20 wt. % aqueous solution of TPAOH (diluted from 40 wt. % with double distilled water). The mixture was stirred at $0\text{ }^\circ\text{C}$ for 2 h. Then 5.20 g of TEOS was added to the mixture drop by drop during stirring. The molar composition of the synthesis mixture is $1\text{Al}_2\text{O}_3:60\text{SiO}_2:21.4\text{TPAOH}:650\text{H}_2\text{O}$. This mixture was stirred at room temperature for 44 h and then was heated at $80\text{ }^\circ\text{C}$ for 1.5 h to remove alcohols and reduce the water content. Finally, the concentrated solution was transferred into a Teflon-lined stainless steel autoclave and crystallized at $170\text{ }^\circ\text{C}$ for 4 days. The as-synthesized materials were later recovered by centrifugal separation, washed with double distilled water and dried at $110\text{ }^\circ\text{C}$ overnight in ambient air. To obtain template free H-ZSM-5, the dried sample was ground in a pestle and mortar to powders and transferred into a shallow crucible followed by calcination in a muffle oven (8 h, $550\text{ }^\circ\text{C}$ ($1\text{ }^\circ\text{C min}^{-1}$)) in flowing nitrogen (5 h) and air (3 h).

For comparison, commercial NH_4 -ZSM-5 zeolite obtained from Zeolyst was calcined at $550\text{ }^\circ\text{C}$ for 3 h in static air to get the H-form. This sample is denoted as H-ZSM-5-C.

2.2.5 Solid State Ion Exchange

The solid state ion exchange (SSIE) samples were prepared according to Grünert and co-workers [112]. A certain amount of FeCl_3 (trace metals basis, Sigma-Aldrich) was added to 2.0 g of H-ZSM-5 (synthesized in the section of 2.2.4) and ground in a pestle and mortar for 30 minutes. Under flowing N_2 , the mixture was firstly heated to 150 °C (2 °C/min) and then the temperature was increased to 300 °C (5 °C/min) and hold for 1 hour. After cooling down, the sample was washed and dried at 100 °C overnight. Finally, the sample was calcined (550 °C, 1 °C min⁻¹) for 3 h in flowing air. These catalysts are denoted as H/Fe(III)-ZSM-5-SSIE. For comparison, Si-1 (synthesized in the section of 2.2.1) was also used as support and denoted as Fe(III)-Si-1-SSIE. The Roman numerals in the brackets indicate the valence of iron in the original Fe precursors (not in the final catalysts, since calcination will change the oxidation state of Fe).

2.2.6 Liquid Ion Exchange

According to the method of Shishkin and co-workers [113], liquid ion exchanged (LIE) samples were prepared. 2.0 g of H-ZSM-5 (synthesized in the section of 2.2.4) was added to 100 ml FeCl_2 (trace metals basis, Sigma-Aldrich) aqueous solution (0.045 mol/L) and stirred for 48 h at room temperature. The resulting Fe-ZSM-5 sample was washed with deionized water until the rinse water was free from chlorides, which was checked by the reaction of AgNO_3 . The powder sample was then dried at 110 °C overnight at ambient air and finally calcined at 450 °C for 3 h in static air using a closed muffle oven (denoted as H/Fe(II)-ZSM-5-LIE).

LIE was also used to transfer the sample of H-0.5Fe-Si-1 from H-form to Na-form. A certain amount of the sample was mixed with a certain amount of 1.0 M solution of NaNO_3 with a mass ratio of 1:30 and then the mixture was heated to 85 °C and kept stirring for 24 h. This procedure was repeated twice and then the powder sample was dried at 100 °C overnight followed by a calcination at 550 °C (1 °C min⁻¹) for 3 h in static air in a closed muffle oven. The obtained Na-form of sample is denoted as Na-0.5Fe-Si-1-LIE.

2.2.7 Molecular Designed Dispersion method

The molecular designed dispersion (MDD) catalysts were prepared at University of Antwerp (Laboratory of Adsorption and Catalysis) by Qi Xin as follows. Prior to the synthesis, the support was dried at 200 °C for 6 h in air. Subsequently, 1 g of the thermally treated support was stirred in 30 mL anhydrous chloroform solution (CHCl_3 , $\geq 99\%$, Sigma Aldrich) containing 0.0316 g of iron

(III) acetylacetonate ($\text{Fe}(\text{acac})_3$, 99 %, Acros) or 0.023g iron (II) acetylacetonate ($\text{Fe}(\text{acac})_2$, 99 %, Chemos) in a dry air flushed glove box, to achieve a final Fe loading of 0.5 wt. %. The whole mixture was stirred for 48 h at room temperature, followed by washing and filtration with 3 times 10 mL chloroform. Afterwards, the samples were dried at 60 °C overnight in ambient air. Finally, the dried samples were calcined at 450 °C for 6 h with a heating rate of 1 °C min^{-1} in ambient air. The obtained samples are denoted as H/Fe(III)-ZSM-5-MDD, H/Fe(II)-ZSM-5-MDD and Fe(III)-Si-1-MDD.

2.2.8 Wetness Impregnation

A traditional wetness impregnation method was used to load Fe on silicalite-1. 0.38 g of Iron(III) nitrate nonahydrate was dissolved in a certain amount of deionized water, then 2.0 g of template free sample of silicalite-1 was added in the solution. After stirring for 2 hours the mixture was heated to 80 °C under stirring to remove the water. Then the obtained slurry was dried at 110 °C overnight. Finally, the sample was calcined (550 °C, 1 °C min^{-1}) for 3 h in flowing air in a muffle oven. The obtained catalyst is denoted as Fe-Si-1-WI.

2.2.9 Na-form of Fe-silicalite-1 *via* hydrothermal synthesis

To obtain the Na-form of Fe-silicalite-1 *via* hydrothermal synthesis, the source of Na was added in the gel before starting crystallization. To accomplish this, according to the procedure described in section 2.2.1, a certain amount of NaOH was added to obtain a molar composition of the synthesis mixture of $25\text{SiO}_2:6.73 \times 10^{-2}\text{Fe}_2\text{O}_3:6.82\text{TPAOH}:950\text{H}_2\text{O}:0.15\text{Na}_2\text{O}$. After crystallization, washing, drying and calcination (1 °C min^{-1} , 550 °C for 3 h), the obtained sample is denoted as Na-0.5Fe-Si-1-S.

2.2.10 Overview of the prepared samples

For the notations of the samples investigated in this work, the Arabic number before Fe indicates an aimed Fe content in the sample. For example, “0.5” indicates an aimed standard Fe content of 0.5 wt. %. The Arabic number at the end of the notation shows the calcination temperature for the removing of the organic template. For example, “550” represents that a standard calcination temperature of 550 °C was used. [Table 2.2](#) gives an overview of the prepared samples in this work.

Table 2.2. Overview of the prepared samples in this work.

Notation	Description
Si-1	The synthesized silicalite-1. See section 2.2.1.
0.5Fe-Si-1-syn	The as-synthesized Fe-silicalite-1 that still contains organic template. The Arabic number of “0.5” indicates an aimed standard Fe content of 0.5 wt. % in the calcined sample. See section 2.2.1.
0.5Fe-Si-1-550	0.5Fe-Si-1-syn after calcination. The Arabic number of “550” indicates a standard calcination temperature of 550 °C. See section 2.2.1.
NH ₄ -0.5Fe-Si-1	NH ₄ -form of calcined Fe-silicalite-1. See section 2.2.1.
H-0.5Fe-Si-1	H-form of calcined Fe-silicalite-1. See section 2.2.1.
Na-0.5Fe-Si-1-LIE	Na-form of Fe-silicalite-1 prepared by the liquid ion exchange method. See section 2.2.6.
Na-0.5Fe-Si-1-S	Na-form of Fe-silicalite-1 prepared by hydrothermal synthesis. See section 2.2.9.
Cu-silicalite-1/Fe-silicalite-1	The physical mixture of Cu-silicalite-1 and Fe-silicalite-1. See section 2.2.1.
H-0.5Fe-Si-1-LC	H-form of Fe-silicalite-1 with large crystals. See section 2.2.2.
H-0.5Fe-Si-1-SC	H-form of Fe-silicalite-1 with small crystals. See section 2.2.3.
H-ZSM-5	Self-synthesized H-form of ZSM-5 in this work. See section 2.2.4.
H-ZSM-5-C	Commercially obtained NH ₄ -ZSM-5 zeolite and after calcination to get the H-form. See section 2.2.4.
H/Fe(III)-ZSM-5-SSIE	Fe-loaded sample on H-ZSM-5 <i>via</i> the solid state ion exchange method using trivalent iron of the original Fe precursor (FeCl ₃). See section 2.2.5.
Fe(III)-Si-1-SSIE	Fe-loaded sample on silicalite-1 <i>via</i> the solid state ion exchange method using trivalent iron of the original Fe precursor (FeCl ₃). See section 2.2.5.
H/Fe(II)-ZSM-5-LIE	Fe-loaded sample on H-ZSM-5 <i>via</i> the liquid ion exchange method using divalent iron of the original Fe precursor (FeCl ₂). See section 2.2.6.
H/Fe(III)-ZSM-5-MDD	Fe-loaded sample on H-ZSM-5 <i>via</i> the molecular designed dispersion method using trivalent iron of the original Fe precursor (Fe(acac) ₃). See section 2.2.7.
H/Fe(II)-ZSM-5-MDD	Fe-loaded sample on H-ZSM-5 <i>via</i> the molecular designed dispersion method using divalent iron of the original Fe precursor (Fe(acac) ₂). See section 2.2.7.
Fe(III)-Si-1-MDD	Fe-loaded sample on silicalite-1 <i>via</i> the molecular designed dispersion method using trivalent iron of the original Fe precursor (Fe(acac) ₃). See section 2.2.7.
Fe-Si-1-WI	Fe-loaded sample on silicalite-1 <i>via</i> the wetness impregnation method. See section 2.2.8.

2.3 Characterization of the catalysts

If not mentioned the characterization method was available at the Institute of Chemical Technology. Otherwise, the institute is mentioned where the characterization method was available.

2.3.1 Powder X-Ray Diffraction

Powder X-ray diffraction (PXRD) patterns of the catalysts were obtained by using a BrukerD8 Advance diffractometer at an excitation voltage of 35 kV and a current intensity of 40 mA with a Cu K α ($\lambda = 0.154$ nm) radiation. The range of 2θ values was $5-55^\circ$ with a step size of 0.016° and a step time of 0.2 s.

2.3.2 Chemical Analysis

A Varian optical emission spectrometer Vista-MPX CCD with an inductively coupled plasma optical emission spectrometry (ICP-OES) was used to analyze the chemical composition of the catalysts and supports. Silicon, aluminum, sodium, iron and copper were determined by ICP-OES. Approximately 50 mg of the sample were dissolved in 3 mL of diluted hydrofluoric acid (10 wt. % HF in doubly distilled water) and 6 mL of nitrohydrochloric acid (aqua regia). This mixture was filled up to 250 mL with double distilled water and was then analyzed. ICP-OES analyses were carried out by Heike Fingerle.

2.3.3 Scanning Electron Microscopy

Scanning electron microscope (SEM) images were recorded using a Cambridge Cam Scan 44 instrument (in the Institute of Planetology, University of Stuttgart). The samples were covered beforehand with an ultra-thin layer of gold using an Emitech sputter coating equipment K550. SEM images were conducted by M.Sc. Swen Lang and M.Sc. Daniel Mack.

2.3.4 Transmission Electron Microscopy

Transmission electron microscopy (TEM) images were taken with an FEI TECNAI G² (in the Department of Biobased Materials, University of Stuttgart). The particles were suspended in acetone with an ultrasonic bath before they were deposited on copper grids. Remaining acetone was evaporated at ambient condition overnight. The applied voltage was 200 kV and the camera was a TVIPS TEMCAM F224HD. TEM images were conducted by M.Sc. Fabian Guba and M.Sc. Paul Rößner.

2.3.5 FT-Infrared Spectroscopy

The Fourier transform infrared spectroscopy (FT-IR) were collected with a Fischer Scientific FTIR-spectrometer Nicolet 6700. Samples were diluted with KBr (0.1 gram, the dilution ratio was 50:1) and pressed in a sample holder to pellets and measured in transmission. The resolution was 2 cm^{-1} and 64 scans were collected per sample.

2.3.6 Low Temperature Nitrogen Physisorption

Nitrogen physisorption was conducted in a Quantachrome Autosorb IIIb device to measure the textural properties of the catalysts and supports. The sample was degassed at 623 K for 16 h in high vacuum prior to the N_2 isothermal adsorption-desorption measurement at 77 K. For the calculation of the specific surface area A_{BET} according to Brunauer, Emmett and Teller (BET) [133], values of $0.1 \leq p/p_0 \leq 0.3$ were chosen to obtain a linear BET plot and a positive C-value.

2.3.7 H_2 -Temperature Programmed Reduction

H_2 -temperature programmed reduction (TPR) measurements were performed using an Autosorb iQ (Quantachrome) instrument equipped with a thermal conductivity detector (TCD). Calcined samples, with particle sizes between 200 μm and 315 μm , were loaded in a U-type quartz reactor and pre-treated in a He stream at 300 $^\circ\text{C}$ for 1 h. After cooling to 50 $^\circ\text{C}$, the reactor was heated in a flow of 10 vol. % of H_2 in N_2 (flow rate: 30 mL/min) with a heating rate of 10 $^\circ\text{C}/\text{min}$ to 1100 $^\circ\text{C}$. The flow of gas mixture was maintained at 1100 $^\circ\text{C}$ for 5 min. The H_2 consumption was calibrated by performing H_2 -TPR measurements of a known amount of CuO loaded on an inert support.

2.3.8 NH_3 -Temperature Programmed Desorption

NH_3 -temperature programmed desorption (TPD) measurements were performed on the same instrument as for H_2 -TPR measurements. A certain amount of catalyst was packed into the reactor and pretreated in a flow of N_2 (30 mL/min) at 550 $^\circ\text{C}$ for 30 min, and then, the sample was cooled to 120 $^\circ\text{C}$ for adsorbing ammonia until the saturated state was obtained. The physically adsorbed ammonia was removed by purging with helium at the same temperature for 1.5 h and the NH_3 -TPD profile was recorded by programming the temperature from 120 to 600 $^\circ\text{C}$, ramping at 10 $^\circ\text{C}/\text{min}$.

2.3.9 Diffuse reflectance Ultraviolet-Visible spectroscopy

Diffuse reflectance Ultraviolet-visible spectroscopy (UV-Vis-DR) measurements of the catalysts were carried out on a Nicolet Evolution 500 spectrophotometer equipped with an integrating

sphere. The spectra were taken in the range of 200-800 nm with a scan speed of 120 nm/min. The samples were diluted to 2 wt. % with KBr. An average of 3 measuring cycles was taken for each sample. UV-Vis-DR measurements were conducted by Karen Leyssens at University of Antwerp (Laboratory of Adsorption and Catalysis).

2.3.10 Thermogravimetric analysis

Thermogravimetric analysis (TGA) was carried out in a Setaram Thermogravimetric Analyzer Setsys TG-16/18. To figure out the minimum calcination temperature for the removal of organic template in the synthesized zeolites, the sample was heated up in a synthetic air flow from room temperature to 800 °C with a heating rate of 5 °C/min, with staying at the temperatures of 340 °C, 350 °C, 360 °C, 370 °C, 380 °C, 400 °C, 450 °C, 500 °C, and 800 °C for 5 hours. TGA was carried out by Barbara Gehring.

2.4 Procedure of the catalytic experiments

The catalyst powders were pressed and sieved to yield particles of 200-315 µm in diameter. In a typical reaction, 0.2 g or 0.1 g of catalyst was homogeneously mixed (by physical repeated mixing in a small sampling bottle) with a certain amount of inert quartz glass (200-315 µm in diameter) and loaded into the tubular reactor. After connecting the reactor, a leak check (pressure loss below 0.5 bar after 2 h) was performed using highly purified N₂ (99.999 %) at 40 bar. Then, a feed flow of 4.0 ml/min of highly purified CH₄ (99.995 %) and 4.0 ml/min of highly purified N₂ (99.999 %) was adjusted by two MFCs. Aqueous H₂O₂ solution with a certain concentration was dosed at a certain flow rate by a high-performance liquid chromatography pump. When the temperature of the oil bath reached the desired temperature, the tubular reactor was immersed into the oil bath and the reaction was started. Liquid samples were manually taken every 30 minutes from the bottom of the separator and the data of the gas analyzers was manually recorded every 15 minutes. The flow rate of the gas phase after the reactor was measured by a MilliGascounter. The reaction was conducted for 5 h as soon as the gas analyzer showed constant gas concentrations. To stop the reaction the reactor was removed from the oil bath. H₂O₂ was quantified through titration against acidified Ce(SO₄)₂ solution of known concentration, with a Ferroin indicator:



2.5 Analysis of products

The liquid sample was qualitatively analyzed by a mass spectrometer and quantitatively analyzed by high-performance liquid chromatography (HPLC, Agilent 1260) with a column of the type NUCLEOGEL SUGAR 810 H (Macherey-Nagel). The gas phase was quantitatively analyzed online by a non-dispersive infrared analyzer (Uras 10E, Hartmann & Braun) for the analysis of CH₄, CO and CO₂, and a continuous gas analyzer (EL3020, ABB) with a paramagnetic oxygen sensor for the analysis of O₂.

The following reactions are stoichiometrically possible chemical reactions for the selective oxidation of methane in aqueous H₂O₂ solution and are not the kinetically relevant chemical reactions (see section 3.3.4):



Conversion of methane (X_{CH_4}) and H₂O₂ ($X_{H_2O_2}$) were defined in [Equation \(2.8\)](#) and [Equation \(2.9\)](#):

$$X_{CH_4} (\%) = \frac{n_{o,CH_4} - n_{CH_4}}{n_{o,CH_4}} \times 100 \quad (2.8)$$

$$X_{H_2O_2} (\%) = \frac{c_{o,H_2O_2} - c_{H_2O_2}}{c_{o,H_2O_2}} \times 100 \quad (2.9)$$

Here, n_{o,CH_4} refers to the initial molar amount of methane in the sample volume at the inlet of reactor, and n_{CH_4} is the molar amount methane in the sample volume behind the reactor. Similarly, c_{o,H_2O_2} refers to the initial molar concentration of H₂O₂ in the liquid flow which is known from the specification of the used aqueous hydrogen peroxide solution at the inlet of reactor, and $c_{H_2O_2}$ is the concentration of H₂O₂ in the liquid flow behind the reactor, with the assumption that the liquid flow rate was unchanged after reaction.

The selectivities of product i based on converted methane and H_2O_2 are defined in [Equation \(2.10\)](#) and [Equation \(2.11\)](#):

$$S_{i,CH_4} (mol\%) = \frac{n_i - n_{0,i}}{n_{0,CH_4} - n_{CH_4}} \times \left| \frac{\mu_i}{\nu_{CH_4}} \right| \times 100 \quad (2.10)$$

$$S_{i,H_2O_2} (mol\%) = \frac{n_i - n_{0,i}}{n_{0,H_2O_2} - n_{H_2O_2}} \times \left| \frac{\mu_i}{\nu_{H_2O_2}} \right| \times 100 \quad (2.11)$$

Here, $n_{0,i}$ refers to the initial molar amount of product i at the inlet of reactor which was assumed to be 0, and n_i is the molar amount of product i in the sample volume behind the reactor. μ_i , ν_{CH_4} , and $\nu_{H_2O_2}$ represent the stoichiometric coefficients of product i , methane and H_2O_2 in the corresponding reaction equations (see [Equations \(2.2\) - \(2.7\)](#)), respectively. Turnover frequency (TOF) was defined as moles of liquid phase products per mole of iron and hour (h^{-1}) and volumetric productivity was defined as moles of liquid phase products per fixed-bed reactor volume and second ($mol \cdot ml^{-1} \cdot s^{-1}$).

3 Optimizing catalyst performance

3.1 Introduction

As described in section 1.3.3, Hutchings and co-workers recently carried out the selective oxidation of methane using H₂O₂ as oxidant at 70 °C under 3 bar in an autoclave reactor [63]. With a physical mixture of Cu-silicalite-1 and Fe-silicalite-1 as the catalyst, denoted in the following as Cu-silicalite-1/Fe-silicalite-1, a methane conversion of 10.1 % with a methanol selectivity of 93 % was obtained. A high turnover frequency of 70 h⁻¹ (based on Fe) with a volumetric productivity of 4.7×10⁻⁹ mol•ml⁻¹s⁻¹ towards methanol was obtained. Later on, they transferred the reaction into a fixed-bed reactor [64]. However, it was found that with the same catalyst, the TOFs dropped by nearly two orders of magnitude compared to the batch reactor and a low methane conversion of 0.5 % at optimized reaction conditions was obtained [64]. This considerable drop of the catalyst performance observed in the fixed-bed reactor let the authors assume that severe mass transport limitations occur during the reaction [64].

In this chapter, taking these results of Hutchings and co-workers as the starting point, the selective oxidation of methane with aqueous hydrogen peroxide was investigated in a continuous flow setup, but with the goal to overcome mass transport limitations. In order to decrease the barrier of mass transport, sub-micrometer sized Cu-silicalite-1/Fe-silicalite-1 was prepared to decrease internal mass transport limitations and a micro reactor was used to enhance external mass transport and guarantee a defined flow regime. The reaction conditions such as temperature, concentration of H₂O₂ in the aqueous solution and flow rate of the liquid phase were systematically varied and the best set of parameters was identified.

3.2 Catalysts and characterization

The synthesis of sub-micrometer sized silicalite-1 and Cu-silicalite-1/Fe-silicalite-1 has been already described in section 2.2.1.

The chemical compositions and textural properties of the different catalysts are shown in [Table 3.1](#). For the synthesized silicalite-1 in the present work, the contents of Fe and Cu were below the detection limit (10 ppm). For Cu-silicalite-1/Fe-silicalite-1, a Fe content of 0.24 wt. % and a Cu content of 0.26 wt. % was obtained. The first line contains the textural properties of silicalite-1 published by van Bokhoven and co-workers [134]. They synthesized silicalite-1 according to a conventional synthesis protocol leading to micrometer-sized crystals having crystal dimensions of

around $18 \times 6 \times 1 \text{ } \mu\text{m}^3$. The total apparent surface area was $355 \text{ m}^2/\text{g}$ with a small apparent external surface area of $0.5 \text{ m}^2/\text{g}$ due to the large crystal size. The sub-micrometer sized silicalite-1 and Cu-silicalite-1/Fe-silicalite-1 prepared in the present work exhibit larger apparent surface areas with values of $451 \text{ m}^2/\text{g}$ and $464 \text{ m}^2/\text{g}$, respectively. Especially for the apparent external surface area, the value significantly increased to $69 \text{ m}^2/\text{g}$ and $184 \text{ m}^2/\text{g}$, respectively, indicating much smaller crystals obtained in this work. The pore volume of the synthesized silicalite-1 was very close to that of the reference silicalite-1 while the value for Cu-silicalite-1/Fe-silicalite-1 was $0.11 \text{ cm}^3/\text{g}$, which was a little lower than that of the reference silicalite-1.

Table 3.1. The chemical compositions and textural properties of different catalysts

Catalyst	Fe (wt. %)	Cu (wt. %)	$S_{\text{BET}}^{\text{a}}$ (m^2/g)	S_{ex}^{b} (m^2/g)	V_{P}^{c} (cm^3/g)
silicalite-1*	-	-	355	0.5	0.15
silicalite-1	< 10 ppm	< 10 ppm	451	69	0.17
Cu-silicalite-1/Fe-silicalite-1	0.24	0.26	464	184	0.11

*data from reference [134]; ^a apparent surface area, calculated by BET method. ^b apparent external surface area, calculated by t-plot method. ^c micropore volume, calculated by t-plot method.

Figure 3.1 illustrates the XRD patterns of our catalysts. Characteristic reflexes of the MFI structure can be seen in all diffractograms, indicating that the catalysts were successfully synthesized and the MFI structure remains unchanged despite modification with Fe and Cu. In the diffractogram of Cu-silicalite-1/Fe-silicalite-1, no characteristic diffraction peaks belonging to Fe and Cu oxides could be observed, indicating a high dispersion of Fe and Cu species.

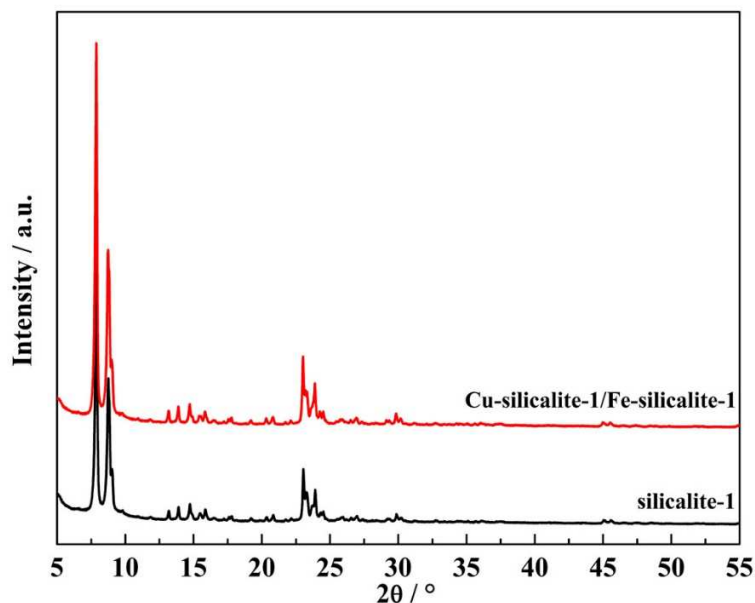


Figure 3.1. XRD patterns of the catalysts

Figure 3.2 shows the SEM images of our catalysts. As can be seen, sub-micrometer sized particles were obtained. The small particles are multicrystalline spheres with a relative uniform size distribution of 160-240 nm. The morphology is similar to that reported by Persson et al. [131]. These small crystal particles lead to a large external surface area, which was also confirmed by the low temperature N₂ adsorption-desorption measurement.

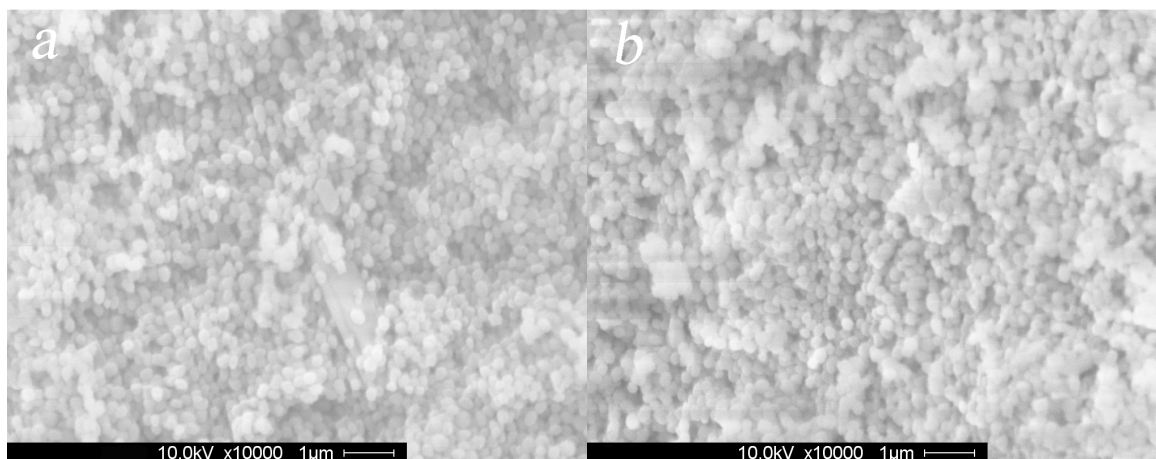


Figure 3.2. SEM images of the catalysts. a) silicalite-1, b) Cu-silicalite-1/Fe-silicalite-1.

3.3 Adjusting appropriate reaction conditions

Firstly, the reaction temperature was varied. Then at the chosen temperature, the level of over-oxidation was decreased by adjusting the concentration and flow rate of the aqueous H₂O₂ solution.

The description of the experimental setup and the procedure of the catalytic experiments can be found in the sections 2.1 and 2.4, respectively. The analysis of products is described in section 2.5. The result of blind test (reaction conditions: 0.2 g quartz glass; reaction temperature: 100 °C; pressure: 40 bar; liquid flow: 0.5 ml/min of 1.0 M aqueous H₂O₂ solution; gas flow: 4 ml/min N₂ and 4 ml/min CH₄.) showed that no conversion of methane could be observed whereas just the decomposition of H₂O₂ took place with a H₂O₂ conversion of 15.8 %.

In all catalytic measurements, the composition of gaseous products was mainly CO₂, O₂ and CO and that of the liquid products was formic acid (FA) and formaldehyde (FD) and in some cases methanol with trace amounts of less than 0.01 %. These low values are not given and discussed in chapter 3, because they are within the measurement error. The low methanol selectivity is consistent with the results of Hutchings and co-workers [64] because they found that with a decreasing liquid-to-solid ratio the subsequent oxidation of methanol takes place. With the very low liquid-to-solid-ratio in the micro reactor it is very likely that formic acid or formaldehyde rather than methanol becomes the main product.

3.3.1 Variation of the reaction temperature

Catalytic results related to CH₄ and related to H₂O₂ are shown in [Table 3.2](#) and [Table 3.3](#), respectively, for different reaction temperatures. Summing up the selectivities related to CH₄ of all the products gives values very close to 100 %, reflecting satisfying carbon balances for these experiments. Regarding to the sum of the selectivities related to H₂O₂ for all the products, the deviations are larger but within an acceptable range. These larger deviations may be caused through the errors in measuring the O₂ concentration at the outlet of the reactor. It was found that the conversion of methane increased from 15.7 % to 17.8 % and 21.0 % when the reaction temperature dropped from 140 °C to 120 °C and 100 °C. The TOFs and volumetric productivities increased from 131 h⁻¹ and 8.5×10⁻⁷ mol•ml⁻¹s⁻¹ to 169 h⁻¹ and 1.1×10⁻⁶ mol•ml⁻¹s⁻¹ when reaction temperature decreased from 140 °C to 100 °C. The reason for that seems to be the increased decomposition of H₂O₂ at higher temperatures, which reduces methane conversion and finally productivity due to lower H₂O₂ concentrations in the reactor. This can be confirmed by the observation that all H₂O₂ was converted at reaction temperatures above 100 °C. Furthermore, the selectivities to O₂ were quite high, with values above 65 %, underpinning a high level of decomposition of H₂O₂ to O₂. When further decreasing the reaction temperature from 100 °C to

70 °C, a relative high formic acid selectivity of 76.2 % was reached, mainly due to the decreased CO₂ formation with a selectivity of 25.8 %. The conversion of H₂O₂ dropped obviously from 100 % to 54.7 % and the selectivity of hydrocarbon oxygenates (formic acid) increased from 20.6 % to 33.7 % with the CO_x selectivity dropping from 21.3 % to 17.3 % (Table 3.3). However, the conversion of methane dropped significantly to 15.9 % and the TOF and volumetric productivity decreased to 142 h⁻¹ and 9.3×10⁻⁷ mol•ml⁻¹s⁻¹, respectively. When the reaction was conducted at 50 °C, no product could be detected, indicating that the selective oxidation stagnated. However, decomposition of H₂O₂ still took place with a H₂O₂ conversion of 20.6 %. Based on these results, we have chosen 100 °C as the best temperature for the selective oxidation of methane under given conditions (highlighted by italics in Table 3.2 and Table 3.3).

Table 3.2. Catalytic results related to CH₄ under different reaction temperatures.

Temperature °C	CH ₄ conversion %	Selectivity %				TOF h ⁻¹	Volume Prod mol•ml ⁻¹ s ⁻¹
		FA	CO ₂	CO	Sum		
140	15.7	54.1	50.3	0.8	105.1	131	8.5×10 ⁻⁷
120	17.8	48.0	50.7	0.5	99.3	115	7.5×10 ⁻⁷
<i>100</i>	<i>21.0</i>	<i>56.9</i>	<i>44.4</i>	<i>0</i>	<i>101.3</i>	<i>169</i>	<i>1.1×10⁻⁶</i>
70	15.9	76.2	25.8	0	102.0	142	9.3×10 ⁻⁷
50	0.5	0	0	0	0	0	0

Reaction conditions: 0.2 g Cu-silicalite-1/Fe-silicalite-1; pressure: 40 bar; liquid flow: 0.5 ml/min of 1.0 M aqueous H₂O₂ solution; gas flow: 4 ml/min N₂ and 4 ml/min CH₄.

Table 3.3. Catalytic results related to H₂O₂ under different reaction temperatures.

Temperature °C	H ₂ O ₂ conversion %	Selectivity %			
		O ₂	Hydrocarbon oxygenates	CO _x	Sum
140	100	71.8	15.7	21.0	108.5
120	100	74.8	14.1	21.9	110.8
<i>100</i>	<i>100</i>	<i>67.3</i>	<i>20.6</i>	<i>21.3</i>	<i>109.3</i>
70	54.7	60.6	33.7	17.3	111.6
50	20.6	98.3	0	0	98.3

Reaction conditions: 0.2 g Cu-silicalite-1/Fe-silicalite-1; pressure: 40 bar; liquid flow: 0.5 ml/min of 1.0 M aqueous H₂O₂ solution; gas flow: 4 ml/min N₂ and 4 ml/min CH₄.

With Cu-silicalite-1/Fe-silicalite-1 (Fe content of 0.5 wt. %) as the catalyst, Hutchings and co-workers [63] obtained a TOF of 70 h^{-1} and a volumetric productivity of $4.7 \times 10^{-9} \text{ mol} \cdot \text{ml}^{-1} \cdot \text{s}^{-1}$ in an autoclave reactor at a low temperature ($70 \text{ }^\circ\text{C}$) and pressure (3 bar). When the reaction was transferred into a flow reactor, a severe drop of the TOFs by two orders of magnitude was observed by the authors. As can be seen from Table 3.2, such a drop of the TOFs could not be found when using sub-micrometer sized Cu-silicalite-1/Fe-silicalite-1 and a micro reactor, confirming the assumption of Hutchings and co-workers [64] that mass transport limitations occur in their fixed-bed reactor. Furthermore, in this work the TOFs were in the same order of magnitude than reported by Hutchings in the batch system [63]. However, the volumetric productivities are several orders of magnitudes higher compared to their results, mainly due to the small volume of the micro reactor.

3.3.2 Decreasing the over-oxidation level

At the chosen reaction temperature of $100 \text{ }^\circ\text{C}$, the selectivity of CO_2 was still quite high with a value of 44.4 %, indicating a high level of over-oxidation. Thus, the concentration of the aqueous H_2O_2 solution and its flow rate were systematically varied at the chosen temperature of $100 \text{ }^\circ\text{C}$. Unfortunately, when loading the reactor with the amount of 0.2 g catalyst and at flow rates of the liquid phase higher than 0.7 ml/min, a significant pressure drop across the reactor of 15 bar was observed, which did not allow a constant pressure of 40 bar in the reactor. To reduce the pressure drop below 3 bar, the catalyst loading was reduced to 0.1 g and the catalyst mixed with 0.1 g of inert quartz glass with the same size distribution. The corresponding catalytic results are summarized in Table 3.4 and Table 3.5.

Table 3.4 shows the catalytic results related to CH_4 for different reaction conditions at $100 \text{ }^\circ\text{C}$. As can be found in the table, CO_2 was the only product in the gas phase and no CO could be detected. A methane conversion of 10.6 % with a FA selectivity of 64.1 % was obtained when a low flow rate of 0.2 ml/min of 1.0 M H_2O_2 was used. Formaldehyde was also found with a selectivity of 2.8 %. When the flow rate was increased from 0.2 ml/min to 0.7 ml/min, the conversion of methane increased significantly to 21.5 %, but the selectivity of FA dropped to 49.5 % and the CO_2 selectivity increased to 55.1 %. Despite the low selectivity of FA, the volumetric productivity of FA increased to $2.2 \times 10^{-6} \text{ mol} \cdot \text{ml}^{-1} \cdot \text{s}^{-1}$ due to overcompensation by the increase of the TOF to 333 h^{-1} . When further increasing the liquid flow rate to 1.5 ml/min, the methane conversion nearly doubles (40.9 %), showing strong dependence on the mean H_2O_2 concentration in the reactor.

However, the selectivity of formic acid decreased to 37.1 % and CO₂ became the main product with a selectivity of about 65 %. This observation indicates that a too high mean H₂O₂ concentration and thus H₂O₂ outlet concentration causes a poor selectivity of formic acid due to consecutive oxidation. Thus, decreasing the H₂O₂ concentration at the highest flow rate should allow to obtain a higher selectivity of FA. Indeed, when the concentration of H₂O₂ decreased to 0.5 M, a nearly two times higher selectivity (73.3 %) of FA was obtained and the selectivity of CO₂ decreased more than two times to 29.9 %. In addition, the TOF and volumetric productivity significantly increased to 590 h⁻¹ and 3.8×10⁻⁶ mol•ml⁻¹s⁻¹, respectively. In order to further increasing the selectivity of FA and decreasing the over-oxidation level of methane, an even lower concentration of 0.12 M of aqueous H₂O₂ solution was chosen. As shown in [Table 3.4](#), a methane conversion of 10.3 % with a markedly increased selectivity of 97.6 % to formic acid was obtained, with still high but not the highest values of TOF and volumetric productivity of 307 h⁻¹ and 2.0×10⁻⁶ mol•ml⁻¹s⁻¹. When further decreasing the concentration of the aqueous H₂O₂ solution to 0.06 M, the conversion of methane dropped to zero and no product at all could be detected.

Catalytic results related to H₂O₂ for different reaction conditions at 100 °C are summarized in [Table 3.5](#). The conversion of H₂O₂ dropped a little bit from 100 % to 98.3 % when the flow rate increased to 0.7 ml/min. The selectivity of O₂ significantly increased from 44.4 % to 74.9 % and the selectivity of hydrocarbon oxygenates and CO_x decreased to 12.0 % and 17.9 %, respectively. When further increasing the flow rate to 1.5 ml/min, the conversion of H₂O₂ decreased to 83.8 %, with the selectivity of hydrocarbon oxygenates dropping to only 8.0 %. The selectivities of O₂ and CO_x increased to 83.7 % and 18.6 %, respectively, indicating that both the level of H₂O₂ decomposition as well as the level of over-oxidation of methane increased under this reaction condition. Decreasing the concentration of H₂O₂ to 0.5 M lead to a drop of the H₂O₂ conversion to 71.3 % and the selectivities of O₂ and CO_x also decreased to 61.8 % and 16.0 %, respectively. The selectivity of hydrocarbon oxygenates significantly increased to 29.4 %. When the concentration of H₂O₂ was further decreased to 0.12 M, a significant decrease of H₂O₂ conversion to 48.4 % occurred with the selectivities of O₂ and CO_x also dramatically decreasing to 37.9 % and 3.2 %, respectively. The selectivity of hydrocarbon oxygenates sharply increased from 29.4 % to 70.4 %, indicating a much higher level of H₂O₂ utilization.

Table 3.4. Catalytic results related to CH₄ for different reaction conditions under 100 °C.

Liquid flow	CH ₄ conversion %	Selectivity %					TOF h ⁻¹	Volume Prod mol•ml ⁻¹ s ⁻¹
		FA	FD	CO ₂	CO	Sum		
1.0M H ₂ O ₂ , 0.2 ml/min	10.6	64.1	2.8	39.0	0	103.0	242	1.6×10 ⁻⁶
1.0 M H ₂ O ₂ , 0.7 ml/min	21.5	49.5	0	55.1	0	104.5	333	2.2×10 ⁻⁶
1.0 M H ₂ O ₂ , 1.5 ml/min	40.9	37.1	0	65.1	0	102.2	383	2.5×10 ⁻⁶
0.5 M H ₂ O ₂ , 1.5 ml/min	31.5	73.3	0	29.9	0	103.1	590	3.8×10 ⁻⁶
<i>0.12 M H₂O₂, 1.5 ml/min</i>	<i>10.3</i>	<i>97.6</i>	<i>0</i>	<i>3.3</i>	<i>0</i>	<i>101.0</i>	<i>307</i>	<i>2.0×10⁻⁶</i>
0.06 M H ₂ O ₂ , 1.5 ml/min	0.2	0	0	0	0	0	0	0

Reaction conditions: 0.1 g Cu-silicalite-1/Fe-silicalite-1; reaction temperature: 100 °C; pressure: 40 bar; gas flow: 4 ml/min N₂ and 4 ml/min CH₄.

Table 3.5. Catalytic results related to H₂O₂ for different reaction conditions under 100 °C.

Liquid flow	H ₂ O ₂ conversion %	Selectivity %			
		O ₂	Hydrocarbon oxygenates	CO _x	Sum
1.0M H ₂ O ₂ , 0.2 ml/min	100.0	44.4	31.6	24.9	100.9
1.0 M H ₂ O ₂ , 0.7 ml/min	98.3	74.9	12.0	17.9	104.8
1.0 M H ₂ O ₂ , 1.5 ml/min	83.8	83.7	8.0	18.6	110.3
0.5 M H ₂ O ₂ , 1.5 ml/min	71.3	61.8	29.4	16.0	107.2
<i>0.12 M H₂O₂, 1.5 ml/min</i>	<i>48.4</i>	<i>37.9</i>	<i>70.4</i>	<i>3.2</i>	<i>111.5</i>
0.06 M H ₂ O ₂ , 1.5 ml/min	8.9	114.6	0	0	114.6

Reaction conditions: 0.1 g Cu-silicalite-1/Fe-silicalite-1; reaction temperature: 100 °C; pressure: 40 bar; gas flow: 4 ml/min N₂ and 4 ml/min CH₄.

3.3.3 Comparison with the state-of-the-art

For better comparison, [Figure 3.3](#) shows the selectivities of hydrocarbon oxygenates as a function of the corresponding conversions of methane measured in the present work together with results published so far in the open literature. As can be seen in the figure, the selectivities range from 0 to nearly 97 % and the methane conversions range from 0.2 to nearly 41 %. By adjusting the concentration and the flow rate of aqueous H₂O₂ solution, both the conversion of methane and the selectivity of formic acid could be enhanced considerably leading to the best S,X-trajectory compared with literature results. Thus, a higher oxygenate selectivity was obtained at the same level of methane conversion when compared to reference [63] in which an autoclave batch reactor

was used. However, in the present work, formic acid was the main product whereas in reference [63] methanol was the main product at Cu-silicalite-1/Fe-silicalite-1 due to the much higher liquid-to-solid ratio in the batch reactor compared to the micro reactor. When the reaction was performed in a continuous reactor according to reference [64], the methane conversion sharply dropped to 0.5 %, indicating a slow overall kinetics due to mass transport limitations. In reference [64] both methanol and formic acid was formed with the Cu-Fe-ZSM-5 (with a Fe/Cu ratio similar to our catalysts), which was explained by the lower liquid-to-solid ratio compared to the batch reactor. Since the liquid-to-solid ratio of our micro reactor is even lower it could be the reason, that no or only trace amounts of methanol were found. Another possible reason may be that a special structure of the Cu species is needed to decrease the level of over-oxidation and thus leading to the formation of methanol as a main product (see also Figure 1.21). However, it was not the aim of the present work to optimize the structure of the Cu sites in order to suppress over-oxidation. Furthermore, the working hypothesis in reference [63] is doubtful since a physical mixture of Fe- and Cu-silicalite-1 is used which brings along a large distance between Fe- and Cu-sites. Ishihara and co-workers also obtained formic acid by partial oxidation of methane on H-ZSM-5 with a methane conversion of 19.5 % and a selectivity to formic acid of 66.8 % [135]. However, the reaction was carried out in an autoclave reactor and triphenylphosphine (Ph₃P) was used as a promoter. Also compared to this reference, better catalytic performance by optimization of temperature, H₂O₂ concentration and H₂O₂ flow rate could be observed in the present work.

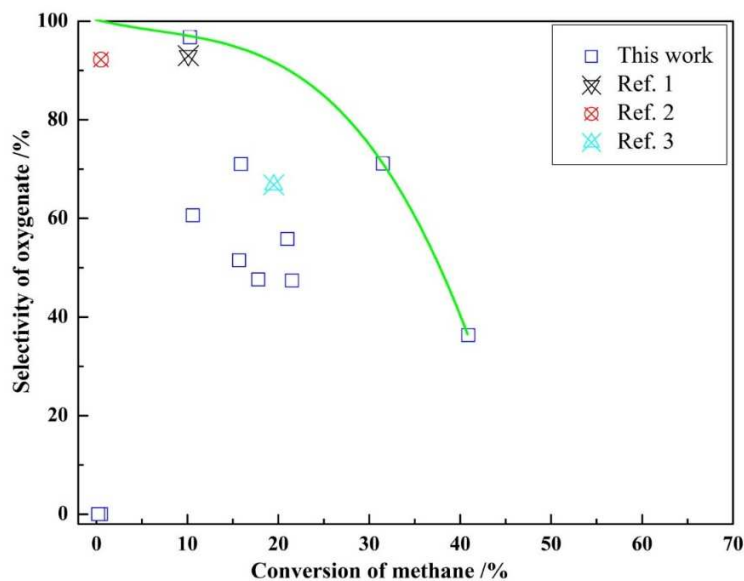


Figure 3.3. Selectivity of hydrocarbon oxygenates as a function of the methane conversion for the present work and from literature (Ref. 1: [63], Ref. 2: [64] and Ref. 3: [135]).

3.3.4 Reaction scheme

As discussed, for the selective oxidation of methane, the main gaseous products were CO_2 , O_2 and CO and the liquid products consisted of formic acid (FA), formaldehyde (FD) and in some cases trace amounts of methanol. Methyl hydroperoxide (CH_3OOH , MHP) was found to be the primary reaction product when relative low temperatures such as $50\text{ }^\circ\text{C}$ were chosen for the selective oxidation of methane using H_2O_2 as oxidant [63]. However, when the reaction temperatures increased above $70\text{ }^\circ\text{C}$, no MHP could be detected anymore [64]. This may be due to the fact that MHP is not stable at such high temperatures under given conditions. In the present work, the reaction temperature was $100\text{ }^\circ\text{C}$ and as expected, no MHP could be detected.

Although a high level of catalytic performance could be obtained under the optimal reaction conditions in the present work, the reaction scheme is still not clear under given conditions. Thus, in this section the reaction scheme was investigated. Firstly, the possibility of the conversion of methanol, FD and FA over the catalyst without H_2O_2 under the optimal reaction conditions was checked. For this purpose, 0.05 M of methanol, FD and FA aqueous solution were separately dosed into the reaction system without H_2O_2 as the oxidant using pure N_2 (8 ml/min) as the gas phase flow. These results showed that no conversion of these hydrocarbon oxygenates happened and no gaseous products such CO_2 and CO could be detected, indicating that without the presence of H_2O_2 the conversion of these hydrocarbon oxygenates over the catalyst was negligible.

Then a certain amount of methanol, FD or FA was premixed with 0.12 M aqueous H₂O₂ solution to obtain a concentration of 0.05 M of the corresponding hydrocarbon oxygenate aqueous solution. These obtained liquid mixtures were dosed into the reaction system under the optimal reaction conditions using pure N₂ (8 ml/min) as the gas phase. The catalytic results are summarized in Table 3.6. For all these experiments, CO₂ was the only gaseous product and no CO was detected. When methanol and H₂O₂ aqueous mixture was used as the reactant, the conversion of methanol was 34.6 %. Liquid products of FD and FA were detected with selectivities of 21.3 % and 79.5 %, respectively. The selectivity of CO₂ was 4.2 %. When the mixture of FD and aqueous H₂O₂ solution was dosed into the reaction system, a FD conversion of 60.2 % was reached. The selectivities to FA and CO₂ were 87.7 % and 18.5 %, respectively. In the case of FA, the conversion of FA was 27.9 % and CO₂ was the only detected product.

Table 3.6. Catalytic results of using different hydrocarbon oxygenates as reactants.

Reactant	hydrocarbon oxygenates conversion %	Selectivity %				
		FD	FA	CO ₂	CO	Sum
CH ₃ OH + H ₂ O ₂	34.6	21.3	79.5	4.2	0	105.0
HCHO + H ₂ O ₂	60.2	-	87.7	18.5	0	106.2
HCOOH + H ₂ O ₂	27.9	-	-	98.7	0	98.7

Reaction conditions: 0.1 g Cu-silicalite-1/Fe-silicalite-1; reaction temperature: 100 °C; pressure: 40 bar; gas flow: 8 ml/min N₂; liquid flow: 1.5 ml/min of 0.05 M of hydrocarbon oxygenates in 0.12 M aqueous H₂O₂ solution.

Taking all these results into account, a reaction scheme could be derived which is depicted in Figure 3.4. Without the presence of H₂O₂, the conversion of hydrocarbon oxygenates such as methanol, FD and FA over the catalyst was negligible under given conditions, especially meaning that formic acid decomposition does not take place. While at the presence of H₂O₂, the reaction scheme for the selective oxidation of methane comprises consecutive oxidation reaction steps with methanol, formaldehyde and formic acid as the intermediate products and CO_x as the final product.

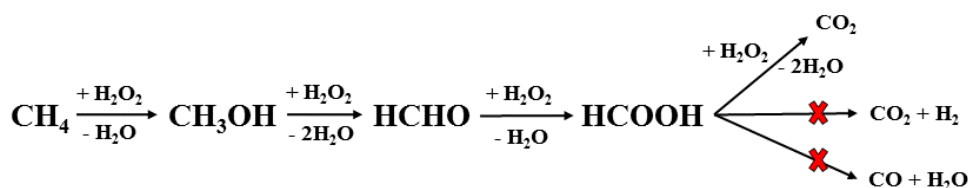


Figure 3.4. Proposed reaction scheme for the selective oxidation of methane under given conditions.

3.4 Summary

Sub-micrometer sized Cu-silicalite-1/Fe-silicalite-1 was prepared and the selective oxidation of methane with aqueous H_2O_2 was conducted in a micro fixed-bed reactor to intensify internal and external mass transport of the overall reaction. The reaction conditions were optimized by varying the reaction temperature and both the concentration as well as the flow rate of the aqueous H_2O_2 solution. Formic acid rather than methanol was the main product in the liquid phase. Thus, the positive role of Cu species for obtaining methanol as the main product and preventing its over-oxidation as stated in literature (see section 1.3.3 and [Figure 1.21](#)) could be not confirmed. However, the TOFs of methane selective oxidation could be enhanced nearly three orders of magnitude compared to previously reported work in a fixed-bed reactor [64]. As reaction temperature of 100 °C was chosen and a relative low concentration of aqueous H_2O_2 solution (0.12 M) at a relative high flow rate (1.5 ml/min) was adjusted to decrease over-oxidation of methane. A selectivity to formic acid of 96.7 % at a methane conversion of 10.3 % could be achieved under these optimal reaction conditions. The optimal reaction conditions and the corresponding results are highlighted in italics in the [Tables 3.2, 3.3, 3.4, and 3.5](#). The investigation of the reaction scheme revealed that the selective oxidation of methane comprises consecutive oxidation reaction steps over the catalyst. No decomposition of formic acid took place in the absence of H_2O_2 , whereas in the presence of H_2O_2 total oxidation of formic acid was observed. However, formic acid was not completely oxidized to CO_2 but to about 30 %, which seems to be consistent with the results of methane partial oxidation in which a similar amount of formic acid is formed when passing the reactor.

4 Selective oxidation of methane over Fe-silicalite-1 catalysts

As described in sections of 1.3.3 and 1.4.1, Fe-silicalite-1 (Fe-containing MFI zeolite prepared by the direct hydrothermal synthesis method) zeolites were intensively investigated by many researchers due to their good performance in selective oxidations, xylene isomerization, and ethylbenzene dehydrogenation reactions. Binuclear Fe species, positively charged or neutral, which are similar to those present in sMMO, could be also formed by the migration of Fe from framework to extra-framework positions during calcination of Fe-silicalite-1. These binuclear Fe species are proposed to be the active sites for the selective oxidation of methane in aqueous H₂O₂ solution [63]. It has been discussed in chapter 3 that the positive role of Cu species in the Cu-silicalite-1/Fe-silicalite-1 catalyst, which has been reported in literature (see section 1.3.3, [Figure 1.21](#)) for obtaining methanol as the main product, could not be reproduced in the present work. Therefore, in this chapter, the focus of investigation was shifted to Fe-silicalite-1. In chapter 3, it was found that the optimum reaction temperature was 100 °C and a relative low concentration of aqueous H₂O₂ solution (0.12 M) at a relative high flow rate (1.5 ml/min) was preferable for the selective oxidation of methane. Thus, these conditions were used in all following investigations described in chapters 4 and 5. The influence of different calcination temperatures, different Fe contents, different crystal sizes and different acidities of Fe-silicalite-1 to the selective oxidation of methane in a micro fixed-bed reactor was investigated.

4.1 The influence of different calcination temperatures

4.1.1 Introduction

Due to the state-of-the-art, the migration of iron species from framework to extra-framework positions can take place during the calcination procedure when removing the organic template. Thus, it can be expected that different calcination temperatures would lead to different amounts of iron species located at extra-framework positions. As the local structure of the iron species in framework and extra-framework positions is totally different, it is interesting to investigate the difference of their catalytic performance.

Starting from the as-synthesized Fe-silicalite-1 that still contains organic template, different calcination temperatures were used to remove the template. Firstly, in order to find a minimum calcination temperature that is necessary to remove most of the organic template, a TGA measurement of the as-synthesized sample was carried out (see the procedure described in section

2.3.10). Figure 4.1 shows the measured TGA profile of the template containing Fe-silicalite-1 sample. It could be found that at a calcination temperature of 370 °C in flowing air, more than 96 % of weight loss was reached compared to the total weight loss at a final temperature of 800 °C. This indicates that almost all of the organic template can be removed at a calcination temperature of 370 °C. In particular, a calcination temperature of 550 °C used as a standard calcination temperature in the present work (see section 2.2.1) is sufficient to remove totally the organic template. In this work, a series of samples calcined at different temperatures above 370 °C were prepared and these catalysts were characterized by XRD, ICP-OES, low temperature N₂ adsorption-desorption, H₂-TPR, NH₃-TPD, TEM, FT-IR and UV-Vis-DR techniques. Their catalytic activities were investigated and compared.

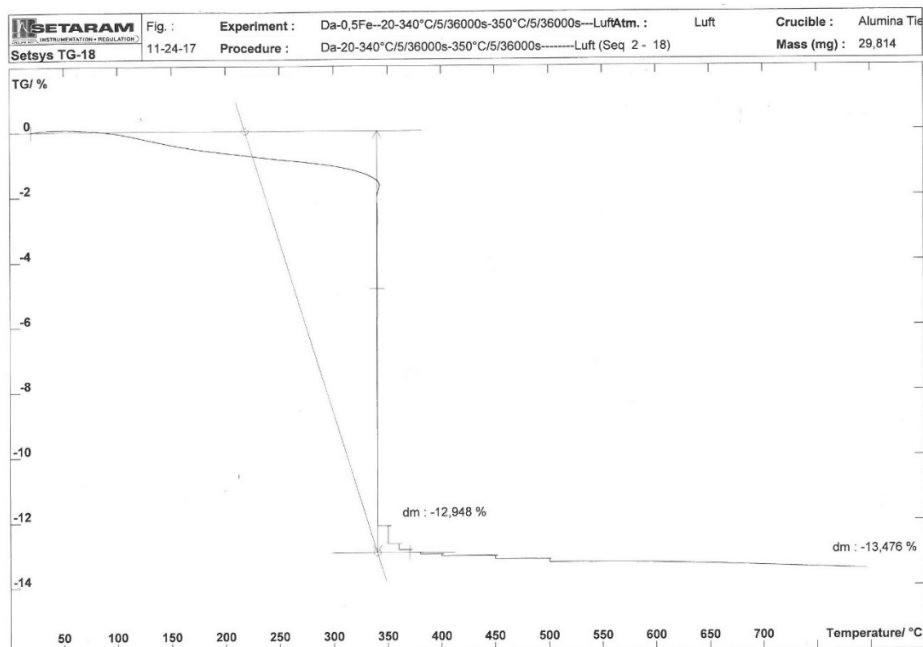


Figure 4.1. TGA profile of template containing Fe-silicalite-1 sample.

4.1.2 Catalysts

Sub-micrometer sized Fe-silicalite-1 samples were hydrothermally synthesized (see section 2.2.1). The Fe loading was set to 0.5 wt. % by addition of the corresponding amount of Fe precursor before starting the crystallization step. The obtained template containing Fe-silicalite-1 sample, so-called as-synthesized Fe-silicalite-1, is denoted as 0.5Fe-Si-1-syn. Then, calcination temperatures of 370 °C, 450 °C, 550 °C, 650 °C and 750 °C were adjusted by a heating rate of 1 °C min⁻¹ and hold 5 h in flowing nitrogen and 3 h in air. After calcination the ion exchange

procedure with a 1.0 M solution of $\text{NH}_4(\text{NO}_3)_3$ as described in section 2.2.1 was omitted. The obtained calcined catalysts are denoted as 0.5Fe-Si-1-370, 0.5Fe-Si-1-450, 0.5Fe-Si-1-550, 0.5Fe-Si-1-650 and 0.5Fe-Si-1-750 with the calcination temperature as the last figure in the notation.

4.1.3 Characterization results

Table 4.1 illustrates the chemical compositions and textural properties of Fe-silicalite-1 catalysts calcined at different temperatures. As all these catalysts were generated from the same parent sample of 0.5Fe-Si-1-syn *via* different calcination temperatures, it is not surprising that similar Fe contents of around 0.45 wt. % were obtained for all these catalysts. For 0.5Fe-Si-1-370, the highest apparent surface area of 462 m^2/g together with a micropore volume of 0.15 cm^3/g was obtained. When calcination temperatures increased from 370 °C to 750 °C, the apparent surface area dropped gradually from 462 m^2/g to 410 m^2/g . The micropore volume also decreased gradually from 0.15 cm^3/g to 0.13 cm^3/g . This trend can be explained by the increasing migration of Fe species from framework to extra-framework positions with increasing calcination temperatures, and thus blocking the channels of the Fe-silicalite-1, leading to the drop of apparent surface area and micropore volume. There is no obvious trend for the changes of the apparent external surface area.

Table 4.1. Chemical compositions and textural properties of Fe-silicalite-1 catalysts calcined at different temperatures.

Sample	Fe (wt. %)	$n_{\text{Fe}/n_{\text{Si}}}$	$S_{\text{BET}}^{\text{a}}$ (m^2/g)	S_{ex}^{b} (m^2/g)	V_{P}^{c} (cm^3/g)
0.5Fe-Si-1-370	0.45	0.0050	462	76	0.15
0.5Fe-Si-1-450	0.44	0.0049	448	103	0.15
0.5Fe-Si-1-550	0.45	0.0050	396	83	0.14
0.5Fe-Si-1-650	0.46	0.0050	419	121	0.13
0.5Fe-Si-1-750	0.45	0.0049	410	107	0.13

^a apparent surface area, calculated by BET method. ^b apparent external surface area, calculated by t-plot method. ^c micropore volume, calculated by t-plot method.

Figure 4.2 demonstrates the XRD patterns of the Fe-silicalite-1 catalysts calcined at different temperatures. Characteristic diffraction patterns of the MFI structure could be observed for all of the samples irrespective of the calcination temperature chosen. These observations indicate that the parent sample, 0.5Fe-Si-1-syn, was successfully synthesized and the MFI structure retained

despite calcination under different temperatures, even as high as 750 °C. No characteristic diffraction reflexes belonging to Fe oxides could be observed from the diffractograms of all catalysts, suggesting that the Fe oxide species were highly dispersed.

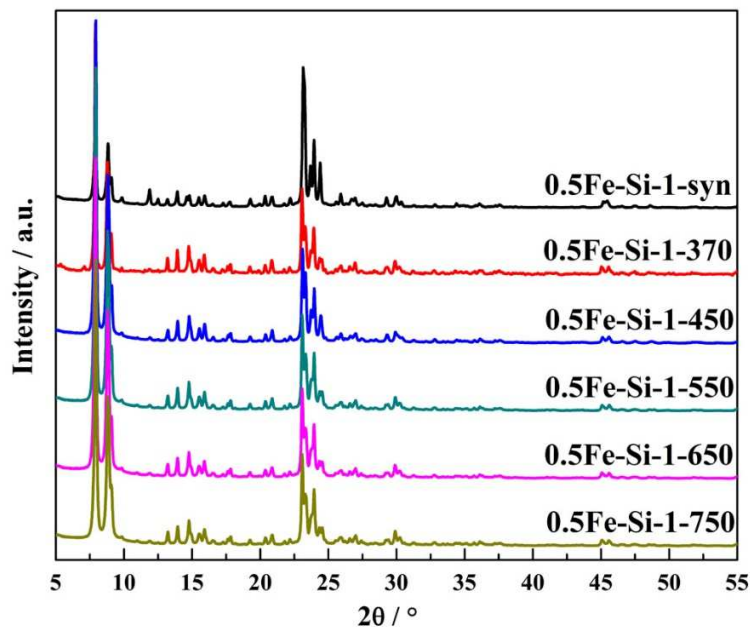


Figure 4.2. XRD patterns of Fe-silicalite-1 catalysts calcined at different temperatures.

The TEM image of 0.5Fe-Si-1-syn is displayed in [Figure 4.3](#). Sub-micrometer sized crystals of ellipsoid-like shape and sizes ranging from 200 nm to 370 nm (most particle size around 300 nm) were obtained. These crystals exhibit relative clear edges.

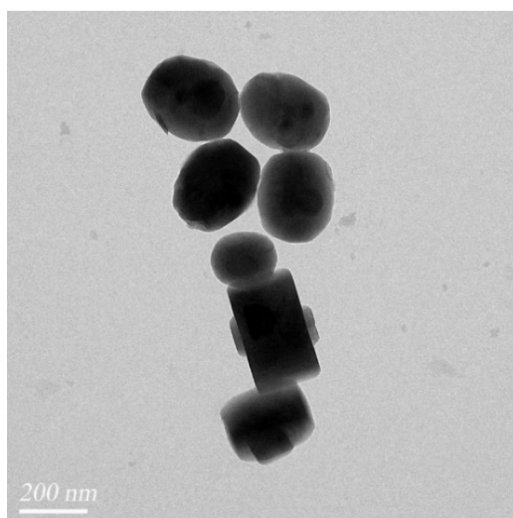


Figure 4.3. TEM image of 0.5Fe-Si-1-syn

According to Zecchina and co-workers [136], infrared spectroscopy could provide meaningful information concerning the iron structure in the zeolite by exploring both the hydroxyl stretching region (3800-3400 cm^{-1}) and the framework stretching region (1350-400 cm^{-1}). Figure 4.4 shows FT-IR spectra of the catalysts in the hydroxyl stretching region. For 0.5Fe-Si-1-syn, the broad absorption extending from 3600 to 2500 cm^{-1} can be attributed to the OH stretching band of the organic template (TPAOH) and the superimposed stretching modes at 3030-2860 cm^{-1} can be attributed to CH_2 and CH_3 groups in the template [119]. After calcination, an obvious shoulder peak appeared at 3670 cm^{-1} , which is assigned to bridged hydroxyl groups relating to Brønsted acid sites [119] coming along with Fe species in the framework of the 0.5Fe-silicalite-1. When increasing the calcination temperature this shoulder peak remains, indicating the stability of framework Fe species even at a high calcination temperature of 750 °C. This is consistent with the observations from XRD measurements. A more obvious broad absorption peak could be found with maximum at 3450 cm^{-1} , which is attributed to hydrogen-bonded silanolic species, indicating that partial extraction of Fe^{3+} from the framework leads to the formation of hydroxyl nests [119].

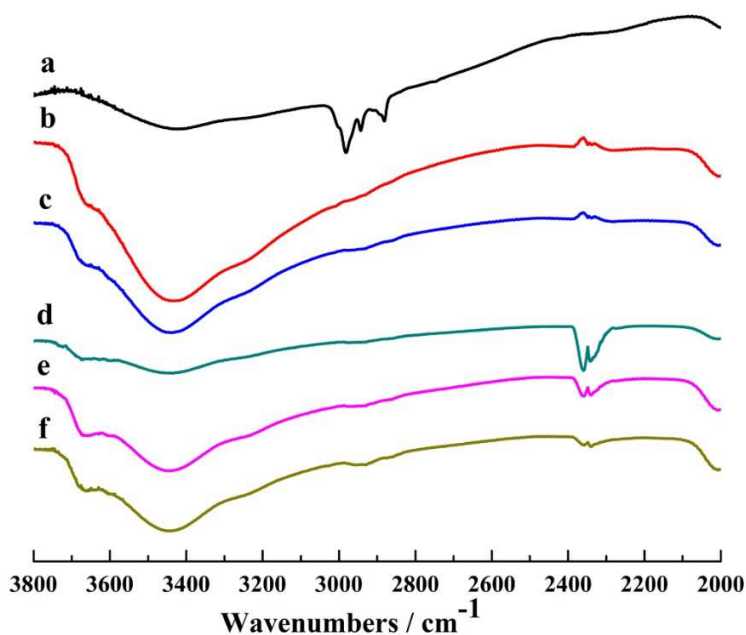


Figure 4.4. Transmission FT-IR spectra of Fe-silicalite-1 catalysts calcined at different temperatures in the OH stretching region. (a) 0.5Fe-Si-1-syn, (b) 0.5Fe-Si-1-370, (c) 0.5Fe-Si-1-450, (d) 0.5Fe-Si-1-550, (e) 0.5Fe-Si-1-650, (f) 0.5Fe-Si-1-750.

FT-IR spectra of the Fe-silicalite-1 catalysts calcined at different temperatures in the framework stretching region (1300-400 cm^{-1}) are depicted in Figure 4.5. According to Bordiga and co-workers

[119], the bands appeared at 1006 cm^{-1} are mainly associated with the vibrational modes of tetrahedral surrounding of the Fe^{3+} centers by O_3SiO^- units. It is clear that, after calcination, the intensity of this band decreased with increasing calcination temperature, revealing the drop of the concentration of framework Fe^{3+} species. For all the calcined catalysts, absorption peaks appeared at 686 cm^{-1} with a small shoulder peak observed at around 697 cm^{-1} . The band at 686 cm^{-1} is attributed to the characteristic Si-O-Fe linkage [137, 138]. The tiny shoulder peaks found around 697 cm^{-1} are very close to the characteristic band of Si-O-Fe, indicating there may exist Si-O-Fe linkages in the framework of these zeolites with different structural surroundings. Zecchina and co-workers found that after calcination the iron species dislodged from the tetrahedral lattice positions would interact with residual Si(OH)Fe bridges, defective SiOH groups, or strained SiOSi bridges of the framework, leading to the formation of grafted or anchored isolated and/or clustered Fe species [118]. Thus, it is very likely that new Si-O-Fe linkages were formed which have different local structures compared to the ones located in the framework.

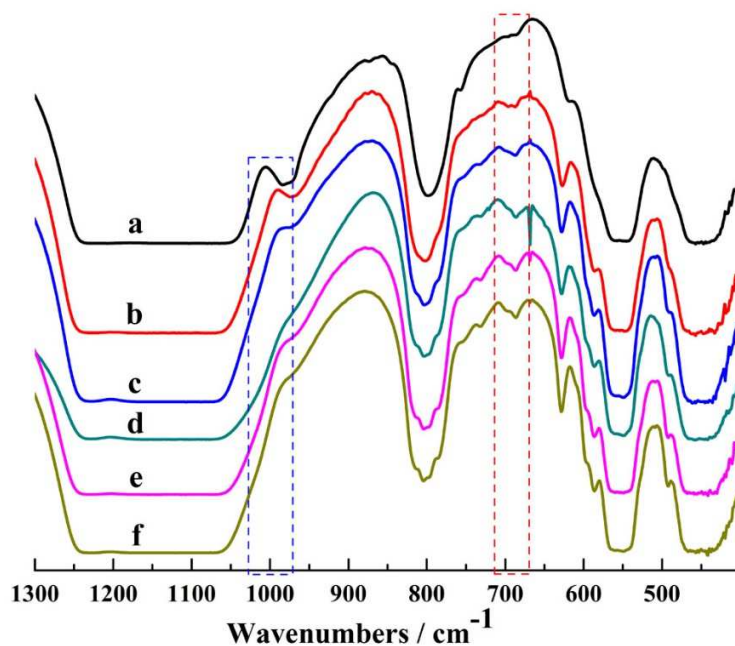


Figure 4.5. Transmission FT-IR spectra of Fe-silicalite-1 catalysts calcined at different temperatures in the framework stretching region. (a) 0.5Fe-Si-1-syn, (b) 0.5Fe-Si-1-370, (c) 0.5Fe-Si-1-450, (d) 0.5Fe-Si-1-550, (e) 0.5Fe-Si-1-650, (f) 0.5Fe-Si-1-750.

Figure 4.6 illustrates the H_2 -TPR profiles of the Fe-silicalite-1 catalysts calcined at different temperatures. For 0.5Fe-Si-1-370, an obvious reduction peak with shoulders appeared at $953\text{ }^\circ\text{C}$.

Two broad shoulder peaks could also be observed at 437 °C and 645 °C. For 0.5Fe-Si-1-450, the high temperature reduction peak dropped to 927 °C and another two broad peaks appeared at 455 °C and 670 °C. If the calcination temperature is further increased (0.5Fe-Si-1-550), the high temperature reduction peak dropped strongly to 801 °C and a more distinct shoulder peak appeared at 629 °C. Two small broad shoulder peaks could be found at 336 °C and 421 °C. For 0.5Fe-Si-1-650, the high temperature reduction peak increased slightly to 846 °C and the shoulder peak observed at 629 °C in the TPR-profile of the 0.5Fe-Si-1-550 appeared now at 619 °C and was much more significant. A very small and broad peak could be noticed at 384 °C. For 0.5Fe-Si-1-750, the high temperature reduction peak still appeared at 843 °C. It is interesting that additionally to the peak at 636 °C another new peak appeared at 523 °C. In addition, two tiny shoulder peaks could be observed at 342 °C and 408 °C.

Fe-silicalite-1 can form a very complex family of extra-framework iron species such as larger Fe-oxide aggregates, isolated bi-nuclear clusters and other charge-compensating species due to the migration of Fe from the zeolite framework during the calcination procedure [118]. Our results are consistent with the state-of-the-art, as the wide variety of reduction peaks and shoulders indicates a wide variety of Fe species existing in the catalysts. According to Meloni et al. [139], the reduction peaks appearing below 450 °C are attributed to isolated extra-framework iron species whereas peaks appearing between 500 to 680 °C are mainly due to the reduction of charge-compensating extra-framework Fe³⁺ species and reduction peaks above 680 °C are assigned to framework Fe³⁺ species. Thus, the following picture of the observed iron species in the Fe-silicalite-1 samples calcined at different temperatures may be roughly depicted as follows: (1) for the calcination temperatures of 370 °C and 450 °C, various extra-framework iron species were observed in small amounts with broad reduction peaks. With increasing calcination temperature, there is an obvious trend that the amount of extra-framework iron species is increasing, with more iron species moving towards charge-compensating positions. (2) when the calcination temperature increased from 370 °C to 750 °C, the stability of framework iron species firstly decreased with the lowest reduction temperature appeared at 801 °C for the sample calcined at 550 °C and with increasing the calcination temperature to 650 °C and 750 °C, the stability of the framework iron species was strengthened again indicated by a shift of the high-temperature reduction peak to higher temperatures. The areas of the high-temperature reduction peaks dropped with increasing calcination temperatures, revealing that more and more iron species migrated from framework to

extra-framework positions. This observation is consistent with the results of low-temperature N_2 sorption, and FT-IR. For 0.5Fe-Si-1-750, the area of the high temperature reduction peak was smaller than the areas of the lower temperature reduction peaks, revealing more extra-framework iron species than those located in the framework.

Table 4.2 summarizes the hydrogen consumption per Fe site determined from the H_2 -TPR profiles of the catalysts calcined at different temperatures. Values between 0.44 to 0.52 can be found for all the calcined catalysts and these values are very close to the expected theoretical value of 0.50 for the reduction of Fe^{3+} to Fe^{2+} . It has been reported in literature that self-reduction of partial Fe^{3+} species to Fe^{2+} species could be observed during the calcination process [118, 140]. This may explain that for some catalysts the Fe related H_2 consumption values were lower than 0.50.

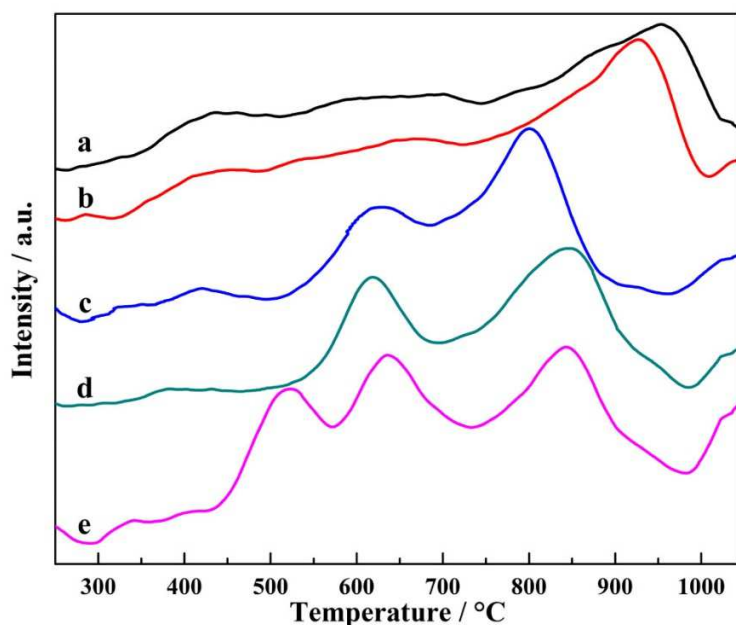


Figure 4.6. H_2 -TPR profiles of Fe-silicalite-1 catalysts calcined at different temperatures. (a) 0.5Fe-Si-1-370, (b) 0.5Fe-Si-1-450, (c) 0.5Fe-Si-1-550, (d) 0.5Fe-Si-1-650, (e) 0.5Fe-Si-1-750.

Table 4.2. Hydrogen consumption during the H₂-TPR experiments for Fe-silicalite-1 catalysts calcined at different temperatures.

Sample	H ₂ /Fe consumption (mol/mol)
0.5Fe-Si-1-370	0.46
0.5Fe-Si-1-450	0.48
0.5Fe-Si-1-550	0.45
0.5Fe-Si-1-650	0.44
0.5Fe-Si-1-750	0.52

Figure 4.7 shows the NH₃-TPD profiles of Fe-silicalite-1 catalysts calcined at different temperatures. For 0.5Fe-Si-1-370, an obvious peak appeared at 208 °C and a tiny broad shoulder peak can be recognized at around 350 °C. When the calcination temperature increased to 450 °C, the low temperature desorption peak of NH₃ slightly decreased to 204 °C with an obvious drop of the peak area. A little increase of the area for the shoulder peak at 350 °C was observed. If the calcination temperature was further increased to 750 °C, the low temperature desorption peak shifted to 190 °C together with a continuous drop of the area. The shoulder peak at 350 °C became more and more broad and indistinct. It has been reported that Fe-silicalite-1 shows an acidity being very similar to that of H-ZSM-5 because of the isomorphous substitution of a certain fraction of Si⁴⁺ with Fe³⁺, leading to the formation of Brønsted acid sites that are responsible for a relative high NH₃ desorption temperature [119, 122]. The attribution of the NH₃ desorption peak at low temperature (e.g. around 200 °C) is still under debate. It has been attributed to weak Lewis acid sites mainly generated by extra-framework metal species [141] or weak Brønsted acid sites generated from the bridged hydroxyls [142, 143]. In this work, it is most likely that the desorption peak appeared at around 200 °C can be attributed to the weak Brønsted acid sites. As with increased calcination temperature, more and more framework iron species moved out of the framework (confirmed by N₂ sorption, FT-IR and H₂-TPR), this inevitably leads to a decrease of the amount and the strength of Brønsted acid sites. This is consistent with the observation of the NH₃-TPD results. The very small or even absent high temperature NH₃ desorption peak is probably caused by the fact that a considerable amount of charge-compensating extra-framework positions were occupied by charged extra-framework iron species rather than Brønsted acidic protons.

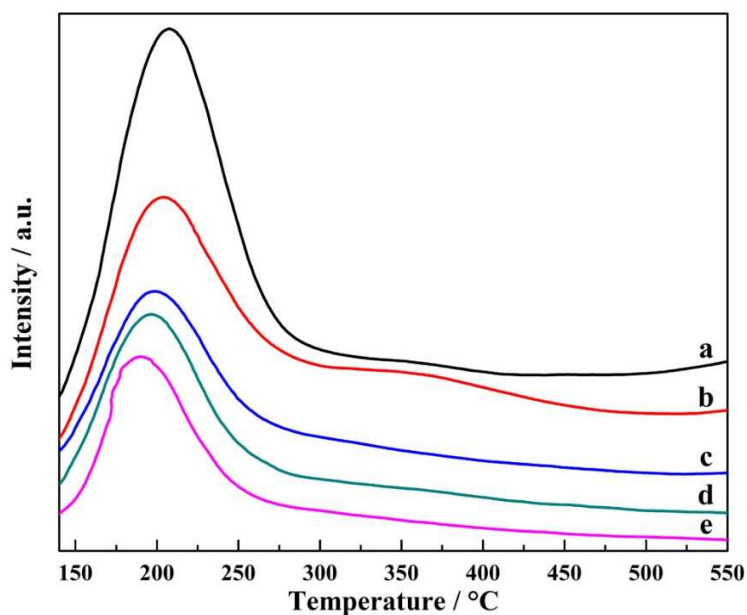


Figure 4.7. NH₃-TPD profiles of Fe-silicalite-1 catalysts calcined at different temperatures. (a) 0.5Fe-Si-1-370, (b) 0.5Fe-Si-1-450, (c) 0.5Fe-Si-1-550, (d) 0.5Fe-Si-1-650, (e) 0.5Fe-Si-1-750.

The UV-Vis-DR spectra of the Fe-silicalite-1 catalysts calcined at different temperatures are illustrated in Figure 4.8. According to Grünert and co-workers, the bands below 300 nm are attributed to Fe³⁺ ← O charge transfer bands of isolated Fe ions in tetrahedral or octahedral coordination and the band at around 350 nm due to oligomeric clusters, while sub-bands above 400 nm are assigned to larger Fe-oxide aggregates [114]. For all the samples, bands appeared below 300 nm while no bands above 300 nm could be obviously observed, indicating most of the Fe species in these samples were isolated in tetrahedral or octahedral coordination and no larger aggregates of Fe species could be detected by UV-Vis-DR. For all the calcined samples, no difference in the spectra could be obviously found, indicating that the different Fe species in these samples could not be distinguished by UV-Vis-DR spectra, but observed by FT-IR and H₂-TPR.

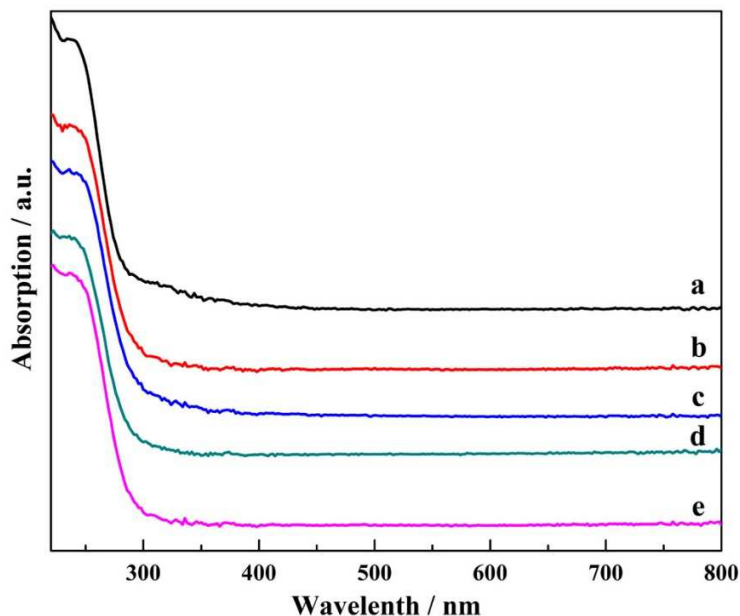


Figure 4.8. UV-Vis-DR spectra of Fe-silicalite-1 catalysts calcined at different temperatures. (a) 0.5Fe-Si-1-syn, (b) 0.5Fe-Si-1-450, (c) 0.5Fe-Si-1-550, (d) 0.5Fe-Si-1-650, (e) 0.5Fe-Si-1-750.

4.1.4 Catalytic results and discussion

Table 4.3 summarize the catalytic results related to CH₄ for the catalysts calcined at different temperatures. It is interesting that when increasing the calcination temperature, the conversion of methane firstly increased from 15.2 % (0.5Fe-Si-1-370) over 15.5 % (0.5Fe-Si-1-450) to 17.1 % (0.5Fe-Si-1-550), then obviously decreased to 13.9 % (0.5Fe-Si-1-650) and 15.4 % (0.5Fe-Si-1-750). When low calcination temperatures were applied, high levels of selectivity for hydrocarbon oxygenates (MeOH, FD and FA) were obtained, with a value of 96.6 % for 0.5Fe-Si-1-370 and 97.2 % for 0.5Fe-Si-1-450. Relative low values of TOFs (around 130 h⁻¹) and volumetric productivities (1.6×10^{-6} mol•ml⁻¹s⁻¹) were obtained for these two catalysts. When increasing the calcination temperature to 550 °C, a selectivity of hydrocarbon oxygenates of 98.8 % with obviously enhanced TOF of 210 h⁻¹ and volumetric productivity of 2.5×10^{-6} mol•ml⁻¹s⁻¹ was reached. The selectivity of CO₂ increased to 3.4 %. For 0.5Fe-Si-1-650, the selectivity of hydrocarbon oxygenates dropped to 96.8 % along with an obvious increase of the selectivity of CO₂ to 5.1 %. The TOF and the volumetric productivity also dropped to 189 h⁻¹ and 2.3×10^{-6} mol•ml⁻¹s⁻¹, respectively. If further increasing the calcination temperature to 750 °C, although the highest values of TOF (223 h⁻¹) and volumetric productivity (2.7×10^{-6} mol•ml⁻¹s⁻¹) were observed,

the highest value of 6.4 % for the selectivity of CO₂ was obtained, indicating a high level of over-oxidation. The selectivity of hydrocarbon oxygenates was 98.3 %.

Table 4.3. Catalytic results related to CH₄ for Fe-silicalite-1 catalysts calcined at different temperatures.

Catalyst	CH ₄ conversion %	Selectivity %					TOF h ⁻¹	Volume Prod mol•ml ⁻¹ s ⁻¹
		MeOH	FD	FA	CO ₂	Sum		
0.5Fe-Si-1-370	15.2	3.6	23.9	69.1	1.8	98.3	128	1.6×10 ⁻⁶
0.5Fe-Si-1-450	15.5	3.7	24.2	69.3	2.0	99.2	129	1.6×10 ⁻⁶
<i>0.5Fe-Si-1-550</i>	<i>17.1</i>	<i>4.0</i>	<i>22.4</i>	<i>72.4</i>	<i>3.4</i>	<i>102.2</i>	<i>210</i>	<i>2.5×10⁻⁶</i>
0.5Fe-Si-1-650	13.9	4.3	23.2	69.3	5.1	101.9	189	2.3×10 ⁻⁶
0.5Fe-Si-1-750	15.4	5.4	30.1	62.8	6.4	104.7	223	2.7×10 ⁻⁶

Reaction conditions: 0.1 g catalysts; reaction temperature: 100 °C; pressure: 40 bar; gas flow: 4 ml/min N₂ and 4 ml/min CH₄; liquid flow: 1.5 ml/min of 0.12 M aqueous H₂O₂ solution.

The catalytic results related to H₂O₂ for the catalysts calcined at different temperatures are summarized in Table 4.4. It could be found that with increasing calcination temperature, there was a clear trend of increasing H₂O₂ conversion, namely from 37.6 % for 0.5Fe-Si-1-370 to 77.1 % for 0.5Fe-Si-1-750. Similar trends though not so pronounced could be found for the selectivities of O₂ (which were increasing from 39.7 % to 48.5 %) and CO₂ (which were increasing from 1.9 % to 5.6 %). Relative high values for the selectivities of hydrocarbon oxygenates were obtained over 0.5Fe-Si-1-450 and 0.5Fe-Si-1-550, with values of 76.2 % and 69.1 %, respectively.

Table 4.4. Catalytic results related to H₂O₂ for Fe-silicalite-1 catalysts calcined at different temperatures.

Catalyst	H ₂ O ₂ conversion %	Selectivity %			
		O ₂	Hydrocarbon oxygenates	CO ₂	Sum
0.5Fe-Si-1-370	37.6	39.7	67.6	1.9	109.2
0.5Fe-Si-1-450	33.3	35.1	76.2	2.1	113.4
<i>0.5Fe-Si-1-550</i>	<i>60.5</i>	<i>33.8</i>	<i>69.1</i>	<i>3.6</i>	<i>106.5</i>
0.5Fe-Si-1-650	66.7	47.4	57.3	4.5	109.2
0.5Fe-Si-1-750	77.1	48.5	55.3	5.6	109.3

Reaction conditions: 0.1 g catalysts; reaction temperature: 100 °C; pressure: 40 bar; gas flow: 4 ml/min N₂ and 4 ml/min CH₄; liquid flow: 1.5 ml/min of 0.12 M aqueous H₂O₂ solution.

To summarize the catalytic results, with catalysts calcined at relative low temperatures, a higher level of selectivities to hydrocarbon oxygenates and a lower level of selectivities to CO₂ could be obtained. However, the TOFs and volumetric productivities were relatively low. On the other hand, higher calcination temperature such as 750 °C although leading to higher levels of TOFs and volumetric productivities, exhibited quite high conversions of H₂O₂ and quite high selectivities to O₂ and CO₂, indicating a much lower level for the utilization of H₂O₂ and a high degree of over-oxidation of methane. The catalyst calcined at 550 °C showed the largest value of methane conversion (17.1 %), a high level of TOF and volumetric productivity, the smallest value for the selectivity of O₂ (generated from the decomposition of H₂O₂) and a relative low level of over-oxidation. According to Hutchings and co-workers [63], the active sites for selective methane oxidation are binuclear Fe species that are generated from extra-framework iron species upon calcination. We observed that with increasing calcination temperature, more and more extra-framework iron species were formed and the TOFs and volumetric productivities were enhanced, though at the expense of an increased level of over-oxidation and H₂O₂ decomposition. One explanation may be that, at higher calcination temperatures, the extra-framework iron species form large aggregates that are not active in the selective oxidation of methane but showed higher activity in H₂O₂ decomposition. Zecchina and co-workers found that such large aggregates in Fe-silicalite-1 do not adsorb CO, N₂O or NO and they are attributed to silent “inactive” guests [118].

4.1.5 Summary

Sub-micrometer sized crystals of Fe-silicalite-1 possessing typical MFI structure were successfully synthesized. At a calcination temperature of 370 °C, most of the organic template could be removed. After calcination, migration of Fe species from framework to extra-framework positions was observed. Increasing calcination temperatures lead to an increasing fraction of extra-framework iron species with an increasing variety of types and structures. The charge-compensating extra-framework cationic sites generated by the introduction of framework Fe were mostly occupied by charged iron species, leading to weak acidity and low NH₃ desorption temperatures. Catalysts calcined at lower temperatures lead to higher levels of selectivity to hydrocarbon oxygenates with lower level of over-oxidation, but relative low values of the TOF and volumetric productivity were obtained. On the other side, higher calcination temperature lead to higher levels of TOFs and volumetric productivities but a much lower level for the utilization of H₂O₂ and a higher degree of over-oxidation were observed. The catalyst calcined at 550 °C

showed the best catalytic performance under given conditions. This calcination temperature seems to be a compromise between the formation of extra-framework binuclear Fe-clusters, which are able to selectively oxidize methane, and the formation of extra-framework iron aggregates, which seem to catalyze over-oxidation and H₂O₂ decomposition.

4.2 The influence of different Fe contents

4.2.1 Introduction

As described section 4.1, migration of Fe species from framework to extra-framework positions takes place upon calcination, thus potentially forming binuclear Fe species that were assumed to selectively oxidize methane. Higher calcination temperatures lead to an increase of extra-framework binuclear Fe species, but unfortunately, also of larger Fe oxide aggregates that are assumed to decompose H₂O₂ and over-oxidize towards CO₂ rather than selectively oxidize methane. Another strategy forming extra-framework binuclear Fe species or at least increase the probability of their formation could be to increase the Fe content of the as-synthesized template containing Fe-silicalite-1 samples. So, following this idea, in this part a series of Fe-silicalite-1 samples with increasing Fe contents were hydrothermally synthesized. These catalysts were characterized by XRD, low temperature N₂ adsorption-desorption, ICP-OES, TEM, H₂-TPR, NH₃-TPD, FT-IR and UV-Vis-DR techniques. Their catalytic activities were investigated and compared.

4.2.2 Catalysts

Different Fe contents of Fe-silicalite-1 were synthesized (see section 2.2.1). In the homogenization step before starting crystallization, different amounts of ferric citrate solution were added to the gel to obtain Fe contents of 0.5 wt. %, 1.2 wt. %, 2.0 wt. %, 2.6 wt. % and 3.7 wt. % in the calcined samples. After calcination at 550 °C, which turned out to be the optimal calcination temperature (see section 4.1.4), ion-exchange with an aqueous solution of NH₄(NO₃)₃ was performed. After drying, another calcination step at 550 °C was carried out to decompose the NH₄⁺ and obtain the H-form of these samples. They are denoted as H-0.5Fe-Si-1, H-1.2Fe-Si-1, H-2.0Fe-Si-1, H-2.6Fe-Si-1, and H-3.7Fe-Si-1. For comparison, wetness impregnation of a sub-micrometer sized silicalite-1 was performed as a typical and often used post-synthetic method introducing Fe. (see section 2.2.8). This sample is denoted as Fe-Si-1-WI.

4.2.3 Characterization results

Table 4.5 demonstrates the chemical compositions and textural properties of the catalysts possessing different Fe contents. For all the Fe-silicalite-1 samples, the final Fe contents (analyzed by ICP-OES) were lower than the ones expected due to the amount of Fe in the synthesis gel, revealing that only part of the Fe species provided by the Fe precursor is incorporated in the Fe-silicalite-1. The higher the Fe content, the larger the deviation between the expected Fe content and actual one. As the ionic radius for Fe^{3+} is 0.064 nm and for Si^{4+} it is only 0.041 nm, the insertion of Fe^{3+} into the lattice leads to the expansion of the unit cell, which is known from literature [119, 139, 144]. Thus, the higher the ratio of Fe/Si is, it is getting more and more difficult to insert Fe^{3+} into the lattice. For H-0.5Fe-Si-1, the measured apparent surface area was 438 m^2/g and the micropore volume was 0.15 cm^3/g . For H-1.2Fe-Si-1, the apparent surface area and micropore volume increased to 473 m^2/g and 0.17 cm^3/g , respectively. When further increasing the Fe contents, it is notable that the apparent surface area decreased from 473 m^2/g to 426 m^2/g and the micropore volume dropped gradually from 0.17 cm^3/g to 0.14 cm^3/g . This may be due to the fact that with increasing Fe contents, more Fe species move from framework to extra-framework positions and thus partially block the channels of the pores, leading to decreasing of apparent surface areas and micropore volumes. A similar trend was obtained for the external surface area with the exception of H-2.6Fe-Si-1 having the highest value of 104 m^2/g . For Fe-Si-1-WI, the Fe content was 2.83 wt. %, which was equal to that of H-3.7Fe-Si-1. Compared to the parent silicalite-1, the apparent external surface area and micropore volume dropped significantly, indicating that the Fe species partially block the pores of silicalite-1. Since on the other hand the external surface area was almost doubled, it can be concluded that large Fe-oxide aggregates are located at the outer surface of the crystals and increase the total outer surface area. This is also supported by the fact that the color of the obtained sample was red-brown.

Table 4.5. Chemical compositions and textural properties of Fe-silicalite-1 catalysts with different Fe contents.

Sample	Fe (wt. %)	$n_{\text{Fe}}/n_{\text{Si}}$	$S_{\text{BET}}^{\text{a}}$ (m ² /g)	S_{ex}^{b} (m ² /g)	V_{p}^{c} (cm ³ /g)
H-0.5Fe-Si-1	0.43	0.0045	438	95	0.15
H-1.2Fe-Si-1	0.88	0.0096	473	93	0.17
H-2.0Fe-Si-1	1.56	0.0177	459	87	0.16
H-2.6Fe-Si-1	2.10	0.0243	459	104	0.15
H-3.7Fe-Si-1	2.83	0.0331	426	85	0.14
silicalite-1	< 10 ppm	-	451	69	0.17
Fe-Si-1-WI	2.83	0.0334	380	129	0.09

^a apparent surface area, calculated by BET method. ^b apparent external surface area, calculated by t-plot method.

^c micropore volume, calculated by t-plot method.

The XRD patterns of the catalysts possessing different Fe contents are depicted in Figure 4.9. All samples show characteristic diffraction patterns of a typical MFI structure, indicating that the synthesis of these samples was successful and that the MFI structure remained largely unchanged even for high Fe contents. For the Fe-silicate-1 samples, the intensities of the reflexes decreased with increasing Fe contents, which may be due to the decrease of the crystallinity and/or the decrease of crystal size with increasing Fe contents (see next paragraph). No characteristic reflexes belonging to Fe oxides could be observed from the diffractograms of all the Fe-silicate-1 samples, suggesting that the Fe species were highly dispersed. The high dispersion of Fe species was also supported by the milk-white color of all finally obtained Fe-silicalite-1 samples, even for H-3.7Fe-Si-1 having the highest Fe content. For Fe-Si-1-WI, also no reflexes belonging to Fe oxides could be detected. However, it showed a red-brown color. The reason that despite the red-brown color no reflexes of Fe oxide occurred in the diffraction pattern could be, that the Fe oxide species are highly dispersed and too small to give reflexes, or their amount is too low to give reflexes beyond the detection limit of the XRD.

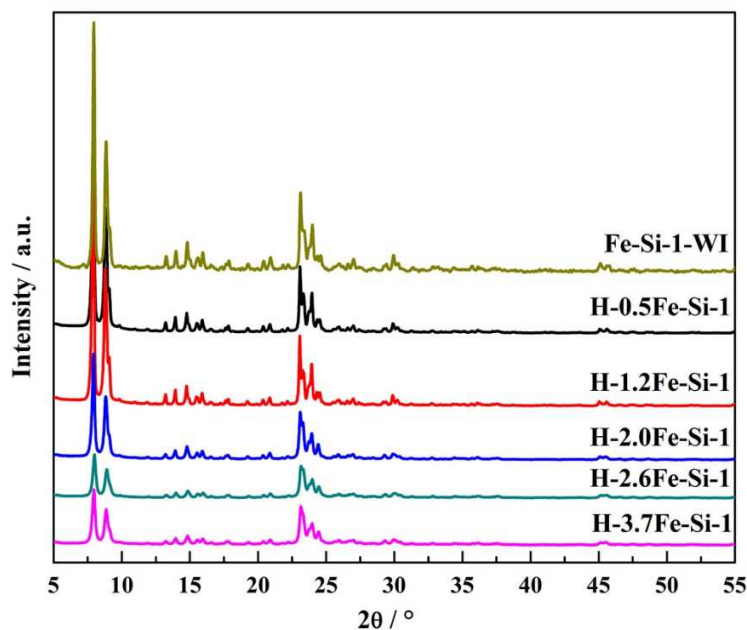


Figure 4.9. XRD patterns of Fe-silicalite-1 catalysts with different Fe contents.

Figure 4.10.a-e display TEM images of the catalysts. For H-0.5Fe-Si-1, crystals with a relative narrow size distribution ranging from 370 nm to 430 nm were obtained. These crystals showed smooth surfaces and clear edges. For H-1.2Fe-Si-1, the size of the crystals decreased and the distribution also broadened, now ranging from 290 nm to 490 nm. These crystals still exhibited smooth surfaces and clear edges. When the Fe content further increased, the morphology significantly changed. The crystal sizes decreased a lot and these much smaller crystals gathered together to form aggregates. For H-2.0Fe-Si-1 the aggregate size ranged between 330 and 510 nm with rough surfaces and edges. The significant drop of the crystal size is consistent with an obvious drop of the intensities of the reflexes in the XRD patterns. For H-2.6Fe-Si-1, a further drop of the crystal size could be observed with larger aggregates ranging from 460 nm to 650 nm. This trend is even more obvious for H-3.7Fe-Si-1, as the aggregate size increased a lot with a very broad distribution of sizes ranging from 720 nm to 1560 nm. The increasing Fe contents lead to significant changes of the morphology of the crystals, indicating that Fe plays an important role as nucleus of crystal growth in the preparation of Fe-silicalite-1 zeolites. Similar observations have also been reported by Inui et al. [145].

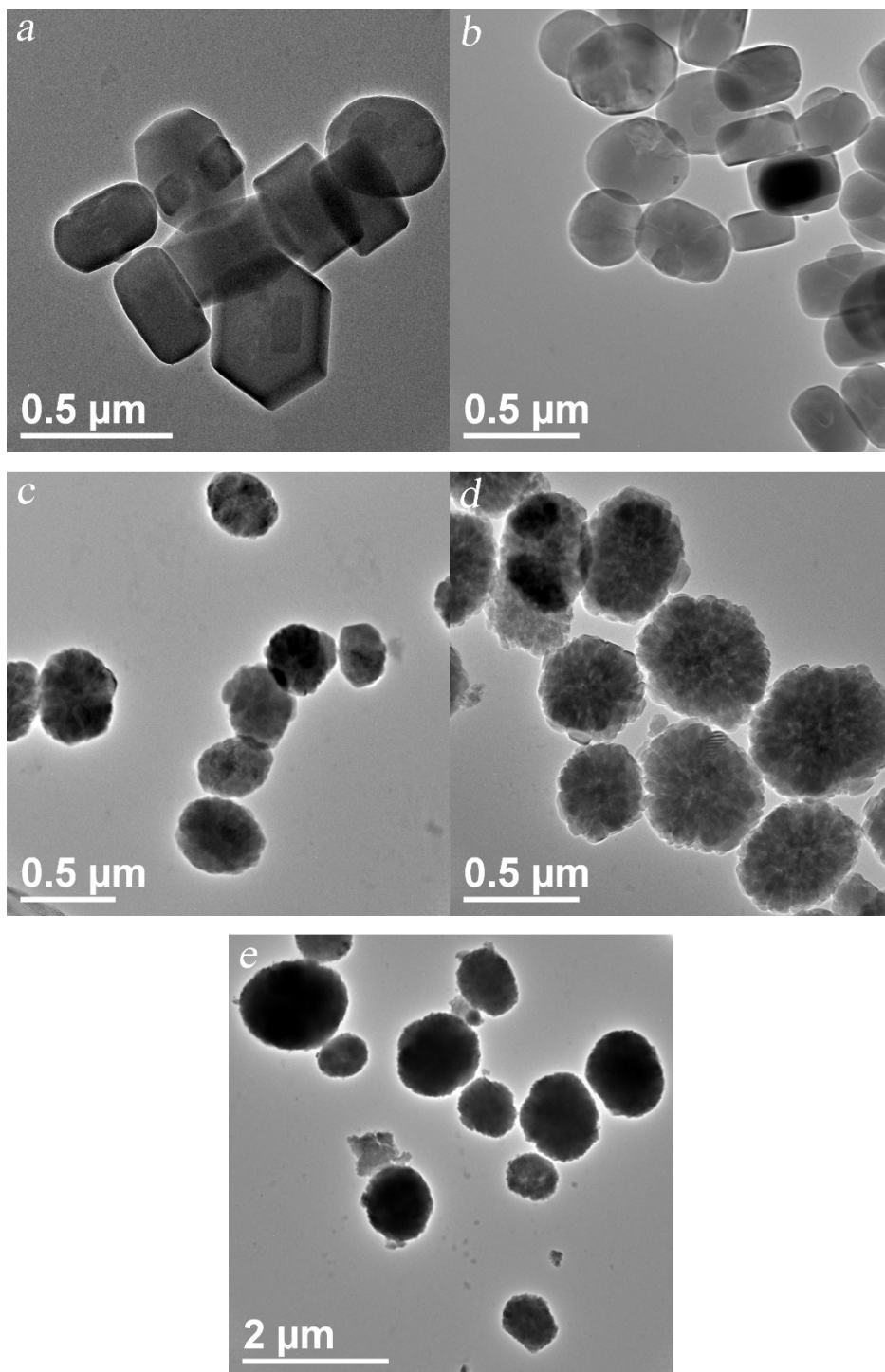


Figure 4.10. TEM images of Fe-silicalite-1 catalysts with different Fe contents. (a) H-0.5Fe-Si-1, (b) H-1.2Fe-Si-1, (c) H-2.0Fe-Si-1, (d) H-2.6Fe-Si-1, (e) H-3.7Fe-Si-1.

The NH_3 -TPD of the Fe-silicalite-1 catalysts having different Fe content is illustrated in [Figure 4.11](#). For Fe-Si-1-WI, which was prepared *via* a post-synthetic wetness impregnation method for

the loading of Fe on silicate-1, no acidity at all could be detected. For all the Fe-silicalite-1 catalysts with different Fe contents, two peaks appeared, one at a low temperature and one at a higher temperature, attributed to low and high acid strength, respectively. The high-temperature peak is attributed to Brønsted acid sites [119, 122], while the low-temperature peak is attributed to weak Brønsted acid sites or Lewis acid sites. With an increasing Fe content, the temperatures of the high-temperature NH_3 desorption peak continuously increased from 348 °C for H-0.5Fe-Si-1 to 380 °C for H-3.7Fe-Si-1. The areas of the desorption peaks also significantly increased. Similar trends can be observed also for the low-temperature NH_3 desorption peaks. These results indicate that, with increasing Fe contents, more Fe species located in the framework positions, leading to more Brønsted acid sites necessary to compensate the negative charge connected to Fe^{3+} being tetrahedrally coordinated.

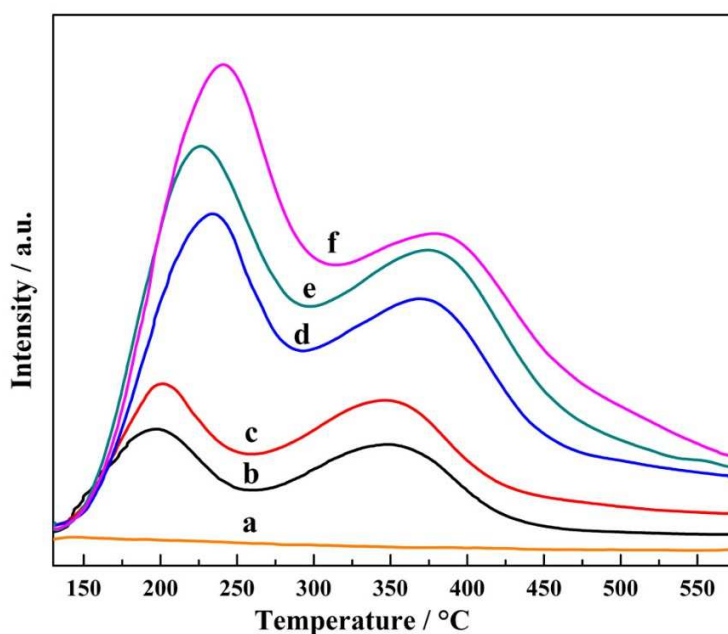


Figure 4.11. NH_3 -TPD profiles of Fe-silicalite-1 catalysts with different Fe contents. (a) Fe-Si-1-WI, (b) H-0.5Fe-Si-1, (c) H-1.2Fe-Si-1, (d) H-2.0Fe-Si-1, (e) H-2.6Fe-Si-1, (f) H-3.7Fe-Si-1.

Figure 4.12 shows the H_2 -TPR of Fe-silicalite-1 catalysts with different Fe contents. For H-0.5Fe-Si-1, a significant reduction peak with shoulders appeared at 804 °C and a relative small peak at 398 °C with a tiny shoulder at 496 °C could be observed. For H-1.2Fe-Si-1, the high-temperature reduction peak decreased to 762 °C with shoulders and the low-temperature reduction peak also dropped slightly to 395 °C. When further increasing the Fe content, the high-temperature reduction peaks and the low temperature reduction peaks continuously decreased to about 670 °C and 375 °C,

respectively, irrespective of the Fe content. The areas of reduction peaks significantly increased with the increasing Fe contents. The reduction peaks appearing below 450 °C can be attributed to isolated extra-framework iron species, reduction peaks appearing between 500 to 680 °C are assigned to the reduction of charge-compensating extra-framework Fe³⁺ species, and reduction peaks above 680 °C are attributed to framework Fe³⁺ species, as reported by Meloni et al. [139]. Thus, one can deduce that with increasing Fe contents both more insertion of Fe into the framework as well as more isolated extra-framework iron species could be found. The drop of the reduction temperatures for framework Fe³⁺ species revealed that with increasing Fe contents, the stability of framework Fe species is decreasing. Figure 4.13 shows the H₂-TPR of Fe-Si-1 WI. Reduction peaks appeared at 375 °C, 533 °C, 1012 °C and shoulder peaks at 495 °C, 650 °C and 695 °C could be found, indicating many different types Fe species in this catalyst.

Table 4.6 summarizes the hydrogen consumption during the H₂-TPR experiments and the ratio of the areas of the low-temperature reduction peak (area I) to the high-temperature reduction peak (area II) for the Fe-silicalite-1 catalysts with different Fe contents. One can conclude that for all Fe-silicalite-1 catalysts, no matter which Fe contents they have, the ratios of consumed H₂ to Fe were around 0.50, which is consistent with the theoretical value of 0.50 for the hydrogen reduction of Fe³⁺ to Fe²⁺. With increasing Fe contents, the ratio of area I to area II also increased, revealing a higher percentage of isolated extra-framework iron species. This is consistent with the observation obtained by low-temperature N₂ sorption that with increasing Fe contents, the apparent surface areas and micropore volumes decreased as the channels of the Fe-silicalite-1 may be partially blocked by these extra-framework iron species. For Fe-Si-1-WI, the ratio of consumed H₂ to Fe was 1.50, which coincides very well with the value for the reduction of Fe³⁺ to metallic Fe. This also indicates that it is much easier to reduce extra-framework Fe species, particularly if they are present as large Fe oxide aggregates.

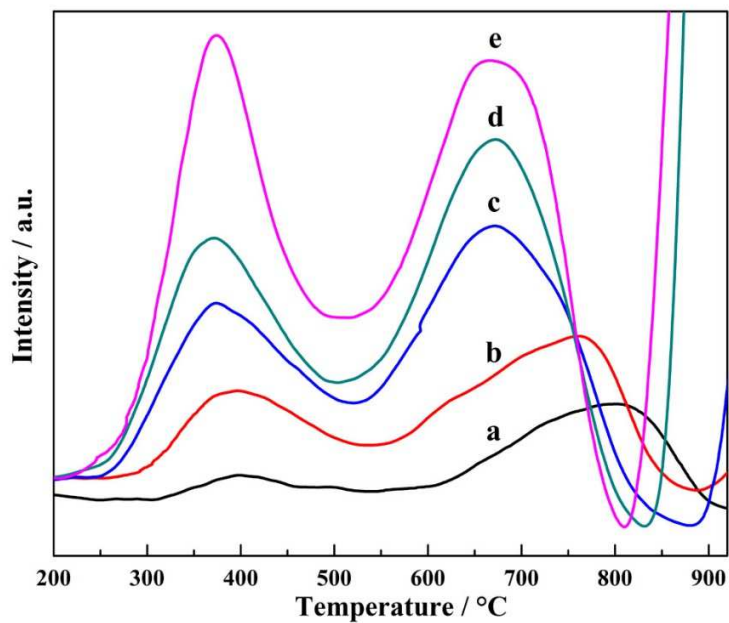


Figure 4.12. H₂-TPR profiles of Fe-silicalite-1 catalysts with different Fe contents. (a) H-0.5Fe-Si-1, (b) H-1.2Fe-Si-1, (c) H-2.0Fe-Si-1, (d) H-2.6Fe-Si-1, (e) H-3.7Fe-Si-1.

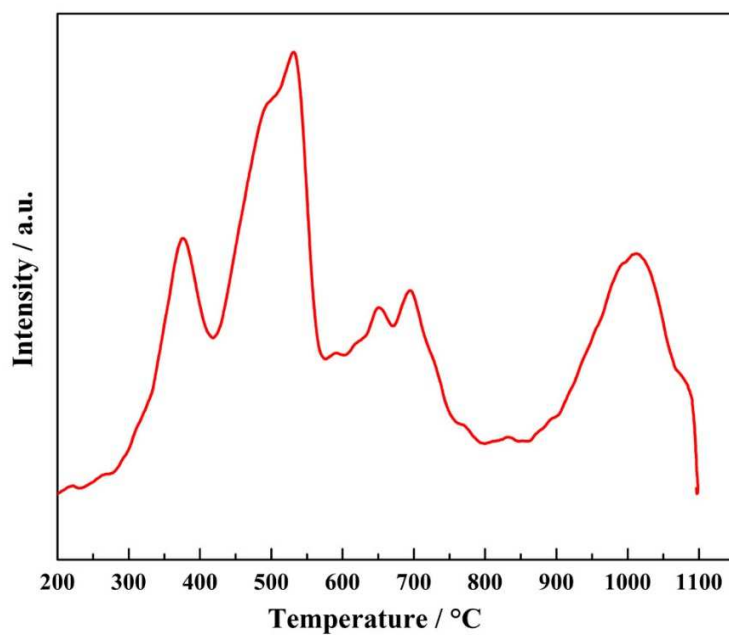


Figure 4.13. H₂-TPR profile of Fe-Si-1-WI.

Table 4.6. Hydrogen consumption in the H₂-TPR experiments and the ratio of different reduction peaks for Fe-silicalite-1 catalysts with different Fe contents. Area I: low temperature reduction peak area; area II: high temperature reduction peak area.

Sample	H ₂ /Fe consumption (mol/mol)	area I/area II
H-0.5Fe-Si-1	0.52	0.14
H-1.2Fe-Si-1	0.47	0.41
H-2.0Fe-Si-1	0.51	0.47
H-2.6Fe-Si-1	0.47	0.49
H-3.7Fe-Si-1	0.51	0.65
Fe-Si-1-WI	1.50	-

Figure 4.14 demonstrates the UV-Vis-DR spectra of the Fe-silicalite-1 catalysts with different Fe contents. According to Grünert and co-workers [114], the bands below 300 nm are assigned to Fe³⁺ ← O charge transfer bands of isolated Fe ions in tetrahedral or octahedral coordination and the band at around 350 nm is attributed to oligomeric clusters, while sub-bands above 400 nm are due to large Fe oxide aggregates. When increasing the Fe contents of the catalysts, the bands significantly shifted towards longer wavelengths with increased intensities, indicating that larger Fe oxide species were generated and the concentration of them increased considerably. This observation is consistent with the results of low-temperature N₂-sorption and H₂-TPR.

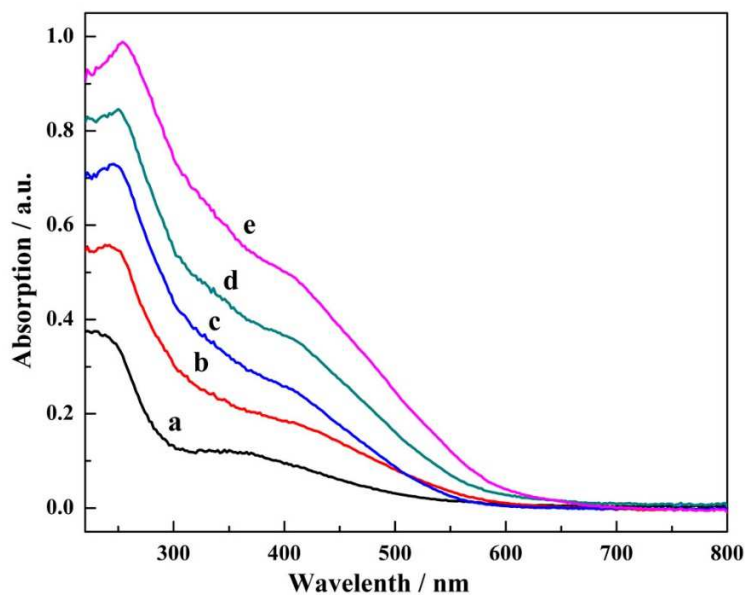


Figure 4.14. UV-Vis-DR spectra of Fe-silicalite-1 catalysts with different Fe contents. (a) H-0.5Fe-Si-1, (b) H-1.2Fe-Si-1, (c) H-2.0Fe-Si-1, (d) H-2.6Fe-Si-1, (e) H-3.7Fe-Si-1.

FT-IR spectra of the Fe-silicalite-1 catalysts with different Fe contents are illustrated in [Figure 4.15](#). For H-0.5Fe-Si-1, an obvious absorption peak appeared at 686 cm^{-1} with a shoulder peak observed at around 697 cm^{-1} . The band at 686 cm^{-1} is assigned to the characteristic Si-O-Fe linkage [137, 138]. When increasing the Fe contents, the shoulder peak at 697 cm^{-1} strengthened and the peak at 686 cm^{-1} became weaker and weaker and at a certain point these two peaks merged together. It indicates that different types of Si-O-Fe linkages were obtained with increasing Fe contents. These new Si-O-Fe linkages showed less stability against the H_2 reduction as observed from the H_2 -TPR results.

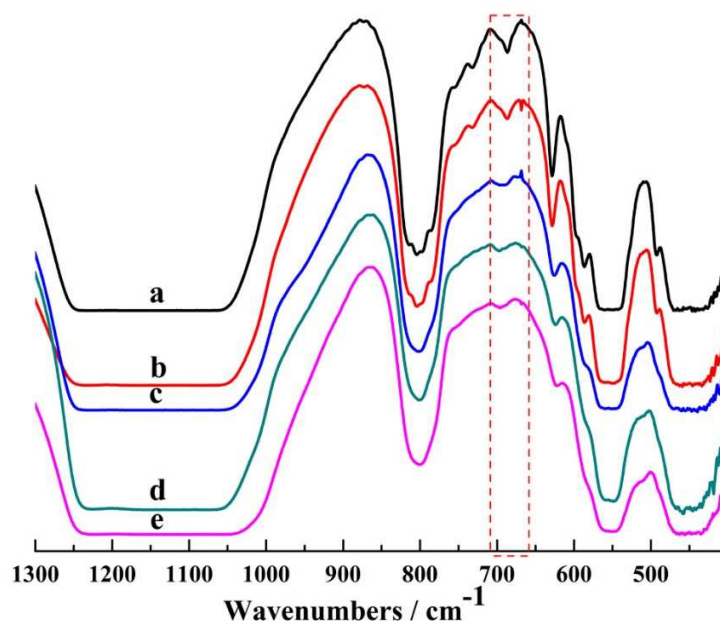


Figure 4.15. FT-IR spectra of Fe-silicalite-1 catalysts with different Fe contents. (a) H-0.5Fe-Si-1, (b) H-1.2Fe-Si-1, (c) H-2.0Fe-Si-1, (d) H-2.6Fe-Si-1, (e) H-3.7Fe-Si-1.

4.2.4 Catalytic results and discussion

Table 4.7 summarizes the catalytic results related to CH₄ for different Fe-silicalite-1 catalysts with different Fe contents. No catalytic activity could be detected for Fe-Si-1-WI, although it contains a considerable amount of Fe (see Table 4.5). For H-0.5Fe-Si-1, a methane conversion of 17.4 % with a hydrocarbon oxygenates (MeOH, FD and FA) selectivity of 95.7 % was obtained. The selectivity of CO₂ was 6.4 % and high values of TOF (228 h⁻¹) and volumetric productivity ($2.6 \times 10^{-6} \text{ mol} \cdot \text{ml}^{-1} \cdot \text{s}^{-1}$) were observed. For H-1.2Fe-Si-1, the conversion of methane was 15.8 % and the selectivity of hydrocarbon oxygenates was 91.8 %. The selectivity of CO₂ significantly increased to 12.5 % with the TOF and volumetric productivity obviously dropping to 95 h⁻¹ and $2.3 \times 10^{-6} \text{ mol} \cdot \text{ml}^{-1} \cdot \text{s}^{-1}$, respectively. When further increasing Fe contents, the conversion of methane increased to 19.4 % for H-2.0Fe-Si-1 and 20.0 % for H-2.6Fe-Si-1. However, the selectivity of hydrocarbon oxygenates steadily decreased from 91.8 % to 85.8 % and, conversely, the selectivity of CO₂ steadily increased from 12.5 % to 15.8 %. A steady drop of the TOFs (from 95 h⁻¹ to 36 h⁻¹) and the volumetric productivities (from $2.3 \times 10^{-6} \text{ mol} \cdot \text{ml}^{-1} \cdot \text{s}^{-1}$ to $2.1 \times 10^{-6} \text{ mol} \cdot \text{ml}^{-1} \cdot \text{s}^{-1}$) was also observed. For H-3.7Fe-Si-1, the conversion of methane considerably decreased to 16.8 % with the selectivity of hydrocarbon oxygenates dropping to 81.9 %. The lowest values of TOF (26 h⁻¹) and volumetric productivity ($2.0 \times 10^{-6} \text{ mol} \cdot \text{ml}^{-1} \cdot \text{s}^{-1}$) were reached with this catalyst.

Table 4.7. Catalytic results related to CH₄ for Fe-silicalite-1 catalysts with different Fe contents.

Catalyst	CH ₄ conversion %	Selectivity %					TOF h ⁻¹	Volume Prod mol•ml ⁻¹ s ⁻¹
		MeOH	FD	FA	CO ₂	Sum		
H-0.5Fe-Si-1	17.4	4.7	35.2	55.7	6.4	102.1	228	2.6×10 ⁻⁶
H-1.2Fe-Si-1	15.8	4.7	36.7	50.4	12.5	104.3	95	2.3×10 ⁻⁶
H-2.0Fe-Si-1	19.4	3.3	39.9	45.4	12.8	101.4	54	2.3×10 ⁻⁶
H-2.6Fe-Si-1	20.0	2.9	39.3	43.6	15.8	101.6	36	2.1×10 ⁻⁶
H-3.7Fe-Si-1	16.8	5.9	37.6	38.4	17.3	99.2	26	2.0×10 ⁻⁶
Fe-Si-1-WI	0.3	0	0	0	0	0	0	0

Reaction conditions: 0.1 g catalysts; reaction temperature: 100 °C; pressure: 40 bar; gas flow: 4 ml/min N₂ and 4 ml/min CH₄; liquid flow: 1.5 ml/min of 0.12 M aqueous H₂O₂ solution.

Catalytic results related to H₂O₂ for Fe-silicalite-1 catalysts with different Fe contents are shown in Table 4.8. For Fe-Si-1 WI, no hydrocarbon oxygenates and no CO₂ could be detected with O₂ being the only product, suggesting that only the decomposition of H₂O₂ took place over this catalyst. It could be found that with the increasing Fe contents, the conversion of H₂O₂ steadily increased from 83.6 % to 100 % and the selectivity to hydrocarbon oxygenates steadily decreased from 49.0 % to 29.0 %, indicating a drop of the efficiency of H₂O₂ utilization. The selectivity of CO₂ also increased steadily from 5.3 % to 10.2 %, revealing that at higher Fe contents, more H₂O₂ participated in the over-oxidation of methane leading to higher levels of CO₂.

Table 4.8. Catalytic results related to H₂O₂ for Fe-silicalite-1 catalysts with different Fe contents.

Catalyst	H ₂ O ₂ conversion %	Selectivity %			
		O ₂	Hydrocarbon oxygenates	CO ₂	Sum
H-0.5Fe-Si-1	83.6	58.7	49.0	5.3	112.9
H-1.2Fe-Si-1	98.6	73.4	35.1	7.7	116.2
H-2.0Fe-Si-1	99.8	72.9	34.5	8.0	115.4
H-2.6Fe-Si-1	100	71.6	31.4	9.3	112.3
H-3.7Fe-Si-1	100	76.7	29.0	10.2	115.9
Fe-Si-1-WI	45.6	108.3	0	0	108.3

Reaction conditions: 0.1 g catalysts; reaction temperature: 100 °C; pressure: 40 bar; gas flow: 4 ml/min N₂ and 4 ml/min CH₄; liquid flow: 1.5 ml/min of 0.12 M aqueous H₂O₂ solution.

4.2.5 Summary

Fe-silicalite-1 catalysts with different Fe contents were successfully synthesized. It was found that with increasing Fe contents, the crystal sizes decreased and the morphology of the crystals also changed, indicating that Fe plays an important role as nucleus of crystal growth in the synthesis of Fe-silicalite-1 zeolites. With increasing Fe contents, the amount of both framework and extra-framework iron species and the acidity also increased. Higher Fe contents lead to large extra-framework iron aggregates, which may be inactive for the selective oxidation of methane but active for H₂O₂ decomposition. A relative low Fe content (e.g., around 0.5 wt. %) is preferable for the catalytic reaction under given conditions. The sample based on silicalite-1 prepared by post-synthetic wetness impregnation method for the loading of Fe showed characterization results very different from other Fe-silicalite-1 catalysts and no catalytic activity could be observed on this catalyst. A special structure of Fe species, most likely binuclear Fe clusters, are needed as active sites for the selective oxidation of methane. These Fe species can be simply obtained by just increasing the Fe content of the catalysts, but the formation of larger extra-framework Fe-oxide clusters seems to be not avoidable. These larger extra-framework Fe-oxide clusters seem to be responsible for H₂O₂ decomposition and over-oxidation to CO₂.

4.3 The influence of different crystal sizes

4.3.1 Introduction

Avoiding of mass transport limitations is of significant importance for heterogeneously catalyzed reactions to obtain higher conversions and productivities of the desired product. As it has been shown in chapter 3, with a micro fixed-bed reactor and by using of sub-micrometer sized catalysts for the selective oxidation of methane with aqueous H₂O₂, the conversion of methane increased more than one order of magnitude and oxygenate productivity could be enhanced nearly three orders of magnitude. The micro fixed-bed reactor may decrease the thickness of the liquid film covering the surface of the solid catalyst, thus decreasing the resistance of external mass transport. On the other hand, by decreasing the crystal sizes of the catalyst, the internal mass transport of the reactants could be intensified, because the diffusion path length through the channels of the zeolite is decreased. In our reaction system, there are two additional aggravating factors. Firstly, our reaction system is a three-phase system comprising a solid (catalysts), a liquid (aqueous H₂O₂ solution) and a gas (methane and nitrogen). In such three-phase system, the mass transport of the gaseous reactant is often seriously hampered due to the low solubility of the gas in the liquid and

the corresponding small concentration gradient. Secondly, the catalyst powder was pressed, crushed and sieved to get agglomerates of 200 -315 μm in diameter, which were filled into the reactor. Thus, an additional diffusion resistance in the agglomerates has to be kept in mind. Figure 4.16 visualizes the rather complex situation due to the mass transport of methane from the gas over the liquid phase to the active sites where the reaction occurs. Anyway, it would be interesting to investigate the influence of different crystal sizes of Fe-silicalite-1 for the selective oxidation of methane, because it might be expected that the largest diffusion resistance lies in the micropores of the crystals. In the following, three Fe-silicalite-1 catalysts with different crystal sizes but similar Fe contents were synthesized. The physicochemical properties of the catalysts were characterized by ICP-OES, low-temperature N_2 adsorption-desorption, XRD, H_2 -TPR, NH_3 -TPD and TEM techniques. Same reaction conditions were adjusted and the catalytic performance was determined and compared.

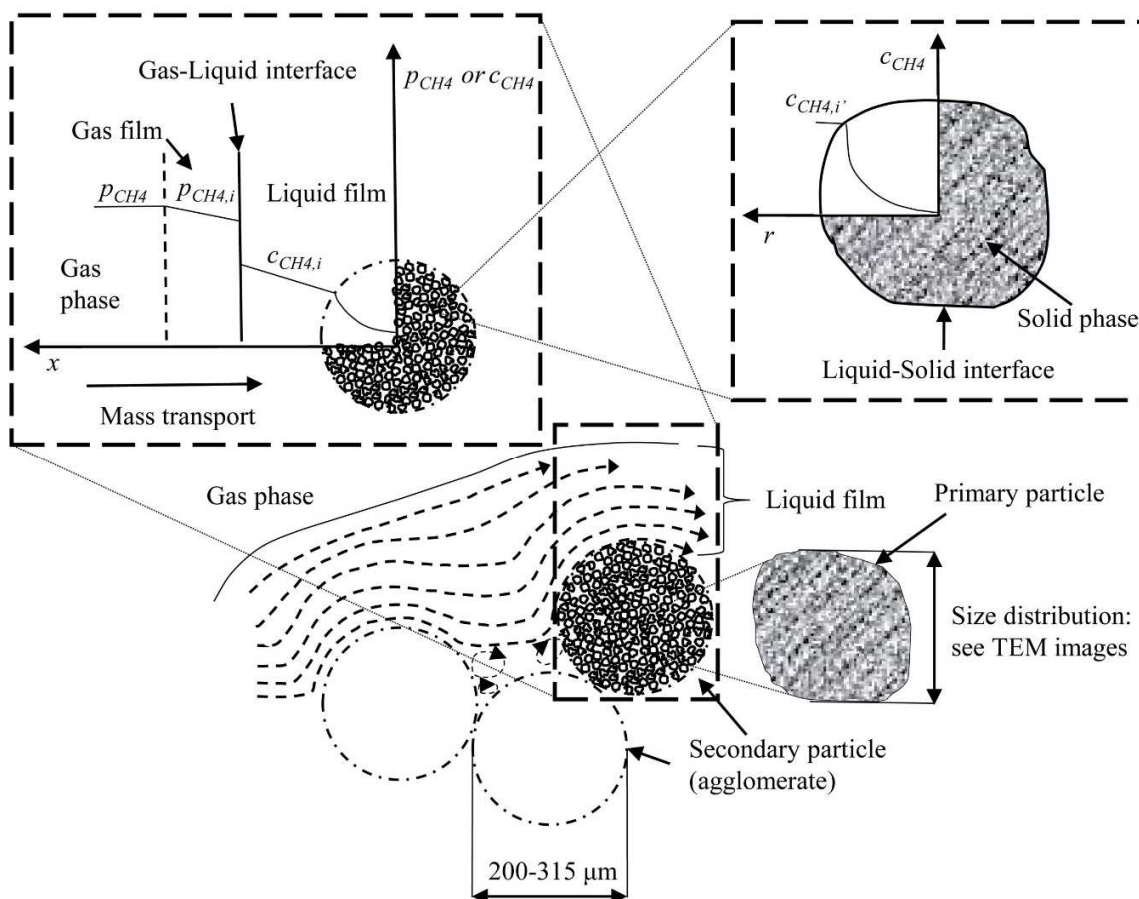


Figure 4.16. Simplified schematic for the mass transport of methane from the gas over the liquid phase to the solid phase in the three-phase system.

4.3.2 Catalysts

Fe-silicalite-1 with similar Fe contents but different crystal sizes were hydrothermally synthesized. Starting from the standard synthesis procedure of Fe-silicalite-1 chosen in this work (see section 2.2.1), sub-micrometer sized crystals are obtained. The catalyst is denoted as H-0.5Fe-Si-1. In order to obtain larger crystal sizes, the same recipe was used but the gel was diluted and the crystallization time was extended to 5 days (see section 2.2.2). The finally obtained material is denoted as H-0.5Fe-Si-1-LC. In order to obtain smaller crystals, the same recipe described in section 2.2.1 was used but a more concentrated mixture of the synthesis gel was chosen (see section 2.2.3). The obtained sample is denoted as H-0.5Fe-Si-1-SC.

4.3.3 Characterization results

Table 4.9 shows the chemical compositions and textural properties of the Fe-silicalite-1 catalysts with different crystal sizes. Similar Fe contents of around 0.40 wt. % were obtained. These three catalysts also exhibited textural properties very close to each other. Similar values of apparent surface areas, apparent external surface areas and micropore volumes were obtained.

Table 4.9. Chemical compositions and textural properties of Fe-silicalite-1 catalysts with different crystal sizes.

Sample	Fe (wt. %)	$n_{\text{Fe}}/n_{\text{Si}}$	$S_{\text{BET}}^{\text{a}}$ (m^2/g)	S_{ex}^{b} (m^2/g)	V_{p}^{c} (cm^3/g)
H-0.5Fe-Si-1-LC	0.41	0.0044	442	91	0.16
H-0.5Fe-Si-1	0.43	0.0045	438	95	0.15
H-0.5Fe-Si-1-SC	0.39	0.0042	445	105	0.15

^a apparent surface area, calculated by BET method. ^b apparent external surface area, calculated by t-plot method. ^c micropore volume, calculated by t-plot method.

The XRD patterns of the Fe-silicalite-1 catalysts with different crystal sizes are depicted in Figure 4.17. Characteristic reflexes of the MFI structure can be seen in all diffractograms, indicating the successful synthesis of these samples. It can be also concluded that the MFI structures were largely preserved even after liquid ion exchange and calcination. In none of the diffractograms characteristic diffraction peaks belonging to Fe oxides species could be observed, suggesting that the Fe species were highly dispersed. The high dispersion of Fe species was also supported by the milk-white color of all finally obtained samples.

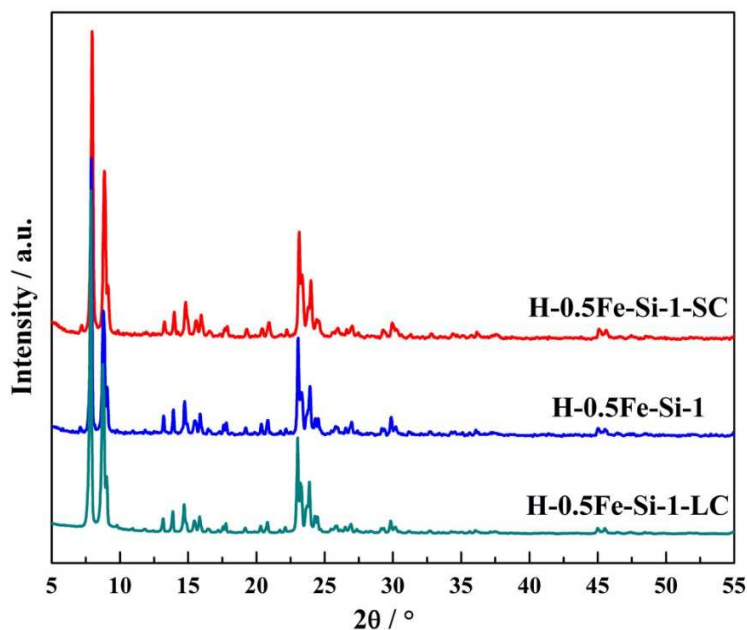


Figure 4.17. XRD patterns of Fe-silicalite-1 catalysts with different crystal sizes.

Figure 4.18.a-d displays TEM and SEM images of the catalysts. For H-0.5Fe-Si-1-SC, the crystal sizes ranged from 70 nm to 155 nm with most crystal sizes around 140 nm. For H-0.5Fe-Si-1, the obtained crystals showed smooth surfaces and clear edges with a relative narrow size distribution ranging from 370 nm to 430 nm. For H-0.5Fe-Si-1-LC, as the crystals were too thick for electrons to transmit through it in the TEM measurement, a SEM image was taken and shown in Figure 4.18.d. The crystals have very smooth surfaces and clear edges with sizes ranging from 5.3 μm to 5.6 μm .

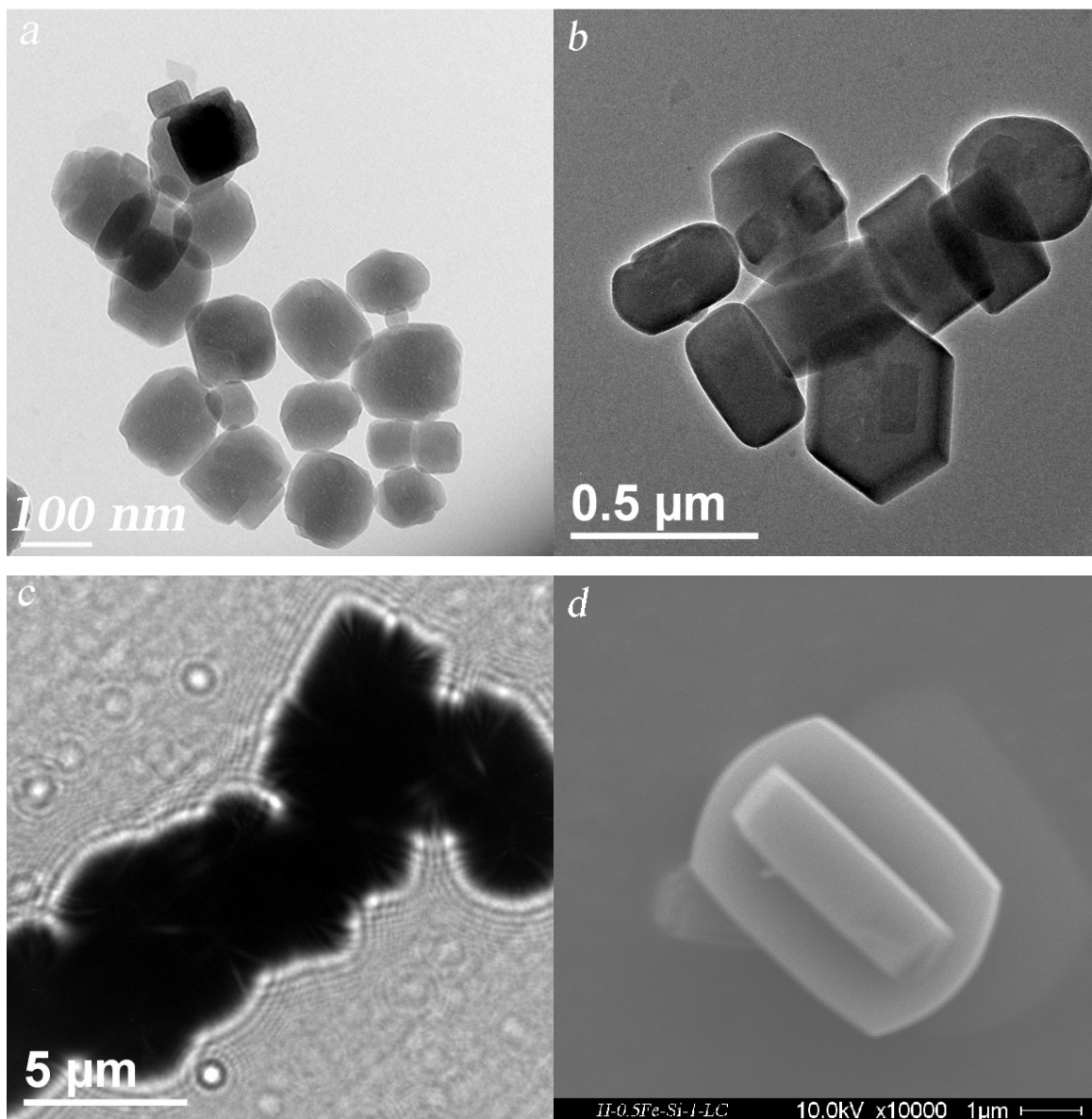


Figure 4.18. TEM images and SEM image of Fe-silicalite-1 catalysts with different crystal sizes. TEM images for (a) H-0.5Fe-Si-1-SC, (b) H-0.5Fe-Si-1, (c) H-0.5Fe-Si-1-LC and SEM image of (d) H-0.5Fe-Si-1-LC.

Figure 4.19 illustrates the NH_3 -TPD of the Fe-silicalite-1 catalysts with different crystal sizes. For all the catalysts, mainly two peaks appeared, one at a low temperature and one at a relative high temperature, which can be attributed to weak and strong acid sites, respectively. For H-0.5Fe-Si-1-SC, the NH_3 desorption temperatures appeared at 185 °C and 329 °C. With increasing crystal size, for H-0.5Fe-Si-1 and H-0.5Fe-Si-1-LC the desorption peaks at low and high temperatures significantly increased to ca. 200 °C and ca. 350 °C, respectively. This could be an indication that even for NH_3 mass transport limitation sets in or increases. Furthermore, the desorption areas

increased, indicating that the amount of adsorbed NH_3 on H-0.5Fe-Si-1 and on H-0.5Fe-Si-1-LC was much larger compared to that of H-0.5Fe-Si-1-SC. For H-0.5Fe-Si-1-LC, the area belonging to weak acid sites increased and that of the strong acid sites dropped obviously, compared to that of H-0.5Fe-Si-1.

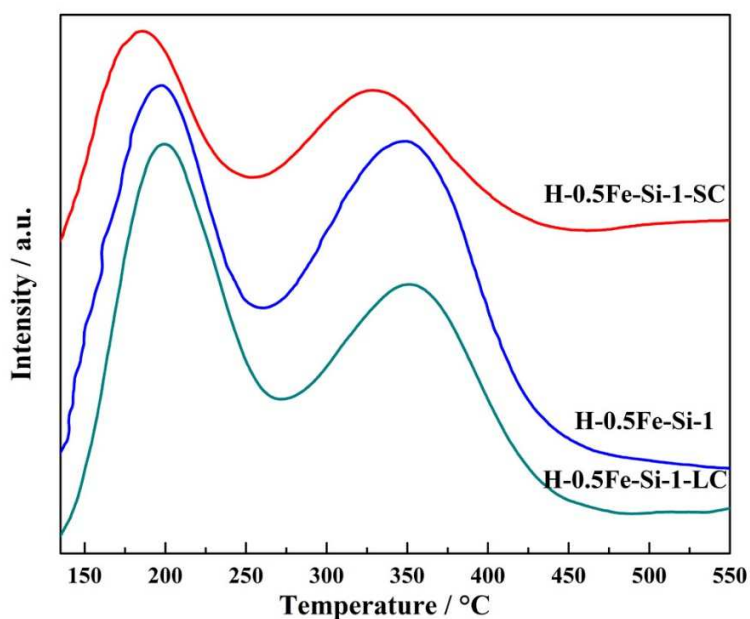


Figure 4.19. NH_3 -TPD profiles of Fe-silicalite-1 catalysts with different crystal sizes.

Figure 4.20 depicts the H_2 -TPR profiles of the catalysts. Table 4.10 summarizes the hydrogen consumption in the H_2 -TPR experiments and the ratio of the areas of the low temperature reduction peak (area I) to the high temperature reduction peak (area II). For H-0.5Fe-Si-1-SC, two shoulder peaks appeared within the high reduction temperature range at 735 °C and 671 °C. In the low temperature range, one peak at 448 °C with a shoulder at 383 °C could be observed. The ratio of consumed H_2 to Fe was 0.49, which is very close to the theoretical value of 0.50 for the hydrogen reduction of Fe^{3+} to Fe^{2+} . The ratio of area I to area II was 0.98, indicating that the amount of extra-framework Fe species was nearly equal to that of framework ones. For H-0.5Fe-Si-1, an obvious peak appeared at 804 °C and two shoulder peaks could be noticed at 398 °C and 496 °C. The ratio of consumed H_2 to Fe was 0.52, which coincides well with the value for the reduction of Fe^{3+} to Fe^{2+} . The ratio of area I to area II was 0.14, revealing most of the Fe species located in the framework. For H-0.5Fe-Si-1-LC, a main reduction peak appeared at 726 °C and two shoulder peaks at 372 °C and 434 °C. The ratio of consumed H_2 to Fe was 0.57, suggesting some Fe oxide

species were reduced to metallic Fe. From the value of the ratio of area I to area II of 0.33, one can deduce that more Fe species existed in the framework positions.

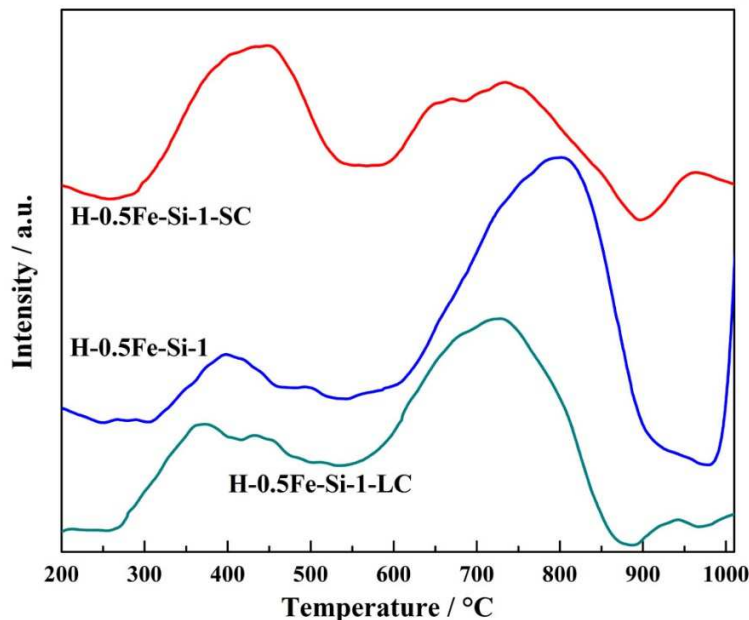


Figure 4.20. H₂-TPR profiles of Fe-silicalite-1 catalysts with different crystal sizes.

Table 4.10. Hydrogen consumption during the H₂-TPR experiments and the ratio of different reduction peaks for Fe-silicalite-1 catalysts with different crystal sizes. Area I: low temperature reduction peak area; area II: high temperature reduction peak area.

Sample	H ₂ /Fe consumption (mol/mol)	area I/area II
H-0.5Fe-Si-1-LC	0.57	0.33
H-0.5Fe-Si-1	0.52	0.14
H-0.5Fe-Si-1-SC	0.49	0.98

4.3.4 Catalytic results and discussion

Table 4.11 summarizes catalytic results related to CH₄ for the Fe-silicalite-1 catalysts with different crystal sizes. For H-0.5Fe-Si-1-LC, a methane conversion of 10.3 % with a hydrocarbon oxygenates (MeOH, FD and FA) selectivity of 101.3 % (a total selectivity sum of 103.3 % was reached) was obtained. The selectivity to CO₂ was 2.0 % and the TOF and volumetric productivity were 147 h⁻¹ and 1.6×10⁻⁶ mol•ml⁻¹s⁻¹, respectively. For H-0.5Fe-Si-1, the conversion of methane

significantly increased to 17.4 % and a hydrocarbon oxygenates selectivity of 95.7 % was obtained. The selectivity to CO₂ increased to 6.4 %. However, the TOF and volumetric productivity considerably increased to 228 h⁻¹ and 2.6×10⁻⁶ mol•ml⁻¹s⁻¹, respectively. These results indicate that when the crystal size was roughly 15 times smaller compared to H-0.5Fe-Si-1-LC (see [Figure 4.18](#)), significant enhancement of catalytic activity could be obtained, although with a higher level of over-oxidation. It is interesting that when further decreasing the crystal size close to nanometer-size, for H-0.5Fe-Si-1-SC, the conversion of methane dropped more than two times with a value of 8.6 %. The selectivities to hydrocarbon oxygenates and CO₂ were 99.0 % and 5.4 %, respectively. The TOF and volumetric productivity also obviously dropped to 165 h⁻¹ and 1.7×10⁻⁶ mol•ml⁻¹s⁻¹, respectively.

Table 4.11. Catalytic results related to CH₄ for Fe-silicalite-1 catalysts with different crystal sizes.

Catalyst	CH ₄ conversion %	Selectivity %					TOF h ⁻¹	Volume Prod mol•ml ⁻¹ s ⁻¹
		MeOH	FD	FA	CO ₂	Sum		
H-0.5Fe-Si-1-LC	10.3	4.7	40.4	56.2	2.0	103.3	147	1.6×10 ⁻⁶
H-0.5Fe-Si-1	17.4	4.7	35.2	55.7	6.4	102.1	228	2.6×10 ⁻⁶
H-0.5Fe-Si-1-SC	8.6	4.6	29.4	65.0	5.4	104.4	165	1.7×10 ⁻⁶

Reaction conditions: 0.1 g catalysts; reaction temperature: 100 °C; pressure: 40 bar; gas flow: 4 ml/min N₂ and 4 ml/min CH₄; liquid flow: 1.5 ml/min of 0.12 M aqueous H₂O₂ solution.

The catalytic results related to H₂O₂ for the Fe-silicalite-1 catalysts with different crystal sizes are demonstrated in [Table 4.12](#). For H-0.5Fe-Si-1-LC, the conversion of H₂O₂ was 68.0 % with an O₂ selectivity of 63.0 %. The selectivities to hydrocarbon oxygenates and CO₂ were 36.8 % and 1.2 %, respectively. For H-0.5Fe-Si-1 with sub-micrometer sized crystals, the conversion of H₂O₂ increased to 83.6 % and the selectivity of O₂ dropped to 58.7 %. The selectivity to hydrocarbon oxygenates considerably increased to 49.0 %, however, also CO₂ selectivity increased to 5.3 %. If further decreasing the crystal size, a H₂O₂ conversion of 53.4 % with an O₂ selectivity of 59.5 % was obtained. The selectivities to hydrocarbon oxygenates and CO₂ were 51.8 % and 4.3 %, respectively.

Table 4.12. Catalytic results related to H₂O₂ for Fe-silicalite-1 catalysts with different crystal sizes.

Catalyst	H ₂ O ₂ conversion %	Selectivity %			
		O ₂	Hydrocarbon oxygenates	CO ₂	Sum
H-0.5Fe-Si-1-LC	68.0	63.0	36.8	1.2	100.9
H-0.5Fe-Si-1	83.6	58.7	49.0	5.3	112.9
H-0.5Fe-Si-1-SC	53.4	59.5	51.8	4.3	115.6

Reaction conditions: 0.1 g catalysts; reaction temperature: 100 °C; pressure: 40 bar; gas flow: 4 ml/min N₂ and 4 ml/min CH₄; liquid flow: 1.5 ml/min of 0.12 M aqueous H₂O₂ solution.

One can conclude, that the catalysts with either larger crystal size (e.g., around 5.5 μm) or smaller crystal size (e.g., around 140 nm) showed lower values of methane conversion, TOFs and volumetric productivities. In other words, over H-0.5Fe-Si-1 with sub-micrometer crystal size of around 400 nm, although a relative high level of over-oxidation was observed, highest values of methane conversion together with highest values of TOF and volumetric productivity were reached. These observations may be explained as follows. For the catalytic performance experiments (also the experiments of H₂-TPR and NH₃-TPD), all the catalysts powder were firstly pressed, then crushed and finally sieved to yield agglomerates of 200-315 μm in diameter (see section 2.4). If the crystal size of the primary particles are too small, after pressing, the space between these primary crystals is very small, leading to smaller pores within the secondary agglomerate particles. This may lead to a worse internal mass transport. For the large crystal size of H-0.5Fe-Si-1-LC, although the secondary pores between the primary crystals are much larger, compared to sub-micrometer crystals, a much longer diffusion length exists through the channels of the crystals, leading also to a worse internal mass transport. These results indicate that a preferable crystal size seems to be around 400 nm, which allows large enough secondary pores, and small enough primary particles. However, it has to be kept in mind that especially for the nearly nano-sized H-0.5Fe-Si-1-SC, the distribution of Fe sites significantly changed having more extra-framework Fe sites. This could be also an explanation for its different catalytic performance.

4.3.5 Summary

Three kinds of Fe-silicalite-1 catalysts with different crystal sizes around 140 nm, 400 nm and 5.5 μm were successfully synthesized. These catalysts showed similar Fe contents and textural

properties. They exhibited different acidities and hydrogen reduction properties. Catalytic results showed that too large or too small crystal sizes of Fe-silicalite-1 lead to lower conversions, TOFs and volumetric productivities. A crystal size of about 400 nm seems to be preferable for the selective oxidation of methane under given conditions.

4.4 The influence of different acidities

4.4.1 Introduction

As described in section 1.4.2, Hellgardt and co-workers prepared Cu- and/or Fe-containing ZSM-5 catalysts by post-synthetic methods of solid state ion exchange and wetness impregnation for the selective oxidation of methane in aqueous H₂O₂ solution [126]. It was found that, by increasing the number of acid sites, a significant enhancement of catalytic activity was observed, leading to the assumption that Brønsted acid sites play an important role for the formation of a special structure of active extra-framework Fe species by providing appropriate positions for them. In section 4.2, we found that Fe-Si-1-WI, prepared *via* post-synthetic wetness impregnation of Fe on silicalite-1, showed no catalytic activity. Although this catalyst contains considerable amount of Fe species, as expected no acidity of Fe-Si-1-WI was detected in NH₃-TPR (see [Figure. 4.11](#)). Therefore, for this observation two explanations seem to be possible. One is that with the non-acidic silicalite-1, the necessary structure of Fe species as active sites can not be formed because acidity is required for their formation. This explanation follows the findings of Hellgardt and co-workers. The other possible explanation could be that the catalyst possesses active extra-framework Fe species, but acid sites are necessary as an indispensable promoter for the activation of methane under given conditions. To figure out if the last explanation holds true, in the following, the influence of different acidities of Fe-silicalite-1 catalysts was investigated.

4.4.2 Catalysts

Starting from the dried template containing Fe-silicalite-1 sample (see section 2.2.1), after calcination at 550 °C, the obtained material is denoted as 0.5Fe-Si-1-550. After the common procedure of liquid ion-exchange with a solution of NH₄(NO₃)₃ and another necessary calcination step at 550 °C, the H-form of sample can be obtained. It is denoted as H-0.5Fe-Si-1. This sample was transferred to the Na-form *via* another liquid ion-exchanged process with a solution of NaNO₃ followed by drying and calcination at 550 °C (see section 2.2.6). The obtained sample is denoted as Na-0.5Fe-Si-1-LIE. Another route to obtain the Na-form of Fe-silicalite-1 is adding the source

of Na already in the gel before starting crystallization (see section 2.2.9). The obtained sample is denoted as Na-0.5Fe-Si-1-S.

4.4.3 Characterization results

Table 4.13 shows the chemical compositions and textural properties of the catalysts. As expected, Fe contents around 0.40 wt. % were measured for all the catalysts. It is noticeable that the molar ratio of Na to Fe was 3.09 for Na-0.5Fe-Si-1-LIE and 1.08 for Na-0.5Fe-Si-1-S. Similar textural properties were obtained for 0.5Fe-Si-1-550, H-0.5Fe-Si-1 and Na-0.5Fe-Si-1-S. However, for Na-0.5Fe-Si-1-LIE, significant drop of apparent surface area (267 m²/g) and micropore volume (0.08 cm³/g) was observed, indicating partial collapse of the pore structure of this sample.

Table 4.13. Chemical compositions and textural properties of Fe-silicalite-1 catalysts with different acidities.

Sample	Fe (wt. %)	<i>n</i> Na/ <i>n</i> Fe	<i>n</i> Fe/ <i>n</i> Si	<i>S</i> _{BET} ^a (m ² /g)	<i>S</i> _{ex} ^b (m ² /g)	<i>V</i> _P ^c (cm ³ /g)
0.5Fe-Si-1-550	0.45	0	0.0050	396	83	0.14
H-0.5Fe-Si-1	0.43	0	0.0045	438	95	0.15
Na-0.5Fe-Si-1-LIE	0.38	3.09	0.0043	267	73	0.08
Na-0.5Fe-Si-1-S	0.44	1.08	0.0049	396	89	0.14

^a apparent surface area, calculated by BET method. ^b apparent external surface area, calculated by t-plot method. ^c micropore volume, calculated by t-plot method.

The XRD patterns of the Fe-silicalite-1 catalysts with different acidities are illustrated in Figure 4.21. All samples showed characteristic diffraction reflexes of a typical MFI structure, indicating the successful synthesis of these samples. Furthermore, the MFI structures were largely preserved even after liquid ion exchange and further calcination. No characteristic diffraction reflexes belonging to Fe oxides could be observed from the diffractograms of all the samples.

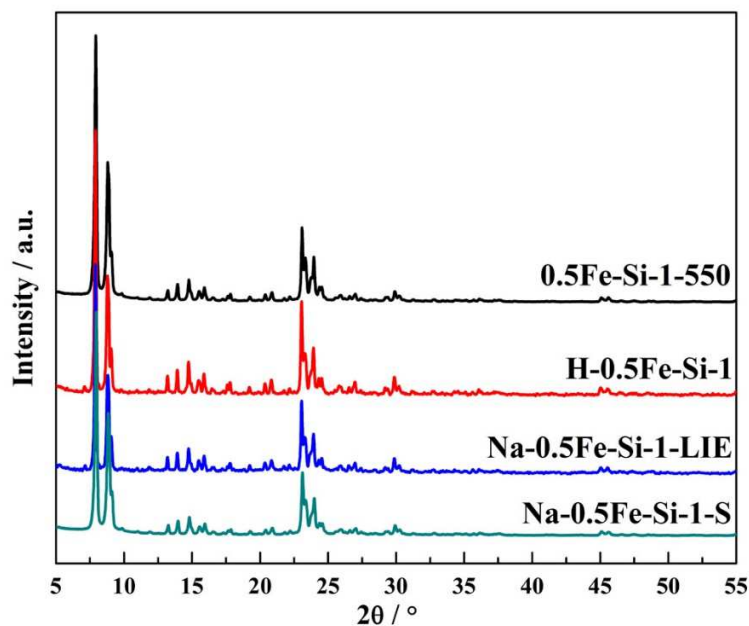


Figure 4.21. XRD patterns of different Fe-silicalite-1 catalysts with different acidities.

Figure 4.22.a-d displays TEM images of the catalysts. For 0.5Fe-Si-1-550, as already shown, sub-micrometer crystals with sizes around 370 nm were obtained. For H-0.5Fe-Si-1, the obtained crystal particles showed smooth surfaces and clear edges with sizes ranging from 370 nm to 430 nm. After further liquid ion exchange and calcination, the obtained Na-0.5Fe-Si-1-LIE showed changes of the morphology with vague edges and uneven surfaces. The crystal sizes roughly ranged from 300 nm to 420 nm. For Na-0.5Fe-Si-1-S, sub-micrometer crystals of ellipsoid-like shapes with a broad size distribution ranging from 230 nm to 440 nm (most crystal sizes around 320 nm) were obtained. These crystals exhibit relative smooth surfaces and clear edges. Although the morphology of these four catalysts showed some differences, their particle sizes were mainly in the same range.

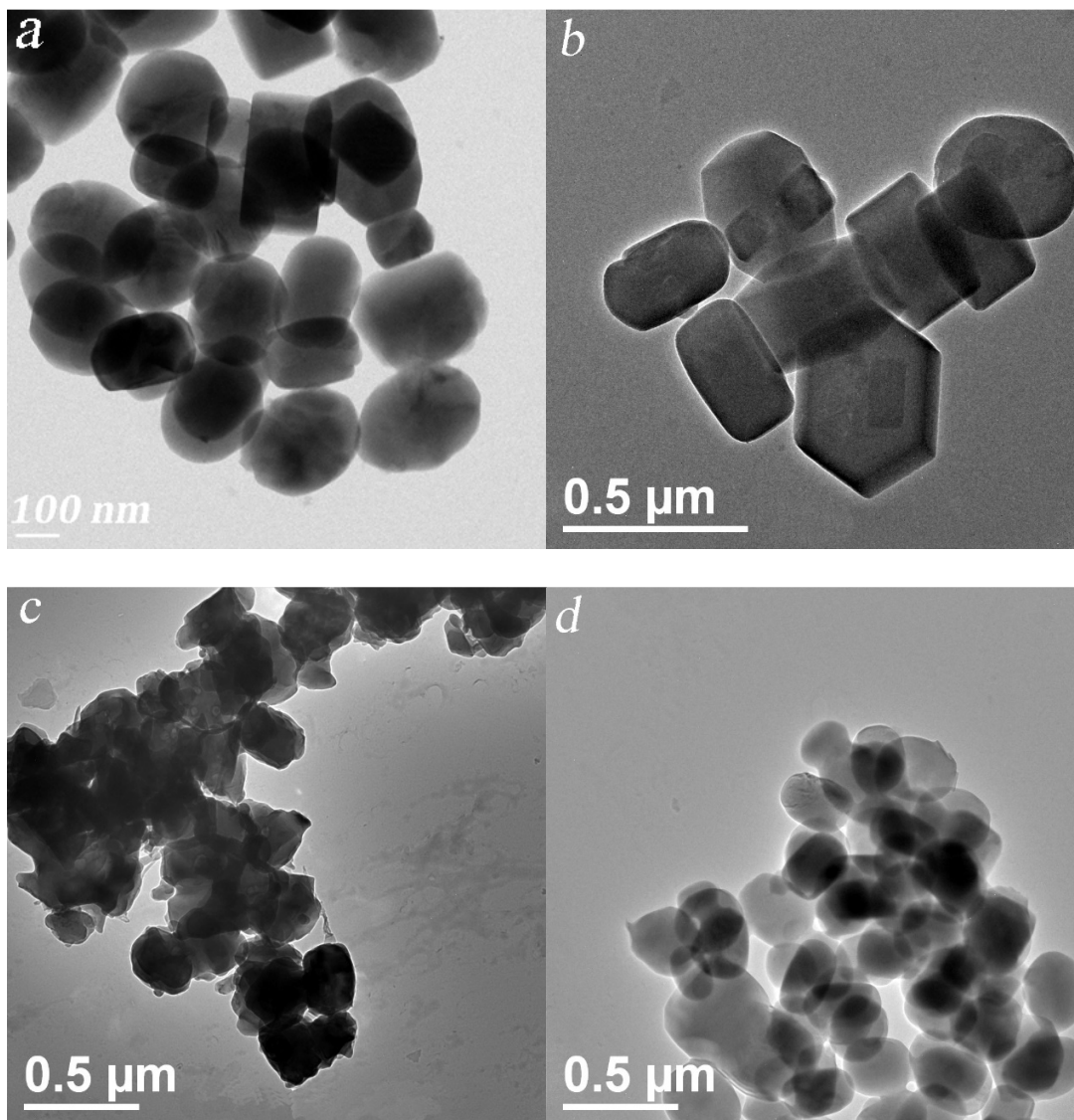


Figure 4.22. TEM images of Fe-silicalite-1 catalysts with different acidities. (a) 0.5Fe-Si-1-550, (b) H-0.5Fe-Si-1, (c) Na-0.5Fe-Si-1-LIE, (d) Na-0.5Fe-Si-1-S.

Figure 4.23 demonstrates the NH_3 -TPD profiles of the Fe-silicalite-1 catalysts with different acidities. Generally, as expected, that these four catalysts exhibit very different acidities. This is indeed the case as can be seen in Figure 4.23. For 0.5Fe-Si-1-550, a desorption peak appeared at a low temperature of 199 °C and in the high temperature range no desorption peak could be obviously observed, indicating that the cation exchange positions (Si-O-Fe) were occupied by positively charged iron species. After ion exchanged with a solution of $\text{NH}_4(\text{NO}_3)_3$ and a calcination step, an obvious peak appeared at 348 °C which can be attributed to Brønsted acid sites,

demonstrating the removal of positively charged iron species after the liquid ion-exchange and the cation exchange positions were occupied by protons exhibiting strong acidity. The peak at low temperature kept almost unchanged at 198 °C. For Na-0.5Fe-Si-1-LIE, which experienced another ion-exchange with an aqueous solution of NaNO₃ and again a calcination, the two desorption peaks merged to one peak which appeared at 254 °C with an area similar to the total desorption area of H-0.5Fe-Si-1. From Table 4.13 it can be found that a molar ratio of Na to Fe of 3.09 was obtained. After the ion exchange, the strength of the acidity significantly decreased but the amount of acid sites kept nearly unchanged, indicating that Brønsted acid sites were occupied by Na species. For Na-0.5Fe-Si-1-S, a much smaller peak could be observed at 204 °C with a tiny and broad shoulder peak at 294 °C, indicating a weak acidity of this sample and most of the Brønsted acid sites were occupied by initially added Na species.

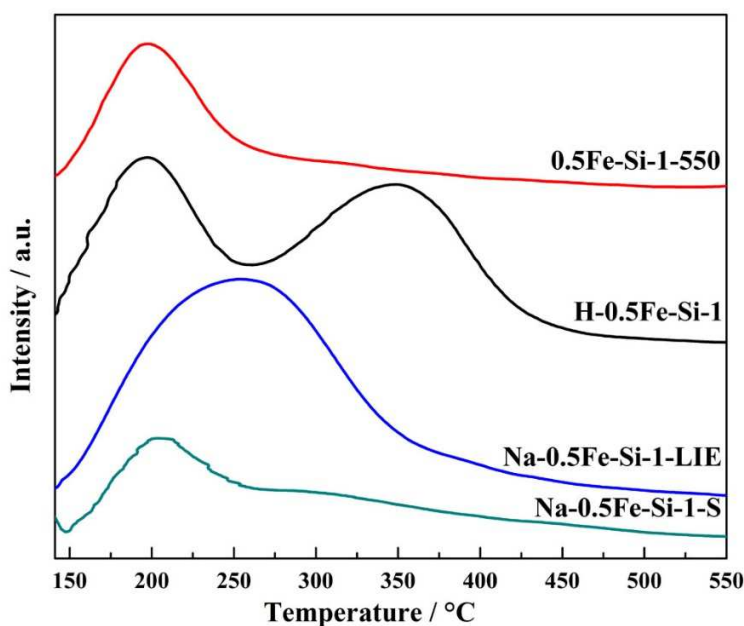


Figure 4.23. NH₃-TPD profiles of Fe-silicalite-1 catalysts with different acidities.

4.4.4 Catalytic results and discussion

Table 4.14 shows the catalytic results related to CH₄ for the Fe-silicalite-1 catalysts with different acidities. For 0.5Fe-Si-1-550, with positively charged iron species occupying the cation exchange positions, the conversion of methane was 17.1 % with a hydrocarbon oxygenates (MeOH, FD and FA) selectivity of 98.8 %. Especially, a highest FA selectivity of 72.4 % with a lowest CO₂ selectivity of 3.4 % was obtained. The TOF and volumetric productivity were 210 h⁻¹ and 2.5×10⁻

$6 \text{ mol}\cdot\text{ml}^{-1}\text{s}^{-1}$, respectively. For H-0.5Fe-Si-1, over which the positively charged iron species were removed by liquid ion exchange and possesses the strongest acid sites, the conversion of methane was 17.4 % and the selectivity of hydrocarbon oxygenates decreased to 95.7 %. Especially, a lowest FA selectivity of 55.7 % with a highest CO_2 selectivity of 6.4 % was obtained over this catalyst. The TOF and volumetric productivity increased a little bit to 228 h^{-1} and $2.6\times 10^{-6} \text{ mol}\cdot\text{ml}^{-1}\text{s}^{-1}$, respectively. When sodium ions occupied the cation exchange positions and the strength of acidity decreased, the conversion of methane dropped a little to 15.2 % and the selectivity of hydrocarbon oxygenates increased to 99.3 % over Na-0.5Fe-Si-1-LIE. The selectivity of CO_2 dropped to 5.9 %. The TOF increased a little to 237 h^{-1} with a little drop of the volumetric productivity to $2.5\times 10^{-6} \text{ mol}\cdot\text{ml}^{-1}\text{s}^{-1}$. For Na-0.5Fe-Si-1-S, when the acidity was further decreased by occupying Brønsted acid sites with initially added Na species, the conversion of methane increased slightly to 16.2 % and the selectivity of hydrocarbon oxygenates dropped to 96.8 %. Especially, the FA selectivity increased to 62.5 % and the CO_2 selectivity dropped to 4.8 %. The TOF decreased to 210 h^{-1} and the value of volumetric productivity was unchanged ($2.5\times 10^{-6} \text{ mol}\cdot\text{ml}^{-1}\text{s}^{-1}$).

Table 4.14. Catalytic results related to CH_4 for Fe-silicalite-1 catalysts with different acidities.

Catalyst	CH_4 conversion %	Selectivity %					TOF h^{-1}	Volume Prod $\text{mol}\cdot\text{ml}^{-1}\text{s}^{-1}$
		MeOH	FD	FA	CO_2	Sum		
0.5Fe-Si-1-550	17.1	4.0	22.4	72.4	3.4	102.2	210	2.5×10^{-6}
H-0.5Fe-Si-1	17.4	4.7	35.2	55.7	6.4	102.1	228	2.6×10^{-6}
Na-0.5Fe-Si-1-LIE	15.2	2.6	39.2	57.6	5.9	105.2	237	2.5×10^{-6}
Na-0.5Fe-Si-1-S	16.2	7.6	26.7	62.5	4.8	101.6	210	2.5×10^{-6}

Reaction conditions: 0.1 g catalysts; reaction temperature: $100 \text{ }^\circ\text{C}$; pressure: 40 bar; gas flow: 4 ml/min N_2 and 4 ml/min CH_4 ; liquid flow: 1.5 ml/min of 0.12 M aqueous H_2O_2 solution.

Table 4.15 demonstrates the catalytic results related to H_2O_2 for Fe-silicalite-1 catalysts with different acidities. For 0.5Fe-Si-1-550, it is interesting to notice that the lowest H_2O_2 conversion of 60.5 % and the lowest O_2 selectivity of 33.8 %, together with the highest selectivity of hydrocarbon oxygenates (69.1 %) and the lowest CO_2 selectivity (3.6 %) were observed, indicating a highest level of H_2O_2 utilization and a lowest level of over-oxidation over this catalyst. For H-0.5Fe-Si-1, the conversion of H_2O_2 significantly increased to 83.6 %, which was the highest conversion of H_2O_2 among all these values. The highest O_2 selectivity (58.7 %) and CO_2 selectivity

(5.3 %) together with a nearly lowest hydrocarbon oxygenates selectivity of 49.0 % were obtained. These results revealed a lowest level of H₂O₂ utilization and a highest level of over-oxidation over the catalyst that possesses the strongest acid sites. With decreased strength of acidity, decreased values of H₂O₂ conversion of 72.1 %, O₂ selectivity of 40.9 % and CO₂ selectivity of 4.9 % could be found over Na-0.5Fe-Si-1-LIE. The hydrocarbon oxygenates selectivity increased to 53.1 %. For Na-0.5Fe-Si-1-S, the conversion of H₂O₂ increased to 82.2 % together with considerable increasing of O₂ selectivity to 52.4 %. The selectivity of hydrocarbon oxygenates decreased to 48.1 % with a CO₂ selectivity of 3.7 % was obtained.

Table 4.15. Catalytic results related to H₂O₂ for Fe-silicalite-1 catalysts with different acidities.

Catalyst	H ₂ O ₂ conversion %	Selectivity %			
		O ₂	Hydrocarbon oxygenates	CO ₂	Sum
0.5Fe-Si-1-550	60.5	33.8	69.1	3.6	106.5
H-0.5Fe-Si-1	83.6	58.7	49.0	5.3	112.9
Na-0.5Fe-Si-1-LIE	72.1	40.9	53.1	4.9	98.9
Na-0.5Fe-Si-1-S	82.2	52.4	48.1	3.7	104.2

Reaction conditions: 0.1 g catalysts; reaction temperature: 100 °C; pressure: 40 bar; gas flow: 4 ml/min N₂ and 4 ml/min CH₄; liquid flow: 1.5 ml/min of 0.12 M aqueous H₂O₂ solution.

For these four investigated catalysts, NH₃-TPD results showed that they exhibited very different acidity, either the strength or the amount of acid sites. Similar values of methane conversion were obtained. Catalyst (0.5Fe-Si-1-550) with positively charged iron species occupying the cation exchange positions showed the highest selectivity towards hydrocarbon oxygenates, the lowest CO₂ selectivity and the most efficient H₂O₂ utilization level. On the contrary, after the removing of the positively charged iron species with protons occupying the cation exchange positions, the catalyst (H-0.5Fe-Si-1) showed nearly the lowest hydrocarbon oxygenates selectivity, together with the highest CO₂ selectivity and the lowest H₂O₂ utilization level. One may conclude that the positively charged iron species play an important role for the selective oxidation of methane and Brønsted acid sites do not exhibit a promoter effect for the activation of methane, in contrast, they enhance unselective reactions (leading to over-oxidation) and the decomposition of H₂O₂ under given conditions.

4.4.5 Summary

Four Fe-silicalite-1 catalysts with typical MFI structure were successfully synthesized. These catalysts showed very similar Fe contents and their particle sizes were mainly in the same range. NH₃-TPD results revealed that they possessed very different acidities. Catalytic results indicated that the positively charged iron species play an important role for the selective oxidation of methane. Brønsted acid sites do not play a role as a critical promoter for the activation of methane, in contrast, they enhance the decomposition of H₂O₂ and unselective reactions leading to over-oxidation of methane under given conditions.

5 Selective oxidation of methane over post-synthetically Fe-loaded MFI zeolites

5.1 Introduction

Post-synthetic methods are widely used for dispersing Fe species inside the zeolite channels to obtain Fe-containing MFI zeolites. It is reported that Fe-containing MFI zeolites prepared by different kinds of post-synthetic methods such as solid state ion exchange (SSIE) and liquid ion exchange (LIE) showed noticeable catalytic performance for the selective oxidation of methane, selective catalytic reduction of NO_x, and hydroxylation of benzene to phenol [109, 112, 113, 126]. As described in section 1.4.2, based on the reaction of the acetylacetonate metal complex with the surface hydroxyls of the support materials, the molecular designed dispersion (MDD) method was developed in order to deposit highly dispersed layers of metal oxides without the formation of crystals [127-129]. Thus, the MDD method was applied to obtain highly dispersed Fe species in the supports of H-ZSM-5 and silicalite-1 using Fe(acac)₃ or Fe(acac)₂ as the precursor of Fe.

In this chapter, first of all, sub-micrometer sized crystals of iron free H-ZSM-5 and silicalite-1 were hydrothermally synthesized. Then, different post-synthetic methods such as SSIE, LIE and MDD methods were applied to prepare Fe-loaded MFI zeolites with a similar Fe content to compare the effect of different post-synthetic methods of Fe loading on the activity and selectivity for the oxidation of methane. The optimized reaction conditions described in chapter 3, namely a relative low concentration of aqueous H₂O₂ solution (0.12 M) and a relative high flow rate (1.5 ml/min) at 100 °C, were used in the investigations of this chapter. The physicochemical properties of the catalysts were characterized by XRD, ICP-OES, low-temperature N₂ adsorption-desorption, H₂-TPR, NH₃-TPD, TEM and UV-Vis-DR techniques.

5.2 Catalysts and characterization results

5.2.1 Catalysts

Sub-micrometer sized crystals of H-ZSM-5 and silicalite-1 were hydrothermally synthesized according to sections 2.2.4 and 2.2.1. The obtained template free H-ZSM-5 and silicalite-1 zeolites are denoted as H-ZSM-5 and Si-1, respectively. For comparison, commercial NH₄-ZSM-5 zeolite obtained from Zeolyst was calcined at 550 °C for 3 h to get the H-form. This sample is denoted as H-ZSM-5-C. Based on the self-synthesized MFI zeolites, H-ZSM-5 and silicalite-1, Fe was loaded

via different post-synthetic methods and different Fe precursor were used. The SSIE sample (description can be found in section 2.2.5) based on the self-synthesized H-ZSM-5 is denoted as H/Fe(III)-ZSM-5-SSIE. For comparison, Si-1 was also used as support for SSIE and the prepared sample is denoted as Fe(III)-Si-1-SSIE. The MDD method is described in section 2.2.7 and Fe-loaded MFI samples using MDD are denoted as H/Fe(III)-ZSM-5-MDD, H/Fe(II)-ZSM-5-MDD and Fe(III)-Si-1-MDD. The Roman numerals in the brackets indicate the valence of iron in the original Fe precursors (not in the final catalysts, since calcination will change the oxidation state of Fe). LIE method was also used and the Fe-loaded MFI sample is denoted as H/Fe(II)-ZSM-5-LIE. The detailed procedure of LIE is described in section 2.2.6.

5.2.2 Characterization results

Table 5.1 shows the chemical compositions and textual properties of the post-synthetically Fe-loaded MFI catalysts. For the commercial zeolite H-ZSM-5-C, an impurity of Fe with a content of 175 ppm was detected by ICP-OES. For the self-synthesized zeolites H-ZSM-5 and Si-1, the contents of Fe were below the detection limit (10 ppm). For the self-synthesized and Fe loaded MFI catalysts, similar Fe contents of around 0.40 wt. % were obtained, except for the H/Fe(II)-ZSM-5-MDD having a Fe content of 0.62 wt. %. Since Fe(acac)₂ was used as the Fe precursor, which has a smaller molecular size than Fe(acac)₃, more positions on the surface of the support can be occupied and thus a higher Fe content is reached. Compared to the commercial H-ZSM-5-C whose apparent surface areas and apparent external surface areas were 383 m²/g and 30 m²/g, respectively, both self-synthesized MFI zeolites, namely H-ZSM-5 and Si-1, showed higher apparent surface areas (461 m²/g and 451 m²/g) and higher apparent external surface areas (103 m²/g and 69 m²/g). For Fe(III)-Si-1-MDD and Fe(III)-Si-1-SSIE, the apparent surface areas dropped to 384 m²/g and 397 m²/g with increased apparent external surface areas of 120 m²/g and 83 m²/g. The micropore volume dropped to 0.11 cm³/g and 0.14 cm³/g, respectively. When compared to Fe(III)-Si-1-SSIE, Fe(III)-Si-1-MDD exhibits a much larger increase of the apparent external surface area and a much larger drop of the micropore volume. The reason can be explained as follows. In the MDD method, the probability of loading the Fe species on the external surface of the support is higher than for the SSIE since the precursor Fe(acac)₃ is a bulky complex and interacts more strongly with the outer surface than FeCl₃. This leads to more Fe oxide species distributed at the external surface after calcination for the MDD method compared to the SSIE. These Fe oxide species distributed at the external surface can block the pore mouths and coarsen

the outer surface. For Fe loaded catalysts based on self-synthesized H-ZSM-5, it is interesting that H/Fe(II)-ZSM-5-LIE showed no decrease of the apparent surface area and micropore volume, revealing a high Fe dispersion inside the micropores and less blocking of micropores in this catalyst. For H/Fe(III)-ZSM-5-MDD, only a small drop of the apparent surface area and micropore volume to 433 m²/g and 0.14 cm³/g could be observed. The apparent surface areas further dropped to 425 m²/g and 406 m²/g with both having a little bit lower micropore volume of 0.12 cm³/g for H/Fe(II)-ZSM-5-MDD and H/Fe(III)-ZSM-5-SSIE, respectively, indicating partially blocked micropores by large Fe oxide clusters.

Table 5.1. Chemical compositions and textural properties of the post-synthetically Fe-loaded MFI catalysts.

Sample	Fe (wt. %)	$n\text{Fe}/n\text{Al}$	$n\text{Fe}/n\text{Si}$	$S_{\text{BET}}^{\text{a}}$ (m ² /g)	S_{ex}^{b} (m ² /g)	V_{P}^{c} (cm ³ /g)
H-ZSM-5-C	175 ppm	-	-	383	30	0.15
H-ZSM-5	< 10 ppm	-	-	461	103	0.15
Si-1	< 10 ppm	-	-	451	69	0.17
H/Fe(III)-ZSM-5-SSIE	0.39	0.12	0.0043	406	121	0.12
Fe(III)-Si-1-SSIE	0.40	-	0.0041	397	83	0.14
H/Fe(III)-ZSM-5-MDD	0.38	0.13	0.0045	433	117	0.14
H/Fe(II)-ZSM-5-MDD	0.62	0.20	0.0072	425	131	0.12
Fe(III)-Si-1-MDD	0.43	-	0.0047	384	120	0.11
H/Fe(II)-ZSM-5-LIE	0.39	0.14	0.0045	464	120	0.15

^a apparent surface area, calculated by BET method. ^b apparent external surface area, calculated by t-plot method. ^c micropore volume, calculated by t-plot method.

The XRD patterns of the post-synthetically Fe-loaded MFI catalysts based on the self-synthesized ZSM-5 and silicalite-1 are illustrated in [Figure 5.1](#). Their powder XRD patterns agree very well with that of a typical MFI structure, revealing that the catalysts were successfully synthesized and the MFI structure was largely maintained despite the post-synthetic modification with Fe *via* different methods and the final calcination under high temperatures. No characteristic diffraction reflexes belonging to Fe oxides could be obviously observed from the diffractograms of all catalysts, revealing that the Fe oxide species are highly dispersed or they are below the detection limit of the XRD due to low Fe contents. Thus, H₂-TPR experiments and UV-Vis-DR were performed to obtain more information about the Fe oxide species of the MFI catalysts.

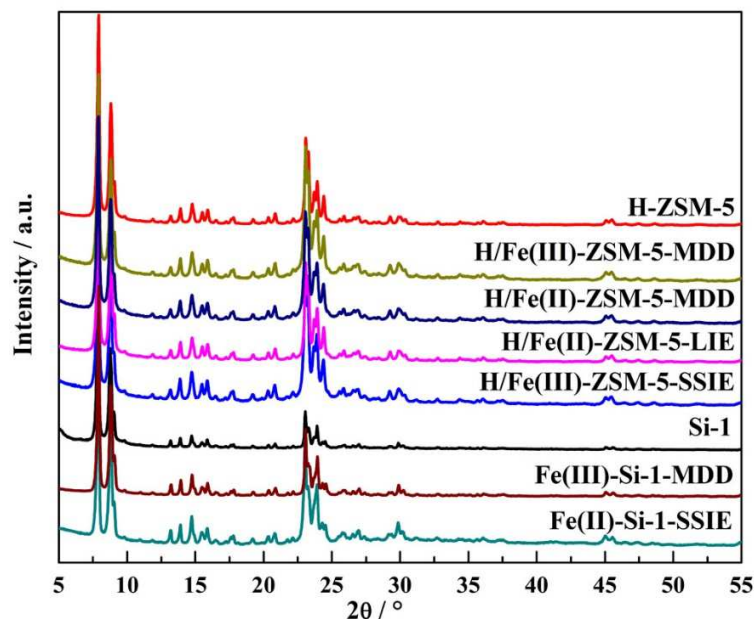


Figure 5.1. XRD patterns of the post-synthetically Fe-loaded MFI catalysts.

TEM images of self-synthesized H-ZSM-5 and Si-1 are shown in Figure 5.2. For H-ZSM-5, crystals with a typical coffin-like morphology could be observed. The sizes of sub-micrometer crystals were around 175 nm. The TEM images are consistent with those described in literature [132]. For Si-1, small ellipsoidal crystals with clear edges were obtained. These crystals owned a relative uniform size distribution in the range of 300-350 nm. These sub-micrometer sized crystals can help to intensify internal mass transport of the reaction.

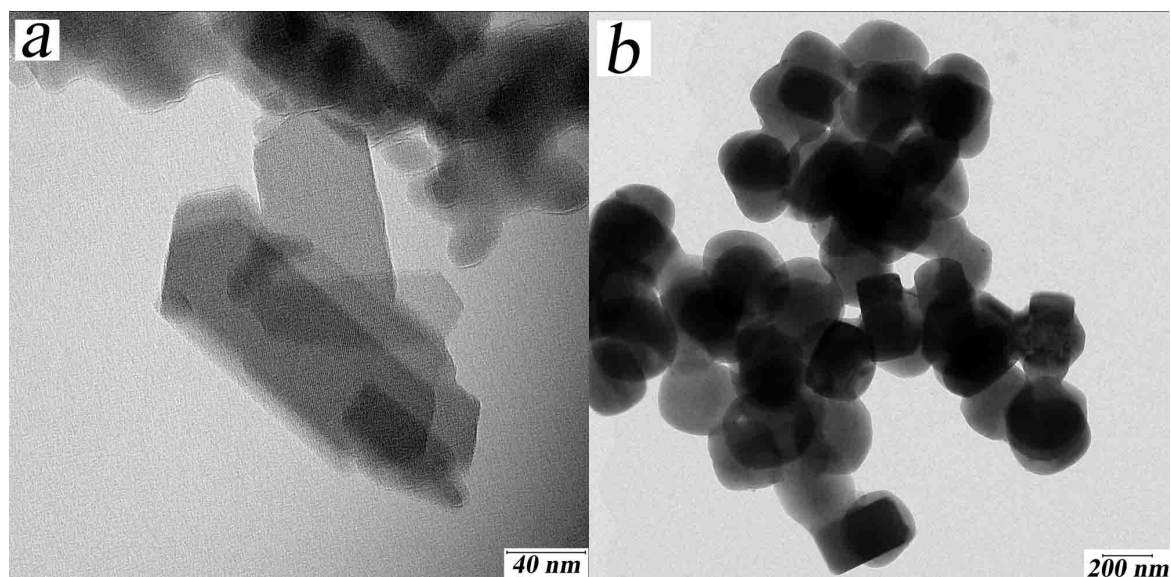


Figure 5.2. TEM images of H-ZSM-5 (a) and Si-1 (b)

Figure 5.3 shows the NH₃-TPD profiles of post-synthetically Fe-loaded MFI catalysts. As expected, no acidity could be detected on Si-1, and Si-1 based catalysts such as Fe(III)-Si-1-MDD and Fe(III)-Si-1-SSIE. Two obvious NH₃ desorption peaks appeared at 212 °C and 423 °C for the parent H-ZSM-5 zeolite. The peak at 423 °C is attributed to NH₃ strongly adsorbed on Brønsted acid sites [141], while the assignment of the peak at 212 °C is somewhat controversial. It has been attributed to the desorption peak of weakly physisorbed NH₃ on Lewis acid sites [141] or weakly adsorbed NH₃ on Brønsted acid sites [142, 143]. After the loading of Fe *via* different post-synthetic methods, the temperature of the peak belonging to strong Brønsted acid sites slightly dropped and, particularly, the area of the peak obviously decreased. These observations may be due to two reasons. One reason is that the Brønsted acid protons of H-ZSM-5 were partially substituted by positively charged Fe species after the loading of Fe. Another reason may be, that the mouths of the micro pores of H-ZSM-5 were partially blocked by Fe oxide species thus hindering the diffusion of ammonia into the pores and causing a lower ammonia loading. The latter explanation would be consistent with the drop of both the apparent surface area as well as the micropore volume (Table 5.1), especially for the H/Fe(II)-ZSM-5-MDD.

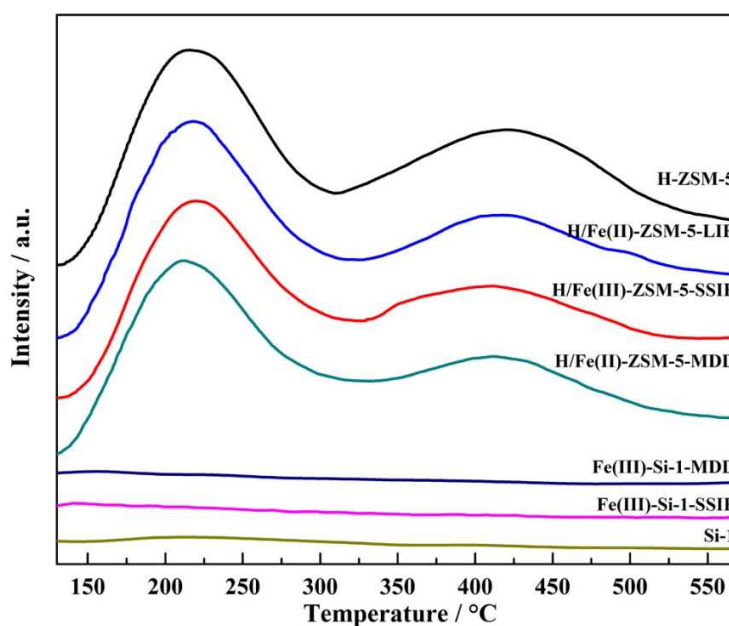


Figure 5.3. NH₃-TPD profiles of the post-synthetically Fe-loaded MFI catalysts.

Figure 5.4 demonstrates the conducted H₂-TPR experiments for all the post-synthetically Fe-loaded MFI catalysts. Table 5.2 summarize the consumption of hydrogen for the temperature range of 200-800 °C during the H₂-TPR experiments for the catalysts. Very different reduction curves

were observed for the Fe-loaded MFI catalysts prepared by different post-synthetic methods. It is clear that all materials feature multiple Fe oxide species on their surface, although some samples have a broader distribution of different Fe-species than others do. For Fe(III)-Si-1-SSIE, an obvious reduction peak could be found at 495 °C with another higher temperature peak at 665 °C. The H₂/Fe ratio was 1.33 (see Table 5.2) which was close to 1.5, indicating that a significant fraction of Fe is present as large Fe oxide aggregates which is easily reduced to metallic Fe [114] and not detected in XRD. Similarly, an obvious peak at 460 °C with a shoulder peak at 370 °C and a tiny peak at 560 °C with a total H₂/Fe ratio of 1.35 was obtained for H/Fe(II)-ZSM-5-MDD, suggesting the predominant presence of Fe oxide aggregates (not detected in XRD) of this sample. For H/Fe(III)-ZSM-5-SSIE, a peak appeared at 475 °C with two shoulder peaks at 390 °C and 570 °C. The H₂/Fe ratio was also relative high with a value of 1.21, which also demonstrates a large amount of easily reducible iron oxide species but with a smaller ratio compared to Fe(III)-Si-1-SSIE. For H/Fe(III)-ZSM-5-MDD, a small and broad reduction peak could be found with the maximum at 400 °C and two shoulder peaks appearing at 320 °C and 480 °C, indicating a broad distribution of different Fe species. The H₂/Fe ratio was 0.50, which might be due to the reduction of a mixture of mononuclear Fe oxide species and α -Fe₂O₃ species according to Nam and co-workers [116]. The Fe(III)-Si-1-MDD also exhibited a small and broad reduction peak but observed at higher temperatures of 555 °C with two shoulder peaks at 405 °C and 635 °C, respectively. Also a low value of the H₂/Fe ratio of 0.65 was obtained, revealing that most of the Fe species were very well dispersed and mostly existed as mononuclear Fe oxide species which are very difficult to reduce to metallic Fe. This assumption was consistent with the observation reported in literature for Fe/SiO₂ samples, in which some iron ions have strong interaction with the silica support forming very small iron oxide species that are very stable against reduction to metallic Fe during H₂ reduction [146]. According to the investigations of Moulijn and co-workers, the reduction kinetics of iron oxides are also influenced by particle size, morphology, defect density, etc. [147]. A tiny and very broad peak with two maxima detected at 405 °C and 505 °C and a very small H₂/Fe ratio of 0.33 were obtained for H/Fe(II)-ZSM-5-LIE. These observations revealed that a considerable amount of highly dispersed mononuclear Fe oxide species that are difficult to reduce existed in this catalyst, leading to tiny and very broad reaction peaks. This was also consistent with the low-temperature N₂ adsorption-desorption result that indicates a high Fe dispersion inside the micropores and less blocking of micropores in this catalyst.

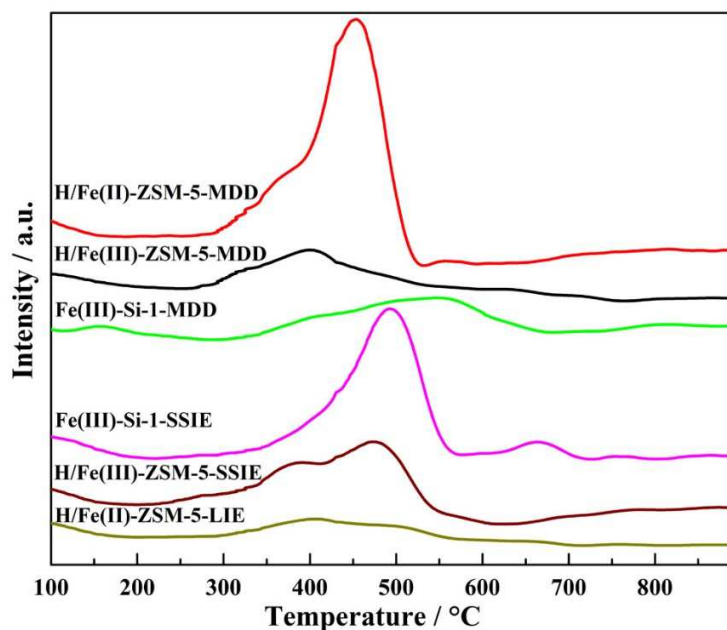


Figure 5.4. H₂-TPR profiles of the post-synthetically Fe-loaded MFI catalysts.

Table 5.2. Hydrogen consumption during the H₂-TPR experiments of the temperature range of 200-800°C for the post-synthetically Fe-loaded MFI catalysts.

Sample	$n_{\text{Fe}}/n_{\text{Al}}$	H ₂ /Fe consumption (mol/mol)
H/Fe(III)-ZSM-5-MDD	0.13	0.50
H/Fe(II)-ZSM-5-MDD	0.20	1.35
Fe(III)-Si-1-MDD	-	0.65
H/Fe(III)-ZSM-5-SSIE	0.12	1.21
Fe(III)-Si-1-SSIE	-	1.33
H/Fe(II)-ZSM-5-LIE	0.14	0.33

The UV-Vis-DR spectra of the post-synthetically Fe-loaded MFI catalysts investigated in this work are presented in [Figure 5.5.a-h](#). The spectra differ strongly revealing a broad distribution of different Fe species present. This may be represented by sub-bands, as illustrated in the figures and the relative numerical contributions are demonstrated in [Table 5.3](#). It was proposed that bands below 300 nm reveal isolated Fe ions in tetrahedral and octahedral coordinations [112, 119, 148]. Signals between 300 and 400 nm were assigned to oligomeric Fe oxo entities, and bands above 400 nm were attributed to Fe oxide aggregates, which may be highly disordered [112]. However,

it was also recently suggested that signals below 300 nm also may arise from binuclear Fe oxo clusters provided that the oxo bridge between the Fe ions is hydroxylated [149].

No absorption bands could be obviously detected on the parent Si-1 and H-ZSM-5 zeolites. For all the Fe loaded catalysts, a significant absorption was observed below 300 nm with a relative contribution ranging from 44.8 % to 56.1 % (Table 5.3), suggesting considerable amounts of mononuclear Fe species existed in all these catalysts. For Fe(III)-Si-1-MDD, all the sub-bands were below 400 nm with a superior sub-band peak present at 235 nm, revealing most Fe existed as isolated Fe species and small oligomeric Fe oxo clusters. This observation is consistent with the TPR experiment showing a very small and broad reduction peak. According to Nam and co-workers [116], broad peaks appearing at ca. 360 nm and 550 nm in UV-Vis spectra of Fe-ZSM-5 catalysts are mainly due to the d-d transitions of Fe^{3+} ions similar to those of Fe_2O_3 . For Fe(III)-Si-1-SSIE, one sub-band could be found at around 385 nm which was very close to 400 nm and may be attributed to larger oligomeric Fe species similar to Fe_2O_3 . In addition, a sub-band appeared at around 515 nm, indicating larger Fe oxide aggregates in the sample, which however are still too small to be detected by XRD. These large oligomeric Fe species and Fe oxide aggregates would lead to an obvious reduction peak, which was confirmed by the H_2 -TPR experiments. For H/Fe(II)-ZSM-5-MDD, sub-bands appeared at around 253 nm, 378 nm and 480 nm. The last one can be attributed to larger Fe oxide aggregates. For H/Fe(III)-ZSM-5-MDD, sub-bands could be observed at around 247 nm, 368 nm and 414 nm. Moreover, there was a comparable larger contribution of the larger aggregates (increase in I_3 , Table 5.3). When compared with H/Fe(II)-ZSM-5-MDD, all peaks shifted to lower wavelengths which corresponds to Fe species which are more difficult to reduce confirmed by the H_2 -TPR curves. H/Fe(III)-ZSM-5-SSIE and H/Fe(II)-ZSM-5-LIE showed similar spectra but the sub-bands differed a lot. Sub-bands appeared at around 255 nm, 367 nm and 432 nm for H/Fe(II)-ZSM-5-LIE, while for H/Fe(III)-ZSM-5-SSIE they were found at 256 nm, 382 nm and 460 nm, i.e. a red shift could be observed. Moreover, their relative contribution changed to a certain extent, generating more I_2 and slightly more I_1 type species at the expense of I_3 species in the H/Fe(III)-ZSM-5-SSIE. According to Brückner and co-workers [150], in Fe-ZSM-5 catalysts, evidently different redox behavior of Fe_xO_y clusters and particles exist and the redox properties of isolated Fe^{3+} sites might change when they coexist with Fe_xO_y clusters in the same sample. In H/Fe(III)-ZSM-5-SSIE, Fe_xO_y clusters may be mainly located on the outer surface of the H-ZSM-5 crystals and block the mouth of the pores thus leading to a significant decrease of

the apparent surface area and the micro pore volume (Table 5.1). Fe_xO_y clusters may be much smaller for H/Fe(II)-ZSM-5-LIE and mainly located in the pores of the ZSM-5-S as no drop of the surface area and the micro pore volume could be observed (Table 5.1). The difference of the Fe_xO_y species in H/Fe(II)-ZSM-5-LIE and H/Fe(III)-ZSM-5-SSIE could also be confirmed by the H_2 -TPR experiments as the reduction peaks could be more obviously observed for H/Fe(III)-ZSM-5-SSIE. However, the detailed structure of these different Fe_xO_y species is still unknown in this work.

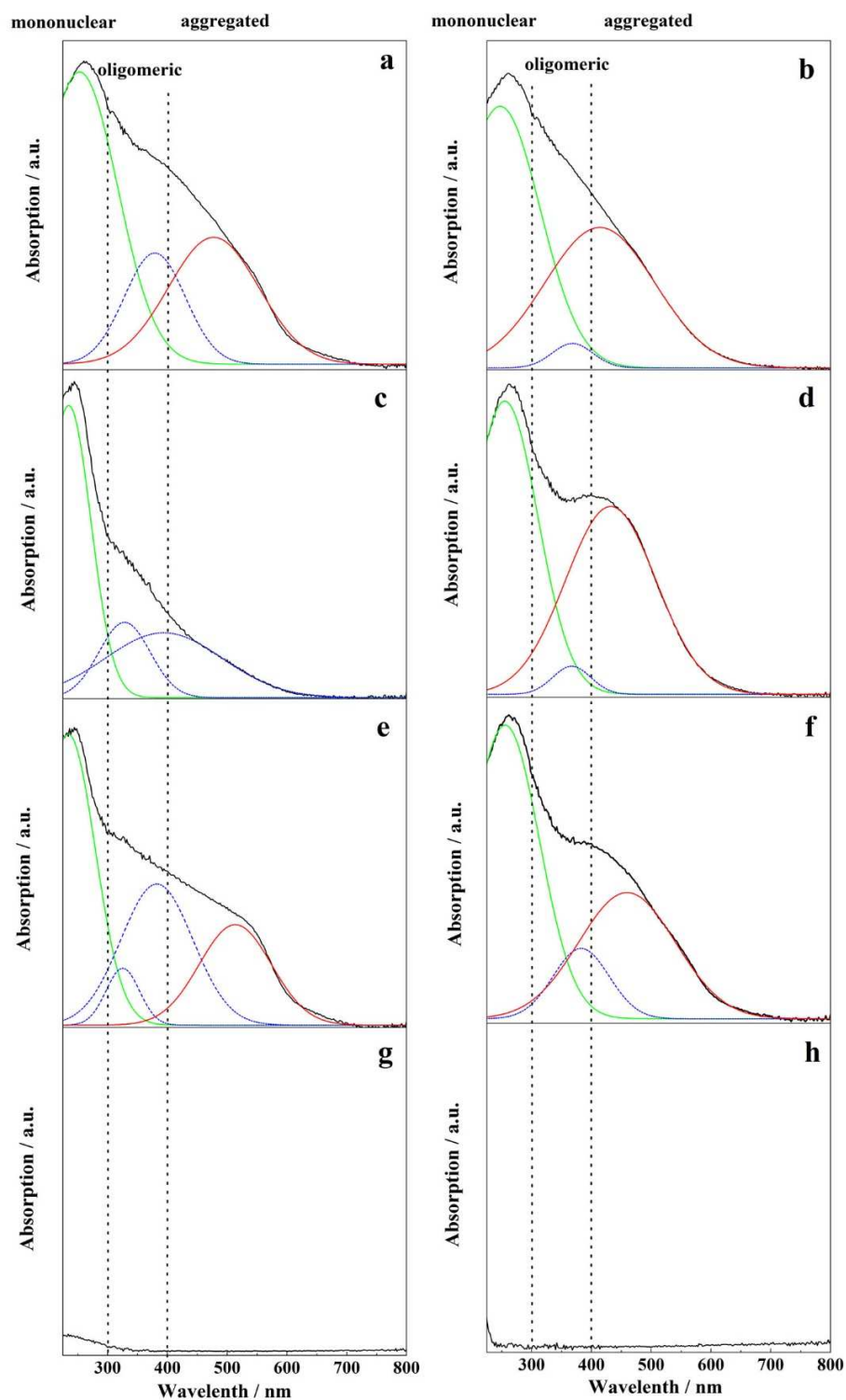


Figure 5.5. UV-Vis-DR spectra of the post-synthetically Fe-loaded MFI catalysts. (a) H/Fe(II)-ZSM-5-MDD, (b) H/Fe(III)-ZSM-5-MDD, (c) Fe(III)-Si-1-MDD, (d) H/Fe(II)-ZSM-5-LIE, (e) Fe(III)-Si-1-SSIE, (f) H/Fe(III)-ZSM-5-SSIE, (g) Si-1, (h) H-ZSM-5. Deconvolution of the spectra into sub-bands was performed according to Gauss function to show the relative contribution of these sub-bands.

Table 5.3. Relative numerical analysis of UV-Vis-DR spectra of post-synthetically Fe-loaded MFI catalysts in Figure 5.5. Percentage of the sub-bands due to the relative contribution of different range of wavelength.

Catalyst	I_1 (%)	I_2 (%)	I_3 (%)
	$\lambda < 300$ nm	$300 < \lambda < 400$ nm	$\lambda > 400$ nm
Fe(III)-Si-1-SSIE	44.8	34.5	20.7
H/Fe(III)-ZSM-5-SSIE	55.5	10.8	33.6
H/Fe(II)-ZSM-5-LIE	51.7	2.9	45.4
H/Fe(II)-ZSM-5-MDD	55.0	16.7	28.3
H/Fe(III)-ZSM-5-MDD	56.1	2.7	41.2
Fe(III)-Si-1-MDD	53.0	47.0	-

5.3 Catalytic results and discussion

In all catalytic measurements, CO₂ and O₂ were the main gaseous products whereas formic acid (FA) and formaldehyde (FD) were the main liquid products. In some cases trace amounts methanol (MeOH) less than 0.01% were detected, which were neglected and the value was set to 0. The only exception regarding to the formation of methanol was H/Fe(II)-ZSM-5-LIE with which a selectivity of 3.0 % for methanol was obtained.

Table 5.4 summarizes the catalytic results related to CH₄ for the post-synthetically Fe-loaded MFI catalysts. A considerable methane conversion of 6.5 % with a high TOF of 2411 h⁻¹ and a very high FA selectivity of 97.5 % was obtained over the commercial H-ZSM-5-C having trace impurities of 175 ppm Fe (Table 5.1). For the self-synthesized MFI zeolites H-ZSM-5 and Si-1 with Fe impurities below 10 ppm (Table 5.1), no activity could be obtained. Also for the two catalysts based on silicalite-1, Fe(III)-Si-1-SSIE and Fe(III)-Si-1-MDD, no conversion of methane could be obviously observed, indicating that they do not bear catalytically active Fe sites even though these two catalysts contained considerable content of Fe (around 0.4 wt. %, see Table 5.1). Over H/Fe(III)-ZSM-5-SSIE, a methane conversion of 18.3 % with a selectivity of 24.4 % towards FD and a selectivity of 62.6 % towards FA were observed. The selectivity of CO₂ was 15.1 %, revealing a high over-oxidation level of methane. The TOF and volumetric productivity were 255 h⁻¹ and 2.7×10⁻⁶ mol•ml⁻¹s⁻¹, respectively. For the Fe-loaded catalysts based on the self-synthesized H-ZSM-5 prepared by the MDD method, the methane conversion increased from 18.1 % with H/Fe(III)-ZSM-5-MDD to 19.1 % with H/Fe(II)-ZSM-5-MDD. Also the selectivities to FA

increased from 67.2 % to 73.3 %, while the selectivities to CO₂ decreased considerably from 16.4 % to 9.8 %, indicating that the over-oxidation level of FA could be decreased to some extent with H/Fe(II)-ZSM-5-MDD. Surprisingly, a lower TOF value of 190 h⁻¹ was obtained for H/Fe(II)-ZSM-5-MDD compared to that of 287 h⁻¹ for H/Fe(III)-ZSM-5-MDD, which is due to a much higher Fe content of H/Fe(II)-ZSM-5-MDD (see Table 5.1) compared to H/Fe(III)-ZSM-5-MDD. As expected, the volumetric productivity over H/Fe(II)-ZSM-5-MDD was higher, with 3.2×10⁻⁶ mol•ml⁻¹s⁻¹ compared to a value of 3.0×10⁻⁶ mol•ml⁻¹s⁻¹ for H/Fe(III)-ZSM-5-MDD. For H/Fe(II)-ZSM-5-LIE, the conversion of methane considerably increased to 23.5 % with a FD selectivity of 22.7 % and a FA selectivity of 64.9 %. This was the only catalyst with which a small but significant amount of methanol was obtained corresponding to a selectivity of 3.0 %. The selectivity of CO₂ was 10.6 %, revealing a relative low over-oxidation level despite the high methane conversion of 23.5 %. Compared to other post-synthetically Fe-loaded MFI catalysts, the highest TOF of 303 h⁻¹ together with a relative high volumetric productivity of 3.1×10⁻⁶ mol•ml⁻¹s⁻¹ was observed.

Table 5.4. Catalytic results related to CH₄ for different post-synthetically Fe-loaded MFI catalysts.

Catalyst	CH ₄ conversion %	Selectivity %					TOF h ⁻¹	Volume Prod mol•ml ⁻¹ s ⁻¹
		MeOH	FD	FA	CO ₂	Sum		
H-ZSM-5-C	6.5	0	0	98.5	2.5	101.0	2411	1.1×10 ⁻⁶
H-ZSM-5	0.1	0	0	0	0	0	0	0
Si-1	0.1	0	0	0	0	0	0	0
H/Fe(III)-ZSM-5-SSIE	18.3	0	24.4	62.6	15.1	102.1	255	2.7×10 ⁻⁶
Fe(III)-Si-1-SSIE	0.0	0	0	0	0	0	0	0
H/Fe(III)-ZSM-5-MDD	18.1	0	20.5	67.2	16.4	104.0	287	3.0×10 ⁻⁶
H/Fe(II)-ZSM-5-MDD	19.1	0	19.6	73.3	9.8	102.7	190	3.2×10 ⁻⁶
Fe(III)-Si-1-MDD	0.2	0	0	0	0	0	0	0
H/Fe(II)-ZSM-5-LIE	23.5	3.0	22.7	64.9	10.6	101.2	303	3.1×10 ⁻⁶

Reaction conditions: 0.1 g catalysts; reaction temperature: 100 °C; pressure: 40 bar; gas flow: 4 ml/min N₂ and 4 ml/min CH₄; liquid flow: 1.5 ml/min of 0.12 M aqueous H₂O₂ solution.

Catalytic results related to H₂O₂ for different post-synthetically Fe-loaded MFI catalysts are shown in Table 5.5. For H-ZSM-5-C, a H₂O₂ conversion of 25.3 % with an O₂ selectivity of 15.2 % was received. The selectivity of hydrocarbon oxygenates was quite high (91.3 %) with a low selectivity of 3.1 % towards CO₂. For the self-synthesized zeolites H-ZSM-5 and Si-1, the conversions of

H_2O_2 were quite low with values of 1.7 % and 2.0 %, respectively. No hydrocarbon oxygenates and CO_2 could be detected with O_2 being the only product, indicating only H_2O_2 decomposition took place over these two zeolites. A similar catalytic performance was found also over the two catalysts based on silicalite-1, Fe(III)-Si-1-SSIE and Fe(III)-Si-1-MDD. However, it is interesting that although their Fe contents were very close (see [Table 5.1](#)), the conversions of H_2O_2 over these two catalysts differed a lot. For Fe(III)-Si-1-SSIE a rather low value of 4.3 % and for Fe(III)-Si-1-MDD a relative high value of 21.2 % was determined. This may be explained by the fact that Fe oxide species were quite different in these two samples as proved by the H_2 -TPR and UV-Vis-DR results. For H/Fe(III)-ZSM-5-SSIE, the conversion of H_2O_2 was 88.5 % and an O_2 selectivity of 37.1 % was obtained. The selectivities of hydrocarbon oxygenates and CO_2 were 53.8 % and 13.7 %, respectively. Changing the Fe-precursor in the MDD method from $\text{Fe}(\text{acac})_3$ to $\text{Fe}(\text{acac})_2$, the conversion of H_2O_2 dropped from 86.8 % for H/Fe(III)-ZSM-5-MDD to 74.3 % for H/Fe(II)-ZSM-5-MDD. It is interesting that the selectivity of hydrocarbon oxygenates significantly increased from 58.3 % to 73.0 % with the selectivity of CO_2 decreasing concomitantly from 15.8 % to 11.0 % and the selectivity of O_2 also concomitantly dropping from 31.7 % to 25.7 %, respectively. Thus, the H_2O_2 utilization over H/Fe(II)ZSM-5-MDD catalyst was much more efficient than over H/Fe(III)-ZSM-5-MDD. This observation is also consistent with the results for the methane conversion showing also less over-oxidation of formic acid (see [Table 5.4](#)). The highest H_2O_2 conversion was observed over H/Fe(II)-ZSM-5-LIE with a value of 95.2 % and the selectivities for O_2 and hydrocarbon oxygenates were 42.1 % and 53.9 %, respectively. A lowest CO_2 selectivity of 8.9 % was received over H/Fe(II)-ZSM-5-LIE, indicating a relative low level of over-oxidation, which is consistent with the low CO_2 selectivity related to methane conversion (see [Table 5.4](#)). Thus, H/Fe(II)-ZSM-5-LIE contains Fe-sites that strongly decompose H_2O_2 , but on the other hand it contains Fe-sites that more selectively oxidize methane to oxygenates.

Table 5.5. Catalytic results related to H₂O₂ for different post-synthetically Fe-loaded MFI catalysts.

Catalyst	H ₂ O ₂ conversion %	Selectivity %			
		O ₂	Hydrocarbon oxygenates	CO ₂	Sum
H-ZSM-5-C	25.3	15.2	91.3	3.1	109.6
H-ZSM-5	1.7	125.9	0	0	125.9
Si-1	2.0	112.0	0	0	112.0
H/Fe(III)-ZSM-5-SSIE	88.5	37.1	53.8	13.7	104.6
Fe(III)-Si-1-SSIE	4.3	108.8	0	0	108.8
H/Fe(III)-ZSM-5-MDD	86.8	31.7	58.3	15.8	105.8
H/Fe(II)-ZSM-5-MDD	74.3	25.7	73.0	11.0	109.7
Fe(III)-Si-1-MDD	21.2	116.6	0	0	116.6
H/Fe(II)-ZSM-5-LIE	95.2	42.1	53.9	8.9	104.7

Reaction conditions: 0.1 g catalysts; reaction temperature: 100 °C; pressure: 40 bar; gas flow: 4 ml/min N₂ and 4 ml/min CH₄; liquid flow: 1.5 ml/min of 0.12 M aqueous H₂O₂ solution.

Hutchings and co-workers [64] reported for measurements in a fixed-bed reactor that with a post-synthesized Cu/Fe-ZSM-5 catalyst based on a commercial ZSM-5 a TOF of 0.3 h⁻¹, a volumetric productivity of 9.4×10⁻⁹ mol•ml⁻¹s⁻¹ and a H₂O₂ conversion of 92.9 % were obtained, whereupon the highest methane conversion was only 0.5 %. As it can be found from Table 5.4, the selective oxidation of methane conducted in a micro fixed-bed reactor over sub-micrometer sized crystals of post-synthetically Fe-loaded H-ZSM-5 catalysts (with a similar Fe content to the reference of 0.4 %) allowed a tremendous intensification of internal and external mass transport of the overall reaction. Because the TOFs and volumetric productivities could be enhanced nearly three orders of magnitude with correspondingly much higher methane conversions. A similar enhancement of TOFs and volumetric productivities was also observed using a micro fixed-bed reactor with sub-micrometer crystals of Cu-silicalite-1/Fe-silicalite-1 as described in chapter 3. It needs to be noted, that a considerable methane conversion with a very high TOF and FA selectivity was observed over commercial H-ZSM-5-C with a Fe impurity of 175 ppm while over the self-synthesized H-ZSM-5 with Fe impurities below 10 ppm, not any activity could be observed, revealing that Brønsted acid sites can't activate methane alone. Post-synthetically Fe-loaded catalysts based on non-acidic silicalite-1 having a similar Fe content of 0.4 wt. % also showed no activity. In section 4.4 it was reported that, acidity doesn't play a significant role in the activation of methane giving

the same conversion no matter whether Brønsted acid sites are present or not. Therefore, it can be concluded that acidity plays a crucial role in obtaining a special structure of Fe species inside the micropores as the active sites using post-synthetic methods of loading Fe. This conclusion is consistent with Hellgardt and co-workers who also concluded that Brønsted acid sites are needed by providing accommodation positions for active Fe-species in ZSM-5 [126]. Different H/Fe-ZSM-5 catalysts based on the different post-synthetic methods for the loading of Fe on H-ZSM-5 showed similar methane activation activities expressed by similar methane conversions being in the range from 18.1 % to 23.5 % (see Table 5.4). However, the selectivities were different as catalysts based on Fe(II) as the precursor showed a better performance due to retarding the over-oxidation of methane, as the selectivities of CO₂ were below 11 % over H/Fe(II)-ZSM-5-MDD and H/Fe(II)-ZSM-5-LIE. Furthermore, among all post-synthetically Fe-loaded H-ZSM-5 catalysts, H/Fe(II)-ZSM-5-MDD showed the lowest H₂O₂ conversion and the highest hydrocarbon oxygenates selectivity based on H₂O₂.

5.4 Summary

Sub-micrometer sized crystals of H-ZSM-5 and silicalite-1 with Fe impurities below 10 ppm were successfully synthesized. Different post-synthetic methods and different Fe precursors were used for obtaining Fe loading of MFI zeolites of 0.40 wt. %. Compared to Hutchings and co-workers [64], the TOFs and volumetric productivities could be enhanced nearly three orders of magnitude with an around forty times higher methane conversion. Commercial H-ZSM-5-C, with trace amounts of Fe impurities of 175 ppm, already showed significant methane activation activity while on self-synthesized H-ZSM-5 with a Fe content below 10 ppm not any activity was observed, indicating that Brønsted acid sites alone can't activate methane under given conditions. Thus, it is important to have Fe-free H-ZSM-5 samples as the basis for the investigation of methane oxidation with iron-loaded H-ZSM-5 catalysts. Fe loaded on silicalite-1 having the same MFI structure as H-ZSM-5 exhibited no activity in methane conversion, even bearing the same Fe content, indicating acidity plays an important role in obtaining active Fe species when using post-synthetic methods of loading Fe. Different H/Fe-ZSM-5 catalysts based on different post-synthetic methods showed similar methane activation activities and catalysts based on Fe(II) as the precursor for loading Fe showed a better performance with regard to retarding the level of methane over-oxidation. Based on self-synthesized iron free H-ZSM-5, the liquid ion exchange with Fe(II) resulted in the only catalyst, which produced methanol in significant amounts.

6 Conclusion

Selective oxidation of methane to hydrocarbon oxygenates using aqueous H_2O_2 as an oxidant over Fe-containing MFI zeolites in a micro fixed-bed reactor was studied in the present work. Compared to literature [64], the catalytic performance could be significantly improved by intensifying mass transport, adapting reaction conditions and optimizing the preparation of Fe-containing MFI zeolites.

In the first part of this work, mass transport was intensified and reaction conditions were adapted. The catalytic results revealed that the internal and external mass transport of the overall reaction could be significantly intensified by using sub-micrometer sized Cu-silicalite-1/Fe-silicalite-1 and a micro fixed-bed reactor. Compared to results in a fixed-bed reactor reported in literature [64], the TOFs of the reaction could be enhanced nearly three orders of magnitude. The best reaction conditions comprised a relative low concentration of H_2O_2 in the aqueous solution (0.12 M), a relative high flow rate of 1.5 ml/min and a reaction temperature of 100 °C. Under the so adapted reaction conditions, a selectivity to formic acid of 96.7 % at a methane conversion of 10.3 % was obtained. The investigation of the reaction scheme revealed that the selective oxidation of methane comprises consecutive oxidation reaction steps.

Based on the obtained conclusion of the first part of this work, the preparation of Fe-MFI zeolites was optimized. The influence of different preparation conditions of Fe-silicalite-1 and different post-synthetic methods for Fe loading based on MFI zeolites were investigated.

A series of sub-micrometer and micrometer sized crystals of Fe-silicalite-1 were successfully synthesized. After calcination, migration of Fe species from framework to extra-framework positions was observed. The catalyst calcined at 550 °C showed the best catalytic performance under given conditions. Fe played an important role as nucleus of crystal growth. A relative low Fe content (around 0.5 wt. %) is preferable for the reaction. Three kinds of Fe-silicalite-1 with different crystal sizes around 140 nm, 400 nm and 5.5 μm were successfully synthesized and a sub-micrometer crystal size around 400 nm was preferable for the reaction. Four Fe-silicalite-1 catalysts with very different acidities were successfully synthesized. Brønsted acidity was found not to be a promoter for the activation of methane under given conditions, but seems to enhance over-oxidation reactions.

Sub-micrometer sized crystals of H-ZSM-5 and silicalite-1 with Fe impurities below 10 ppm were successfully synthesized. Different post-synthetic methods and different Fe precursors were used for the loading of Fe on self-synthesized zeolites. It was proven that it is important to obtain Fe free ZSM-5 samples as the basis for further investigations on the role of Fe species as active sites. Brønsted acid sites alone could not activate methane under given conditions but played a crucial role in obtaining active Fe species by post-synthetic methods of loading Fe. Different H/Fe-ZSM-5 catalysts based on different post-synthetic methods showed similar methane activation activities and catalysts based on Fe(II) as the precursor represented a better performance for retarding over-oxidation.

Based on the results and experience of current study, some prospects for future work are recommended:

1. As the role of Cu species for decreasing the level of over-oxidation was not found in this work, it could be assumed that a special structure of Cu species is needed. Thus, modifications of the preparation method for obtaining this special structure of Cu species can be considered.
2. H₂O₂ was used as oxidant in this work, which has a much higher cost compared to air or oxygen. As profitability is a requirement of every industrial process, the use or addition of air or oxygen may be tried. Another possible route is the in-situ generating of H₂O₂ during the selective oxidation reaction.
3. The calcination procedure was found to be critical for obtaining active Fe species. Thus, more systematic investigations of the calcination procedure should be carried out.
4. Advanced characterization techniques such as Mössbauer spectroscopy, EXAFS or XANES are needed to obtain more detailed information about the structure of active Fe species in the catalysts, which allows to design and tailor active catalysts more efficiently.
5. Binuclear Fe species were reported to be very active for the selective oxidation of methane. It could be an appropriate design strategy to synthesize organometallic complexes containing binuclear Fe species in the first step followed by their immobilization on solid supports as the second step. This would allow a more controlled way of preparing supported binuclear Fe species.

7 References

- [1] P. Schwach, X. Pan, X. Bao, *Chem. Rev.* 117 (2017) 8497-8520.
- [2] B.S. Liu, L. Tian, L. Li, C.T. Au, A.S.C. Cheung, *AiChE J.* 57 (2011) 1852-1859.
- [3] Annual Energy Outlook 2016-U.S. Energy Information Administration (2016).
- [4] G.A. Olah, *Angew. Chem., Int. Ed.* 44 (2005) 2636-2639.
- [5] M. Ravi, M. Ranocchiari, J.A. van Bokhoven, *Angew. Chem., Int. Ed.* 56 (2017) 16464-16483.
- [6] International Energy Outlook 2016-U.S. Energy Information Administration (2016).
- [7] C.D. Elvidge, M. Zhizhin, K. Baugh, F. Hsu, T. Ghosh, *Energies.* 9 (2016) 14-28.
- [8] A.I. Olivos-Suarez, À. Szécsényi, E.J.M. Hensen, J. Ruiz-Martinez, E.A. Pidko, J. Gascon, *ACS Catal.* 6 (2016) 2965-2981.
- [9] N. Dietl, M. Schlangen, H. Schwarz, *Angew. Chem., Int. Ed.* 51 (2012) 5544-5555.
- [10] A. Holmen, *Catal. Today.* 142 (2009) 2-8.
- [11] J.S. Woertink, P.J. Smeets, M.H. Groothaert, M.A. Vance, B.F. Sels, R.A. Schoonheydt, E.I. Solomon, *Proc. Natl. Acad. Sci. U. S. A.* 106 (2009) 18908-18913.
- [12] T.V. Choudhary, V.R. Choudhary, *Angew. Chem., Int. Ed.* 47 (2008) 1828-1847.
- [13] N.F. Goldshleger, M.B. Tyabin, A.E. Shilov, A.A. Shteinman, *Russ. J. Phys. Chem.* 43 (1969) 1222-1223.
- [14] G.B. Shul'pin, A.E. Shilov, A.N. Kitaigorodskii, J. Krevor, *J. Organomet. Chem.* 201 (1980) 319-325.
- [15] A.E. Shilov, *Pure Appl. Chem.* 50 (1978) 725-733.
- [16] A.E. Shilov, G.B. Shul'Pin, *Chem. Rev.* 97 (1997) 2879-2932.
- [17] R.A. Periana, D.J. Taube, E.R. Evitt, D.G. Loffler, P.R. Wentreck, G. Voss, T. Masuda, *Science.* 259 (1993) 340-343.
- [18] R.A. Periana, D.J. Taube, S. Gamble, H. Taube, T. Satoh, H. Fujii, *Science.* 280 (1998) 560-564.
- [19] R.A. Periana, O. Mironov, D. Taube, G. Bhalla, C.J. Jones, *Science.* 301 (2003) 814-818.
- [20] M. Ahlquist, R.J. Nielsen, R.A. Periana, W.A.I. Goddard, *J. Am. Chem. Soc.* 131 (2009) 17110-17115.

- [21] R. Palkovits, M. Antonietti, P. Kuhn, A. Thomas, F. Schueth, *Angew. Chem., Int. Ed.* 48 (2009) 6909-6912.
- [22] R. Palkovits, C. von Malotki, M. Baumgarten, K. Muellen, C. Baltes, M. Antonietti, P. Kuhn, J. Weber, A. Thomas, F. Schueth, *ChemSusChem*. 3 (2010) 277-282.
- [23] R.A. Periana, O. Mirinov, D.J. Taube, S. Gamble, *Chem. Commun.* (2002) 2376-2377.
- [24] G.E. Davico, *J. Phys. Chem. A* 109 (2005) 3433-3437.
- [25] B. Michalkiewicz, *Appl Catal A-Gen.* 394 (2011) 266-268.
- [26] Z. Guo, B. Liu, Q. Zhang, W. Deng, Y. Wang, Y. Yang, *Chem. Soc. Rev.* 43 (2014) 3480-3524.
- [27] V.N. Parmon, G.I. Panov, A. Uriarte, A.S. Noskov, *Catal. Today*. 100 (2005) 115-131.
- [28] H.F. Liu, R.S. Liu, K.Y. Liew, R.E. Johnson, J.H. Lunsford, *J. Am. Chem. Soc.* 106 (1984) 4117-4121.
- [29] K.J. Zhen, M.M. Khan, C.H. Mak, K.B. Lewis, G.A. Somorjai, *J. Catal.* 94 (1985) 501-507.
- [30] G.I. Panov, *CATTECH* 4 (2000) 18-31.
- [31] G.I. Panov, G.A. Sheveleva, A.S. Kharitonov, V.N. Romannikov, L.A. Vostrikova, *Appl Catal A-Gen.* 82 (1992) 31-36.
- [32] L.V. Pirutko, V.S. Chernyavsky, A.K. Uriarte, G.I. Panov, *Appl Catal A-Gen.* 227 (2002) 143-157.
- [33] G. Panov, K. Dubkov, E. Starokon, *Catal. Today*. 117 (2006) 148-155.
- [34] M.V. Parfenov, E.V. Starokon, L.V. Pirutko, G.I. Panov, *J. Catal.* 318 (2014) 14-21.
- [35] E.V. Starokon, K.A. Dubkov, L.V. Pirutko, G.I. Panov, *Top. Catal.* 23 (2003) 137-143.
- [36] Y. Wang, K. Otsuka, *J. Chem. Soc., Faraday Trans.* 91 (1995) 3953-3961.
- [37] X. Wang, Y. Wang, Q. Tang, Q. Guo, Q. Zhang, H. Wan, *J. Catal.* 217 (2003) 457-467.
- [38] Y. Wang, W. Yang, L. Yang, X. Wang, Q. Zhang, *Catal. Today*. 117 (2006) 156-162.
- [39] N.D. Spencer, *J. Catal.* 109 (1988) 187-197.
- [40] N.D. Spencer, C.J. Pereira, *J. Catal.* 116 (1989) 399-406.
- [41] Y. Wang, D. An, Q. Zhang, *Sci. China: Chem.* 53 (2010) 337-350.
- [42] K. Tabata, Y. Teng, T. Takemoto, E. Suzuki, M.A. Banares, M.A. Pena, J. Fierro, *Catal. Rev.* 44 (2002) 1-58.
- [43] A. Holmen, *Catal. Today*. 142 (2009) 2-8.

- [44] A. Parmaliana, F. Arena, V. Sokolovskii, F. Frusteri, N. Giordano, *Catal. Today*. 28 (1996) 363-371.
- [45] S. Irusta, L.M. Cornaglia, E.E. Miro, E.A. Lombardo, *J. Catal.* 156 (1995) 167-170.
- [46] P. Mars, D.W. van Krevelen, *Chem. Eng. Sci.* 3 (1954) 41-59.
- [47] R.K. Grasselli, *Top. Catal.* 21 (2002) 79-88.
- [48] R. Schlögl, A. Knop-Gericke, M. Hävecker, U. Wild, D. Frickel, T. Ressler, R.E. Jentoft, J. Wienold, G. Mestl, A. Blume, O. Timpe, Y. Uchida, *Top. Catal.* 15 (2001) 219-228.
- [49] N. Ohler, A.T. Bell, *J. Phys. Chem. B* 110 (2006) 2700-2709.
- [50] S. Chempath, A.T. Bell, *J. Catal.* 247 (2007) 119-126.
- [51] N.V. Beznis, B.M. Weckhuysen, J.H. Bitter, *Catal. Lett.* 136 (2010) 52-56.
- [52] N.V. Beznis, A.N.C. van Laak, B.M. Weckhuysen, J.H. Bitter, *Microporous Mesoporous Mater.* 138 (2011) 176-183.
- [53] J. Piera, J. Bäckvall, *Angew. Chem., Int. Ed.* 47 (2008) 3506-3523.
- [54] D. Lance, E.G. Elworthy, French Patent 352687 (1905).
- [55] H.J.H. Fenton, *J. Chem. Soc., Trans.* 65 (1894) 899-911.
- [56] F. Harber, J. Weiss, *Proc. R. Soc. London, Ser. A* 147 (1934) 332-351.
- [57] S. Navalon, M. Alvaro, H. Garcia, *Appl. Catal., B* 99 (2010) 1-26.
- [58] L.C. Kao, A.C. Hutson, A. Sen, *J. Am. Chem. Soc.* 113 (1991) 700-701.
- [59] G.V. Nizova, G. Süß-Fink, G.B. Shul Pin, *Chem. Commun.* (1997) 397-398.
- [60] Q. Yuan, W. Deng, Q. Zhang, Y. Wang, *Adv. Synth. Catal.* 349 (2007) 1199-1209.
- [61] M.H. Ab Rahim, M.M. Forde, R.L. Jenkins, C. Hammond, Q. He, N. Dimitratos, J.A. Lopez-Sanchez, A.F. Carley, S.H. Taylor, D.J. Willock, D.M. Murphy, C.J. Kiely, G.J. Hutchings, *Angew. Chem., Int. Ed.* 52 (2013) 1280-1284.
- [62] G.B. Shul'Pin, G.V. Nizova, Y.N. Kozlov, L. Gonzalez Cuervo, G. Süß-Fink, *Adv. Synth. Catal.* 346 (2004) 317-332.
- [63] C. Hammond, M.M. Forde, M.H. Ab Rahim, A. Thetford, Q. He, R.L. Jenkins, N. Dimitratos, J.A. Lopez-Sanchez, N.F. Dummer, D.M. Murphy, A.F. Carley, S.H. Taylor, D.J. Willock, E.E. Stangland, J. Kang, H. Hagen, C.J. Kiely, G.J. Hutchings, *Angew. Chem., Int. Ed.* 51 (2012) 5129-5133.
- [64] J. Xu, R.D. Armstrong, G. Shaw, N.F. Dummer, S.J. Freakley, S.H. Taylor, G.J. Hutchings, *Catal. Today* 270 (2016) 93-100.

- [65] M.H. Ab Rahim, R.D. Armstrong, C. Hammond, N. Dimitratos, S.J. Freakley, M.M. Forde, D.J. Morgan, G. Lalev, R.L. Jenkins, J.A. Lopez-Sanchez, S.H. Taylor, G.J. Hutchings, *Catal. Sci. Technol.* 6 (2016) 3410-3418.
- [66] J.K. Edwards, B. Solsona, E.N. N, A.F. Carley, A.A. Herzing, C.J. Kiely, G.J. Hutchings, *Science*. 323 (2009) 1037-1041.
- [67] R.S. Hanson, T.E. Hanson, *Microbiol. Rev.* 60 (1996) 439-471.
- [68] H. Dalton, *Philos. Trans. R. Soc., B* 360 (2005) 1207-1222.
- [69] R. Balasubramanian, S.M. Smith, S. Rawat, L.A. Yatsunyk, T.L. Stemmler, A.C. Rosenzweig, *Nature* 465 (2010) 115-119.
- [70] V.C.C. Wang, S. Maji, P.P.Y. Chen, H.K. Lee, S.S.F. Yu, S.I. Chan, *Chem. Rev.* 117 (2017) 8574-8621.
- [71] J.D. Semrau, A.A. DiSpirito, S. Yoon, *FEMS Microbiol. Rev.* 34 (2010) 496-531.
- [72] C.E. Tinberg, S.J. Lippard, *Acc. Chem. Res.* 44 (2011) 280-288.
- [73] R. Banerjee, Y. Proshlyakov, J.D. Lipscomb, D.A. Proshlyakov, *Nature* 518 (2015) 431-434.
- [74] A.S. Hakemian, A.C. Rosenzweig, *Annu. Rev. Biochem.* 76 (2007) 223-241.
- [75] R.L. Lieberman, A.C. Rosenzweig, *Nature* 434 (2005) 177-182.
- [76] S.I. Chan, K. Chen, S. Yu, C.L. Chen, S. Kuo, *Biochemistry* 43 (2004) 4421-4430.
- [77] S.I. Chan, V.C. Wang, J.C.H. Lai, S.S.F. Yu, P.P.Y. Chen, K.H.C. Chen, C. Chen, M.K. Chan, *Angew. Chem., Int. Ed.* 46 (2007) 1992-1994.
- [78] S.I. Chan, S.S.F. Yu, *Acc. Chem. Res.* 41 (2008) 969-979.
- [79] B.E.R. Snyder, M.L. Bols, R.A. Schoonheydt, B.F. Sels, E.I. Solomon, *Chem. Rev.* (2017).
- [80] Y. Shiota, K. Yoshizawa, *J. Am. Chem. Soc.* 122 (2000) 12317-12326.
- [81] A.R. Kulkarni, Z. Zhao, S. Siahrostami, J.K. Norskov, F. Studt, *ACS Catal.* 6 (2016) 6531-6536.
- [82] E. Rezabal, F. Ruiperez, J.M. Ugalde, *Phys. Chem. Chem. Phys.* 15 (2013) 1148-1153.
- [83] N. Dietl, C. van der Linde, M. Schlangen, M.K. Beyer, H. Schwarz, *Angew. Chem., Int. Ed.* 50 (2011) 4966-4969.
- [84] M.H. Groothaert, P.J. Smeets, B.F. Sels, P.A. Jacobs, R.A. Schoonheydt, *J. Am. Chem. Soc.* 127 (2005) 1394-1395.

- [85] J.S. Woertink, P.J. Smeets, M.H. Groothaert, M.A. Vance, B.F. Sels, R.A. Schoonheydt, E.I. Solomon, *Proc. Natl. Acad. Sci. U.S.A.* 106 (2009) 18908-18913.
- [86] P.J. Smeets, R.G. Hadt, J.S. Woertink, P. Vanelderen, R.A. Schoonheydt, B.F. Sels, E.I. Solomon, *J. Am. Chem. Soc.* 132 (2010) 14736-14738.
- [87] S.I. Chan, Y. Lu, P. Nagababu, S. Maji, M. Hung, M.M. Lee, I. Hsu, D.M. Pham, J.C.H. Lai, K.Y. Ng, S. Ramalingam, S.S.F. Yu, M.K. Chan, *Angew. Chem., Int. Ed.* 52 (2013) 3731-3735.
- [88] C. Liu, C. Mou, S.S.F. Yu, S.I. Chan, *Energy Environ. Sci.* 9 (2016) 1361-1374.
- [89] S. Grundner, M.A.C. Markovits, G. Li, M. Tromp, E.A. Pidko, E.J.M. Hensen, A. Jentys, M. Sanchez-Sanchez, J.A. Lercher, *Nat. Commun.* 6 (2015) 7546-7554.
- [90] E.M. Alayon, M. Nachtegaal, M. Ranocchiari, J.A. van Bokhoven, *Chem. Commun.* 48 (2012) 404-406.
- [91] P. Tomkins, A. Mansouri, S.E. Bozbag, F. Krumeich, M.B. Park, E.M.C. Alayon, M. Ranocchiari, J.A. van Bokhoven, *Angew. Chem., Int. Ed.* 55 (2016) 5467-5471.
- [92] K. Narsimhan, K. Iyoki, K. Dinh, Y. Román-Leshkov, *ACS Cent. Sci.* 2 (2016) 424-429.
- [93] B.R. Wood, J.A. Reimer, A.T. Bell, M.T. Janicke, K.C. Ott, *J. Catal.* 225 (2004) 300-306.
- [94] E.V. Starokon, M.V. Parfenov, S.S. Arzumanov, L.V. Pirutko, A.G. Stepanov, G.I. Panov, *J. Catal.* 300 (2013) 47-54.
- [95] B.E.R. Snyder, P. Vanelderen, M.L. Bols, S.D. Hallaert, L.H. Bottger, L. Ungur, K. Pierloot, R.A. Schoonheydt, B.F. Sels, E.I. Solomon, *Nature* 536 (2016) 317.
- [96] R.L. Garten, W.N. Delgass, M. Boudart, *J. Catal.* 18 (1970) 90-107.
- [97] P. Marturano, L. Drozdová, A. Kogelbauer, R. Prins, *J. Catal.* 192 (2000) 236-247.
- [98] X.B. Feng, W.K. Hall, *Catal. Lett.* 46 (1997) 11-16.
- [99] H. Chen, W.M.H. Sachtler, *Catal. Today.* 42 (1998) 73-83.
- [100] F. Heinrich, C. Schmidt, E. Löffler, M. Menzel, W. Grünert, *J. Catal.* 212 (2002) 157-172.
- [101] E.J.M. Hensen, Q. Zhu, M.M.R.M. Hendrix, A.R. Overweg, P.J. Kooyman, M.V. Sychev, R.A. van Santen, *J. Catal.* 221 (2004) 560-574.
- [102] A.A. Battiston, J.H. Bitter, D.C. Koningsberger, *Catal. Lett.* 66 (2000) 75-79.

- [103] L.J. Shu, Y. Liu, J.D. Lipscomb, L. Que, *JBIC, J. Biol. Inorg. Chem.* 1 (1996) 297-304.
- [104] J.A. Ryder, A.K. Chakraborty, A.T. Bell, *J. Phys. Chem. B.* 106 (2002) 7059-7064.
- [105] M.J. Rice, A.K. Chakraborty, A.T. Bell, *J. Catal.* 186 (1999) 222-227.
- [106] C. Nozaki, C.G. Lugmair, A.T. Bell, T.D. Tilley, *J. Am. Chem. Soc.* 124 (2002) 13194-13203.
- [107] C. Hammond, R.L. Jenkins, N. Dimitratos, J.A. Lopez-Sanchez, M.H. Ab Rahim, M.M. Forde, A. Thetford, D.M. Murphy, H. Hagen, E.E. Stangland, J.M. Moulijn, S.H. Taylor, D.J. Willock, G.J. Hutchings, *Chem. - Eur. J.* 18 (2012) 15735-15745.
- [108] C. Hammond, N. Dimitratos, R.L. Jenkins, J.A. Lopez-Sanchez, S.A. Kondrat, M. Hasbi Ab Rahim, M.M. Forde, A. Thetford, S.H. Taylor, H. Hagen, E.E. Stangland, J.H. Kang, J.M. Moulijn, D.J. Willock, G.J. Hutchings, *ACS Catal.* 3 (2013) 689-699.
- [109] J.F. Jia, K.S. Pillai, W. Sachtler, *J. Catal.* 221 (2004) 119-126.
- [110] I. Yuranov, D.A. Bulushev, A. Renken, L. Kiwi-Minsker, *J. Catal.* 227 (2004) 138-147.
- [111] Q. Zhu, R.M. van Teeffelen, R.A. van Santen, E.J.M. Hensen, *J. Catal.* 221 (2004) 575-583.
- [112] M. Schwidder, S. Heikens, A. Detoni, S. Geisler, M. Berndt, A. Brückner, W. Grünert, *J. Catal.* 259 (2008) 96-103.
- [113] A. Shishkin, P. Carlsson, H. Härelind, M. Skoglundh, *Top. Catal.* 56 (2013) 567-575.
- [114] M. Schwidder, M.S. Kumar, K. Klementiev, M.M. Pohl, A. Bruckner, W. Grunert, *J. Catal.* 231 (2005) 314-330.
- [115] J.A. Ryder, A.K. Chakraborty, A.T. Bell, *J. Phys. Chem. B.* 106 (2002) 7059-7064.
- [116] J. Park, J. Choung, I. Nam, S. Ham, *Appl. Catal., B* 78 (2008) 342-354.
- [117] K. Sun, H. Xia, Z. Feng, R. van Santen, E. Hensen, C. Li, *J. Catal.* 254 (2008) 383-396.
- [118] G. Berlier, G. Spoto, S. Bordiga, G. Ricchiardi, P. Fisticaro, A. Zecchina, I. Rossetti, E. Selli, L. Forni, E. Giamello, C. Lamberti, *J. Catal.* 208 (2002) 64-82.
- [119] S. Bordiga, R. Buzzoni, F. Geobaldo, C. Lamberti, E. Giamello, A. Zecchina, G. Leofanti, G. Petrini, G. Tozzola, G. Vlaic, *J. Catal.* 158 (1996) 486-501.
- [120] R.B. Borade, *Zeolites* 7 (1987) 398-403.
- [121] R. Szostak, V. Nair, T.L. Thomas, *J. Chem. Soc., Faraday Trans. 1.* 83 (1987) 487-494.
- [122] G. Vorbeck, M. Richter, R. Fricke, B. Parlitz, E. Schreier, K. Szulzewsky, B. Zibrowius, *Stud. Surf. Sci. Catal.* 65 (1991) 631-644.

- [123] Q. Kan, Z. Wu, R. Xu, Q. Wei, S. Peng, G. Xiong, S. Sheng, J. Huang, *Stud. Surf. Sci. Catal.* 69 (1991) 241-249.
- [124] B.M. Abu-Zied, W. Schwieger, A. Unger, *Appl. Catal., B* 84 (2008) 277-288.
- [125] Y. Li, J.N. Armor, *Appl Catal A-Gen.* 188 (1999) 211-217.
- [126] C. Kalamaras, D. Palomas, R. Bos, A. Horton, M. Crimmin, K. Hellgardt, *Catal. Lett.* 146 (2016) 483-492.
- [127] A.J. Vanhengstum, J.G. Vanommen, H. Bosch, P.J. Gellings, *Appl. Catal.* 5 (1983) 207-217.
- [128] M.G. White, *Catal. Today.* 18 (1993) 73-109.
- [129] A. Hanu, S. Liu, V. Meynen, P. Cool, E. Popovici, E.F. Vansant, *Microporous Mesoporous Mater.* 95 (2006) 31-38.
- [130] J. Sonntag, PhD thesis, University of Stuttgart, 2016.
- [131] A.E. Persson, B.J. Schoeman, J. Sterte, J.E. Otterstedt, *Zeolites* 14 (1994) 557-567.
- [132] R. Van Grieken, J.L. Sotelo, J.M. Menéndez, J.A. Melero. *Microporous Mesoporous Mater.* 39 (2000) 135-147.
- [133] S. Brunauer, P.H. Emmett, E. Teller, *J. Am. Chem. Soc.* 60 (1938) 309-319.
- [134] D. Fodor, A.B. Redondo, F. Krumeich, J.A. van Bokhoven, *J. Phys. Chem. C* 119 (2015) 5447-5453.
- [135] A.K.M.L. Rahman, M. Kumashiro, T. Ishihara, *Catal. Commun.* 12 (2011) 1198-1200.
- [136] D. Scarano, A. Zecchina, S. Bordiga, F. Geobaldo, G. Spoto, G. Petrini, G. Leofanti, M. Padovan, G. Tozzola, *J. Chem. Soc., Faraday Trans.* 89 (1993) 4123-4130.
- [137] M.M. Mohamed, N.A. Eissa, *Mater. Res. Bull.* 38 (2003) 1993-2007.
- [138] E. Rafiee, S. Eavani, *Green Chem.* 13 (2011) 2116.
- [139] D. Meloni, R. Monaci, V. Solinas, G. Berlier, S. Bordiga, I. Rossetti, C. Oliva, L. Forni, *J. Catal.* 214 (2003) 169-178.
- [140] J. Pérez-Ramírez, G. Mul, F. Kapteijn, J.A. Moulijn, A.R. Overweg, A. Doménech, A. Ribera, I.W.C.E. Arends, *J. Catal.* 207 (2002) 113-126.
- [141] S. Brandenberger, O. Kroecker, A. Wokaun, A. Tissler, R. Althoff, *J. Catal.* 268 (2009) 297-306.
- [142] B. Hunger, J. Hoffmann, O. Heitzsch, M. Hunger, *J. Therm. Anal.* 36 (1990) 1379-1391.
- [143] L.J. Lobree, I. Hwang, J.A. Reimer, A.T. Bell, *J. Catal.* 186 (1999) 242-253.

- [144] P. Ratnasamy, R. Kumar, *Catal. Today*. 9 (1991) 329-416.
- [145] T. Inui, H. Matsuda, O. Yamase, H. Nagata, K. Fukuda, T. Ukawa, A. Miyamoto, J. *Catal.* 98 (1986) 491-501.
- [146] S. Yuen, Y. Chen, J.E. Kubsh, J.A. Dumesic, N. Topsoe, H. Topsoe, *J. Phys. Chem. C* 86 (1982) 3022-3032.
- [147] O.J. Wimmers, P. Arnoldy, J.A. Moulijn, *J. Phys. Chem.* 90 (1986) 1331-1337.
- [148] M.S. Kumar, M. Schwidder, W. Grünert, A. Brückner, *J. Catal.* 227 (2004) 384-397.
- [149] G.D. Pirngruber, P.K. Roy, R. Prins, *Phys. Chem. Chem. Phys.* 8 (2006) 3939-3950.
- [150] M. Santhoshkumar, M. Schwidder, W. Grünert, U. Bentrup, A. Brückner, *J. Catal.* 239 (2006) 173-186.

List of figures

Figure 1.1.	U.S. dry natural gas production by source for 1990-2040 (trillion cubic feet) [3].	1
Figure 1.2.	World natural gas consumption for 2012-2040. Data from Ref. [6].	2
Figure 1.3.	Overview of the different routes for the valorization of methane [8].	3
Figure 1.4.	Proposed catalytic cycle for the Hg (II) catalyzed methane oxidation reaction [17].	5
Figure 1.5.	Proposed reaction mechanism for the oxidation of methane by (bpym)PtCl ₂ [18].	6
Figure 1.6.	Mechanism of the α -sites' formation [35].	8
Figure 1.7.	Proposed mechanism the selective oxidation of CH ₄ at isolated, SiO ₂ -supported MoO _x sites [49].	10
Figure 1.8.	The catalytic cycle includes stable MMOH ^{ox} and MMOH ^{red} (diferrous sMMO hydroxylase) and detectable transient species O, P*, P, Q and T; transient states QS and R were predicted from kinetic, spectroscopic, and chemical studies [73].	16
Figure 1.9.	Proposed diamond-core structure of compound Q proposed in sMMO, having two irons (Fe ^{IV}) bridged by oxygen atoms. The numbered groups in black surrounding the diamond core are the side chains of amino-acid residues. H, histidine residues; E, glutamate residues [73].	16
Figure 1.10.	Proposed structure of pMMO subunits [75].	18
Figure 1.11.	Proposed structure of the dicopper center as active sites in pMMO. From Ref. [5].	18
Figure 1.12.	Activation of dioxygen by two Cu(I) centers [70].	19
Figure 1.13.	Structural models of ZSM-5 and the Cu ₂ O intermediate used for DFT calculations: Large model constructed from part of a 10-membered ring [85].	20
Figure 1.14.	Proposed reaction pathway for Cu species [86].	20
Figure 1.15.	A) Productive cycling and B) abortive cycling in the oxidation of methane by O ₂ , mediated by the [Cu ^I Cu ^I Cu ^I (7-N-Etppz)] ¹⁺ complex in the presence of H ₂ O ₂ as the sacrificial reductant [87].	21

Figure 1.16.	Structure and location of $[\text{Cu}_3(\mu\text{-O})_3]^{2+}$ cluster in mordenite predicted by DFT [89]. a), the main channel of MOR; b), the MOR side pocket.....	22
Figure 1.17.	DFT-predicted structure of $\alpha\text{-O}$ in Fe-BEA [95].	24
Figure 1.18.	(a) Structure of active center in MMOH as reported in [103] and proposed Fe_2O_2 -type clusters in Fe-ZSM-5 compensating (b) one or (c) two lattice charges [97].	25
Figure 1.19.	Proposed reaction sequence for the formation of methoxy species on Fe and Si sites [93].	26
Figure 1.20.	Proposed reaction mechanism for selective oxidation of CH_4 over Fe-ZSM-5 or Fe-silicalite-1 using H_2O_2 [63].	27
Figure 1.21.	A proposed reaction scheme for the oxidation of methane and the function of Cu component [63].	28
Figure 1.22.	Proposed potential reactions of extra-framework Fe species with the host matrix (residual Brønsted sites and/or zeolite walls) [118].	30
Figure 1.23.	The potential mechanism of the MDD method by using $\text{Fe}(\text{acac})_3$ as the precursor of Fe.	33
Figure 2.1.	Flow sheet of the experimental setup in this work.	37
Figure 2.2.	The micro reactor used in this work.	37
Figure 2.3.	The slug flow observed from the transparent tube in front of the reactor.	37
Figure 3.1.	XRD patterns of the catalysts.	51
Figure 3.2.	SEM images of the catalysts. a) silicalite-1, b) Cu-silicalite-1/Fe-silicalite-1...51	51
Figure 3.3.	Selectivity of hydrocarbon oxygenates as a function of the methane conversion for the present work and from literature (Ref. 1: [63], Ref. 2: [64] and Ref. 3: [135]).	58
Figure 3.4.	Proposed reaction scheme for the selective oxidation of methane under given conditions.	59
Figure 4.1.	TGA profile of template containing Fe-silicalite-1 sample.	62
Figure 4.2.	XRD patterns of Fe-silicalite-1 catalysts calcined at different temperatures.	64
Figure 4.3.	TEM image of 0.5Fe-Si-1-syn	64
Figure 4.4.	Transmission FT-IR spectra of Fe-silicalite-1 catalysts calcined at different temperatures in the OH stretching region. (a) 0.5Fe-Si-1-syn, (b) 0.5Fe-Si-1-370,	

	(c) 0.5Fe-Si-1-450, (d) 0.5Fe-Si-1-550, (e) 0.5Fe-Si-1-650, (f) 0.5Fe-Si-1-750.....	65
Figure 4.5.	Transmission FT-IR spectra of Fe-silicalite-1 catalysts calcined at different temperatures in the framework stretching region. (a) 0.5Fe-Si-1-syn, (b) 0.5Fe-Si-1-370, (c) 0.5Fe-Si-1-450, (d) 0.5Fe-Si-1-550, (e) 0.5Fe-Si-1-650, (f) 0.5Fe-Si-1-750.....	66
Figure 4.6.	H ₂ -TPR profiles of Fe-silicalite-1 catalysts calcined at different temperatures. (a) 0.5Fe-Si-1-370, (b) 0.5Fe-Si-1-450, (c) 0.5Fe-Si-1-550, (d) 0.5Fe-Si-1-650, (e) 0.5Fe-Si-1-750.	68
Figure 4.7.	NH ₃ -TPD profiles of Fe-silicalite-1 catalysts calcined at different temperatures. (a) 0.5Fe-Si-1-370, (b) 0.5Fe-Si-1-450, (c) 0.5Fe-Si-1-550, (d) 0.5Fe-Si-1-650, (e) 0.5Fe-Si-1-750.	70
Figure 4.8.	UV-Vis-DR spectra of Fe-silicalite-1 catalysts calcined at different temperatures. (a) 0.5Fe-Si-1-syn, (b) 0.5Fe-Si-1-450, (c) 0.5Fe-Si-1-550, (d) 0.5Fe-Si-1-650, (e) 0.5Fe-Si-1-750.	71
Figure 4.9.	XRD patterns of Fe-silicalite-1 catalysts with different Fe contents.	77
Figure 4.10.	TEM images of Fe-silicalite-1 catalysts with different Fe contents. (a) H-0.5Fe-Si-1, (b) H-1.2Fe-Si-1, (c) H-2.0Fe-Si-1, (d) H-2.6Fe-Si-1, (e) H-3.7Fe-Si-1.	78
Figure 4.11.	NH ₃ -TPD profiles of Fe-silicalite-1 catalysts with different Fe contents. (a) Fe-Si-1-WI, (b) H-0.5Fe-Si-1, (c) H-1.2Fe-Si-1, (d) H-2.0Fe-Si-1, (e) H-2.6Fe-Si-1, (f) H-3.7Fe-Si-1.....	79
Figure 4.12.	H ₂ -TPR profiles of Fe-silicalite-1 catalysts with different Fe contents. (a) H-0.5Fe-Si-1, (b) H-1.2Fe-Si-1, (c) H-2.0Fe-Si-1, (d) H-2.6Fe-Si-1, (e) H-3.7Fe-Si-1.	81
Figure 4.13.	H ₂ -TPR profile of Fe-Si-1-WI.	81
Figure 4.14.	UV-Vis-DR spectra of Fe-silicalite-1 catalysts with different Fe contents. (a) H-0.5Fe-Si-1, (b) H-1.2Fe-Si-1, (c) H-2.0Fe-Si-1, (d) H-2.6Fe-Si-1, (e) H-3.7Fe-Si-1.	83
Figure 4.15.	FT-IR spectra of Fe-silicalite-1 catalysts with different Fe contents. (a) H-0.5Fe-Si-1, (b) H-1.2Fe-Si-1, (c) H-2.0Fe-Si-1, (d) H-2.6Fe-Si-1, (e) H-3.7Fe-Si-1.	84

Figure 4.16.	Simplified schematic for the mass transport from the gas over the liquid phase to the solid phase in the three-phase system.	87
Figure 4.17.	XRD patterns of Fe-silicalite-1 catalysts with different crystal sizes.	89
Figure 4.18.	TEM images and SEM image of Fe-silicalite-1 catalysts with different crystal sizes. TEM images for (a) H-0.5Fe-Si-1-SC, (b) H-0.5Fe-Si-1, (c) H-0.5Fe-Si-1-LC and SEM image of (d) H-0.5Fe-Si-1-LC.	90
Figure 4.19.	NH ₃ -TPD profiles of Fe-silicalite-1 catalysts with different crystal sizes.	91
Figure 4.20.	H ₂ -TPR profiles of Fe-silicalite-1 catalysts with different crystal sizes.	92
Figure 4.21.	XRD patterns of different Fe-silicalite-1 catalysts with different acidities.	97
Figure 4.22.	TEM images of Fe-silicalite-1 catalysts with different acidities. (a) 0.5Fe-Si-1-550, (b) H-0.5Fe-Si-1, (c) Na-0.5Fe-Si-1-LIE, (d) Na-0.5Fe-Si-1-S.	98
Figure 4.23.	NH ₃ -TPD profiles of Fe-silicalite-1 catalysts with different acidities.	99
Figure 5.1.	XRD patterns of the post-synthetically Fe-loaded MFI catalysts.	106
Figure 5.2.	TEM images of H-ZSM-5 (a) and Si-1 (b)	106
Figure 5.3.	NH ₃ -TPD profiles of the post-synthetically Fe-loaded MFI catalysts.	107
Figure 5.4.	H ₂ -TPR profiles of the post-synthetically Fe-loaded MFI catalysts.	109
Figure 5.5.	UV-Vis-DR spectra of the post-synthetically Fe-loaded MFI catalysts..	112

List of tables

Table 2.1.	Chemicals used in this work.....	35
Table 2.2.	Overview of the prepared samples in this work.	42
Table 3.1.	The chemical compositions and textural properties of different catalysts	50
Table 3.2.	Catalytic results related to CH ₄ under different reaction temperatures.	53
Table 3.3.	Catalytic results related to H ₂ O ₂ under different reaction temperatures.....	53
Table 3.4.	Catalytic results related to CH ₄ for different reaction conditions under 100 °C. 56	
Table 3.5.	Catalytic results related to H ₂ O ₂ for different reaction conditions under 100 °C.	56
Table 3.6.	Catalytic results of using different hydrocarbon oxygenates as reactants.	59
Table 4.1.	Chemical compositions and textural properties of Fe-silicalite-1 catalysts calcined at different temperatures.	63
Table 4.2.	Hydrogen consumption during the H ₂ -TPR experiments for Fe-silicalite-1 catalysts calcined at different temperatures.	69
Table 4.3.	Catalytic results related to CH ₄ for Fe-silicalite-1 catalysts calcined at different temperatures.....	72
Table 4.4.	Catalytic results related to H ₂ O ₂ for Fe-silicalite-1 catalysts calcined at different temperatures.....	72
Table 4.5.	Chemical compositions and textural properties of Fe-silicalite-1 catalysts with different Fe contents.	76
Table 4.6.	Hydrogen consumption in the H ₂ -TPR experiments and the ratio of different reduction peaks for Fe-silicalite-1 catalysts with different Fe contents. Area I: low temperature reduction peak area; area II: high temperature reduction peak area.	82
Table 4.7.	Catalytic results related to CH ₄ for Fe-silicalite-1 catalysts with different Fe contents.	85
Table 4.8.	Catalytic results related to H ₂ O ₂ for Fe-silicalite-1 catalysts with different Fe contents.	85
Table 4.9.	Chemical compositions and textural properties of Fe-silicalite-1 catalysts with different crystal sizes.	88

Table 4.10.	Hydrogen consumption during the H ₂ -TPR experiments and the ratio of different reduction peaks for Fe-silicalite-1 catalysts with different crystal sizes. Area I: low temperature reduction peak area; area II: high temperature reduction peak area.....	92
Table 4.11.	Catalytic results related to CH ₄ for Fe-silicalite-1 catalysts with different crystal sizes.....	93
Table 4.12.	Catalytic results related to H ₂ O ₂ for Fe-silicalite-1 catalysts with different crystal sizes.....	94
Table 4.13.	Chemical compositions and textural properties of Fe-silicalite-1 catalysts with different acidities.	96
Table 4.14.	Catalytic results related to CH ₄ for Fe-silicalite-1 catalysts with different acidities.	100
Table 4.15.	Catalytic results related to H ₂ O ₂ for Fe-silicalite-1 catalysts with different acidities.....	101
Table 5.1.	Chemical compositions and textural properties of the post-synthetically Fe-loaded MFI catalysts.	105
Table 5.2.	Hydrogen consumption during the H ₂ -TPR experiments of the temperature range of 200-800°C for the post-synthetically Fe-loaded MFI catalysts.....	109
Table 5.3.	Relative numerical analysis of UV-Vis-DR spectra of post-synthetically Fe-loaded MFI catalysts in Figure 5.5. Percentage of the sub-bands due to the relative contribution of different range of wavelength.	113
Table 5.4.	Catalytic results related to CH ₄ for different post-synthetically Fe-loaded MFI catalysts.....	114
Table 5.5.	Catalytic results related to H ₂ O ₂ for different post-synthetically Fe-loaded MFI catalysts.....	116